博士学位论文
DOCTORAL DISSERTATION

博 士 学 位 论 文

# RHIC能区金金碰撞中$\pi$介子各向异性流对碰撞能量, 中心度及电荷不对称性依赖的研究

**论文作者:** 柯宏伟
**指导教师:** 刘峰，唐爱红，许怒
**申请学位:** 理学博士
**专业名称:** 粒子物理与原子核物理
**研究方向:** 相对论重离子碰撞

华中师范大学物理科学与技术学院

二零一叁年五月

博士学位论文

DOCTORAL DISSERTATION

A Dissertation for Doctor of Philosophy in Physics

# Beam Energy, Collision Centrality and Charge Asymmetry Dependence of the Pion Event Anisotropy in Au+Au Collisions at RHIC

by Hongwei Ke

Co-supervisor: Feng Liu, Aihong Tang, Nu Xu

Central China Normal University

May 2013

# 摘　要

实验证据显示, 在高能重离子碰撞中产生的热密的新物质形态是一种强相互作用的夸克胶子等离子体. 建造于美国布鲁克海汶国家实验室的相对论重离子对撞机是专门用来研究夸克胶子等离子体的性质以及量子色动力学相图的实验装置. 理论研究指出, 在相对论重离子碰撞的早期, 手征对称性可能恢复. 同时由于在半中心的金金碰撞中产生了极强的磁场, 手征磁效应和手征分离效应相耦合可以诱导产生一种电荷和手征荷的密度波, 被称为手征磁波. 在相对论重离子碰撞中, 手征磁波会产生一个电四极矩. 该电四极矩会导致带电粒子的方位角分布各向异性$v_2$有电荷不对性的依赖. 理论研究认为, 这种效应可以通过带电的$\pi$介子观测到.

本文将报告在质心系能量为$\sqrt{s_{NN}}$ = 200, 62.4, 39, 27 和19.6 GeV的金金碰撞中, $\pi$介子在$0.15 < p_T < 0.5$ GeV/c, $|\eta| < 1$范围内的积分$v_2$. 本文分别研究了$\pi^+$介子和$\pi^-$介子的积分$v_2$对电荷不对性的依赖. 我们观察到, 随着电荷不对性的增加, $\pi^+$介子的$v_2$线性减小, 而$\pi^-$介子的$v_2$线性增加. $\pi^+$和$\pi^-$的$v_2$差别$\Delta v_2 = v_2^{\pi^-} - v_2^{\pi^+}$与电荷不对性$A_{ch}$成正比. 理论认为, $\Delta v_2(A_{ch})$的斜率能反映由手征磁效应引起的电四极矩的强度. 本文测量了在所研究的质心能量和中心度下的该斜率. 我们发现, 从中心碰撞到边缘碰撞, $\Delta v_2(A_{ch})$的斜率先增加后减小. 上述观测均与基于手性磁波的理论计算定性地一致. 我们还注意到, $\Delta v_2(A_{ch})$的斜率从质心能量200 GeV到27 GeV仅显示出很弱的能量依赖性, 其原因尚不完全清楚.

在实验研究方面, 本文也讨论了STAR高阶触发器的开发和升级工作. 随着RHIC的亮度和STAR的数据采集能力的不断提高, 实验数据的生产和存储面临很大挑战. 为了保证稀有事例物理分析的速度以及在RHIC低能实验时实时监测RHIC和STAR的运行状态, 我们开发了STAR的高阶触发器. 高阶触发器是基于高性能计算机集群的软件系统, 被用于实时径迹重建和事件整合. 在之前的实验中, 高阶触发器已经被用于在线挑选包含有高横动量, 双电子以及轻核信号的事件. 正是基于高阶触发器在2010年挑选的事例样本, STAR首次发现了反氦-4原子核并测量了$J/\psi$介子的椭圆流.

作者自2010年起参与STAR高阶触发器的开发工作, 特别是面向高性能计算的升级工作. 作者对STAR高阶触发器的贡献包括如下几个方面的工作. 首先, 作者测量了高阶触发器的径迹重建效率. 径迹重建效率是理解整个高阶触发器性能的基础. 其次, 为

了应对在线次级顶点重建带来的高强度的计算需求, 作者研究学习了如何使用通用图形处理器(GPGPU)来加速高阶触发器的应用, 并开发实现了一个基于通用图形处理器的次级顶点重建器原型. 与传统的基于拓扑结构计算的次级顶点重建器相比, 这一原型的运算速度加快了约60倍. 在最近一年, 作者还研究了如何把基于元胞自动机的径迹重建器应用于STAR高阶触发器. 我们已经用元胞自动机径迹重建器替换了之前使用的基于保角映射的径迹重建器, 并将在今年的实验中进行测试.

# Abstract

In high energy heavy ion collisions, a new state of hot and dense matter has been created. A series of evidences indicate that such a new state of matter is a strongly coupled Quark-Gluon Plasma (QGP). The Relativistic Heavy Ion Collider (RHIC), built at Brookhaven National Laboratory, is a dedicated machine to study properties of QGP as well as the QCD phase diagram. Theoretical studies suggest that the chiral symmetry is restored at the early stage of heavy ion collisions, and with an extremely strong magnetic field generated in middle central Au + Au collisions, the chiral magnetic effect and chiral separation effect can couple with each other and create density waves of electric and chiral charge, namely, the chiral magnetic wave. The chiral magnetic wave in heavy ion collisions induces an electric quadrupole momentum and leads to a charge asymmetry dependence of azimuthal anisotropy $v_2$ of charged particles. It is argued that such effect can be observed via charged pions.

In this thesis, the integrated $v_2$ of $\pi^+$ and $\pi^-$ with $0.15 < p_T < 0.5\,\mathrm{GeV//c}$ and $|\eta| < 1$ in all centralities of Au + Au collisions at $\sqrt{s_{NN}} = 200, 62.4, 39, 27$ and 19.6 GeV are presented. The measured $v_2$ is studied as a function of charge asymmetry $A_{ch}$. It is observed that $v_2$ of $\pi^+(\pi^-)$ linearly decrease (increase) with the increase of charge asymmetry. The $v_2$ difference between $\pi^+$ and $\pi^-$, $\Delta v_2 = v_2^{\pi^-} - v_2^{\pi^+}$, is proportional to the charge asymmetry $A_{ch}$. The slope parameter of $\Delta v_2(A_{ch})$, which is believed to be related to the electric quadrupole momentum induced by the chiral magnetic wave, is extracted for all the centralities and all energies under study. The slope parameter is shown to have a rise and fall feature from central to peripheral collisions, with a weak energy dependence from $\sqrt{s_{NN}} = 200\,\mathrm{GeV}$ to $27\,\mathrm{GeV}$. These observations are qualitatively consistent with theoretical calculations based on chiral magnetic wave.

On the experiment-development side, the implementation and upgrade of the STAR High-Level Trigger (HLT) is discussed. The increasing RHIC luminosity and STAR data-taking capability pose a great challenge to data production and storage. To assure the fast physics output for a selective physics topics based on rare events, as well as to

monitor RHIC/STAR real-time performing during RHIC low energy runs, a High Level Trigger (HLT) is implemented for STAR. The HLT is a software system built on high performance PC cluster to performer real time tracking and event assembling. It has been used to select events containing high $p_T$ , di-electron, light nuclei signals. Based on the HLT selected data sample in year 2010, STAR has observed the anti-helium-4 nuclei, and studied the elliptic flow of $J/\psi$.

Since 2010, the author has participated in the development of the STAR HLT, especially the upgrade towards high performance parallel computing. The author's contributions to HLT include, first, the estimation of HLT tracking efficiency, which sets a baseline for the understanding the HLT trigger performance. Secondly, to cope with the intensive computing requirement of online secondary vertex reconstruction, the author has studied the application of general purpose GPU acceleration and obtained a prototype of GPU based secondary vertex finder which runs 60 times faster than the conventional implementation. In the recent year, the author studied the cellular automaton (CA) based tracker and is adopting it to the STAR HLT.

# Table of Contents

# List of Figures

# List of Tables

# CHAPTER 1

# Introduction

Over the last century our understanding of the fundamental building blocks of the matter has become more complete. According to the standard model, the matter constituents include six quarks and six leptons. Different quarks distinguish from each other by their flavors, which are, $u$ (up), $d$ (down), $c$ (charm), $s$ (strange), $t$ (top) and $b$ (bottom). The lepton family consists of $e$ (electron), $\mu$ (muon), $\tau$ (tauon) and three neutrinos corresponding to each of them. All of those twelve particles are fermions and have spin $= 1/2$. There are four fundamental forces or interactions : strong, weak, electromagnetic and gravitational. Interactions between different particles are mediated by vector bosons. Electromagnetic interaction happens via interchanging photons between charged particles. Weak interaction is mediated by $W^{\pm}$ and $Z$ bosons between all fermions. Strong interaction is carried by eight different gluons between objects with color charge. Comparing to the other three interactions, gravitation is quite different from others and will not be discussed in this dissertation. The electromagnetic force is described by the quantum electrodynamics (QED) and in 1970s, electrodynamics and weak interactions were unified. The strong interaction is described by the quantum chromodynamics (QCD).

## 1.1 Quantum Chromodynamics

Introduced by Gell-Mann and Fritzsch in 1972 [FG72], QCD is a nonabelian gauge theory based on the gauge group $SU(3)_C$, and has been widely accepted as the theory to describe the interaction between colored objects, including quarks and gluons. The

QCD Lagrangian can be written as

$$\mathcal{L}_{QCD} = i\sum_q \bar{\psi}_q^i \gamma^\mu (D_\mu)_{ij} \psi_q^i - \sum_q m_q \bar{\psi}_q^i \psi_q^i - \frac{1}{4} F_{\mu\nu}^{(a)} F^{\mu\nu}, \tag{1.1}$$

$$F_{\mu\nu}^{(a)} = \partial_\mu A_\nu^a - \partial_\nu A_\mu^a - g_s f_{abc} A_\mu^b A_\nu^c, \tag{1.2}$$

$$(D_\mu)_{ij} = \delta_{ij}\partial_\mu + i g_s \sum_a \frac{\lambda_{i,j}^a}{2} A_\mu^a, \tag{1.3}$$

where $F_{\mu\nu}^{(a)}$ is the gluonic field strength tensor, $g_s$ is the QCD coupling constant and $f_{abc}$ is the structure constant of the $SU(3)_C$ algebra. What makes the QCD different from the QED is the third term of Eq. 1.2, which is, the interaction between gluons. In QED, the interaction carrier are photons, which do not have electric charge thus do not interact among themselves. However, for the case of QCD, the self coupling of gluons makes it far more complex than QED.

### 1.1.1 Asymptotic Freedom and Confinement

QCD has two unique properties, namely the asymptotic freedom [Pol73, GW73] and the confinement, both of which come from the running coupling constant. The effect coupling constant as a function of energy scale $\mu$,

$$\alpha_s(\mu) = \frac{g_s^2(\mu)}{4\pi} \approx \frac{4\pi}{\beta_0 \ln(\mu^2/\Lambda_{\mathrm{QCD}}^2)}. \tag{1.4}$$

The asymptotic freedom means that the interaction between quarks is stronger at larger distance, and weaker at shorter distance. The experimental measurements of $\alpha_s$ at different respective energy scale, shown in Fig. 1.1, confirmed this argument. With larger $Q$, quarks can move closer to each other where $\alpha_s$ becomes smaller. The small $\alpha_s$ suggests that at high energy quarks and gluons move freely.

On the contrary, if a pair of quarks are separated away from each other the interaction will become stronger with increasing distance. Potential energy between the quark pair will also increase, and at some point, the potential energy is large enough to create a new pair of quarks. Since quark pairs are colorless and quarks have color charge, this feature suggests that color charge is confined in colorless objects, like hadrons. The color confinement means that color charge cannot be isolated and seen directly in physics

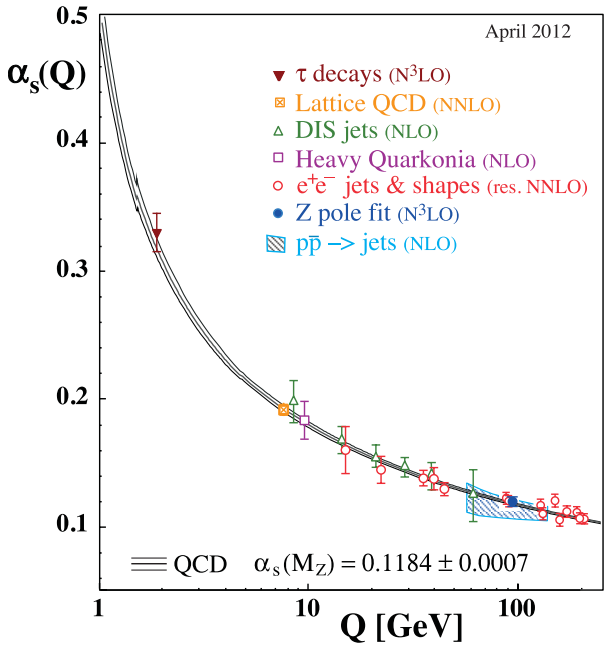


**Figure 1.1**: Measured strong coupling constant $\alpha_s$ as a function of the respective energy scale $Q$. Figure taken from [BAB12].

vacuum.

### 1.1.2 Quark-gluon Plasma

Shortly after the idea of asymptotic freedom was proposed, people realized that it can lead to important consequences [CP75a, CP75b]. When the temperature or density is high enough and the strong interaction becomes very weak, quarks and gluons can move freely in a range much larger than the size of a hadron. In this case, a new state of deconfined matter, the *quark-gluon plasma* (QGP), is created. QGP is believed to had existed at the very beginning of our universe. In laboratory, heavy ion collisions are the best place to create such hot and dense matter. The search for QGP started decades ago and recently it is widely believed that it has been created in relativistic heavy ion collisions [BS07].

Lattice QCD calculations show that at temperature of about $T$ = 170 eV, significant change of degree of freedom occurs, indicating a phase transition[KLP00, Kar02]. The saturation value in Fig. 1.2 is far from the StefanBoltzmann limits for the ideal gas, and

it suggests that the new state of matter is not free of interactions but strongly coupled.

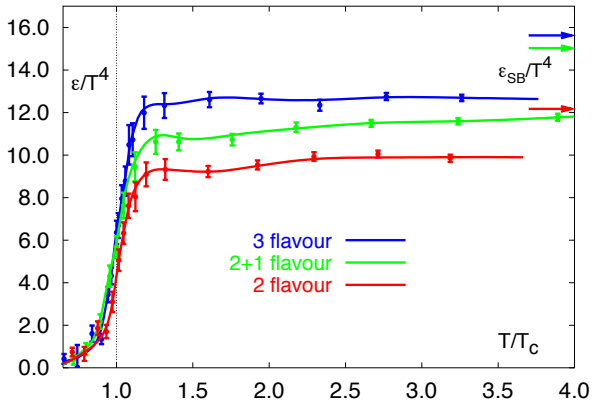


**Figure 1.2**: Energy density in lattice QCD as a function of temperature reduced by the critical temperature $T_c$.

In heavy ion experiments at RHIC, there are mounting evidences for the existence of a new state of matter. Fig. 1.3 shows the number-of-constituent-quark (NCQ) scaling observed at STAR. The universal scaling of $v_2/n_q$, $n_q$ = 2(3) for mesons (hadrons), indicates that partonic, not hadronic, degree of freedom is relevant. Fig. 1.4 shows that the high $p_T$ di-hadron back-to-back correlation disappears in Au + Au collisions. It supports that high $p_T$ jets lose considerable amount of energy due to the dense matter created in heavy ion collisions. Relativistic hydrodynamic study of elliptic flow suggests that the new state of matter created at RHIC is a strongly coupled fluid with very small bulk viscosity, and thus is called 'the perfect liquid' [HKH01, AAA05b].

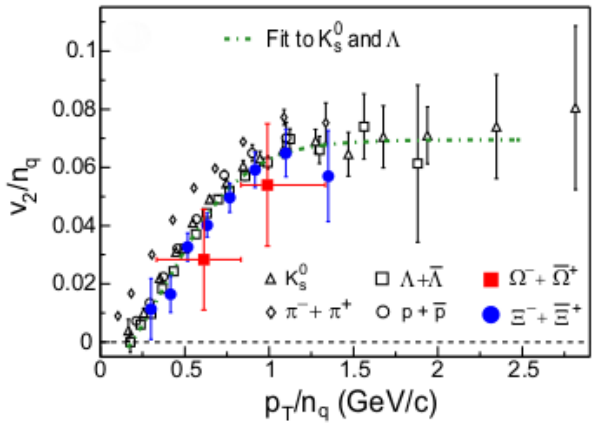


**Figure 1.3**: Number-Of-Constituent-Quark scaling observed at STAR [AAA05b].

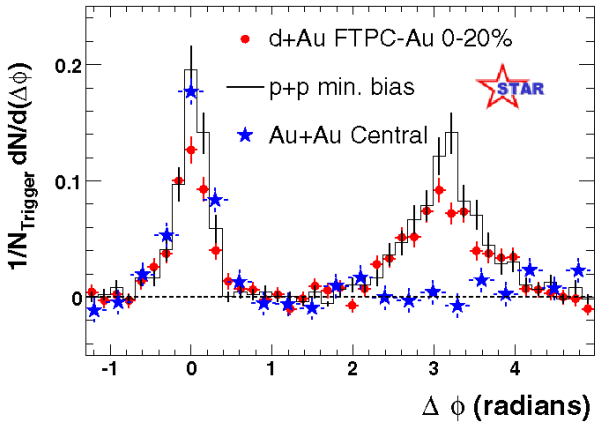


**Figure 1.4**: High $p_T$ di-hadron azimuthal correlation measured at STAR. The back-to-back correlation disappears in Au + Au collisions [AAA05b].

### 1.1.3 QCD Phase Diagram

With the existence of QGP confirmed, the next important task is to determine at what temperature and baryon chemical potential the normal nuclear matter transits to QGP, i.e. to determine the QCD phase diagram. The lattice QCD calculation, shown in Fig. 1.2, shows that at zero baryon chemical potential there is no sudden change of energy density, instead, it is a smooth crossover transition. On the other hand, at low temperature and large baryon chemical potential, this transition should be of the first order. Naturally, one expects that the first order phase transition line should reach its end (the QGP *critical point*) at somewhere as the chemical potential decreases. Searching for the phase boundary and the critical point is one of the most important goals of the current heavy ion experiments.

At RHIC, a beam energy scan (BES) program has been launched to explore the QCD phase diagram[AAA10c]. During the BES phase I in year 2010 and 2011, the STAR experiment has recorded data of Au + Au collisions at $\sqrt{s_{NN}}$ = 39, 27, 19.6, 11.5 and 7.7 GeV. Hints for new features occurring around 19.6 GeV [AAA10b, ] have been seen. A comparison between experimental data and lattice calculations suggests that the critical temperature is about $T_c$ = 175 MeV [GLM11].

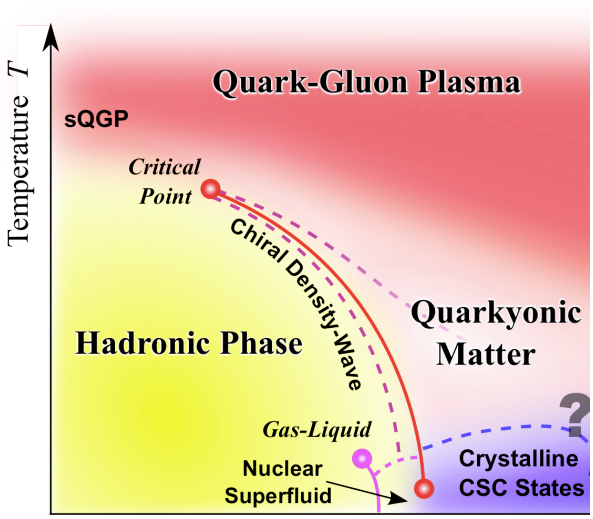


**Figure 1.5**: Conjectured QCD phase diagram. The $x$ axis is baryon chemical potential or baryon number density. The $y$ axis is temperature. Figure taken from [FH11].

## 1.2 Heavy Ion Collisions

Because increasing the mass number of the incident particles is more efficient than increasing beam energy, heavy ion collision is believed to be the best way to search for and study the properties of QCD matter in laboratory. Since 1970's, heavy ion experiments have been performed world wide. Relativistic heavy ion collider (RHIC) built in Brookhaven National Laboratory is the first accelerator-collider dedicated to heavy ion collisions. Just after the first a few years of operation, a strongly coupled QGP has been found in high energy Au + Au collisions [AAA05c, ABB05, BBB05, AAA05b]. The current task of RHIC is to study the properties of QGP and explore the QCD phase diagram. The Large Hadron Collider (LHC) in CERN is pushing the colliding energy to 5.5 TeV, where the energy density and temperature is way more higher than the requirement of QGP formation. Therefore, it is also a very useful facility to study the properties of QGP.

### 1.2.1 Time Evolution

In high energy heavy ion collisions, incident nuclei are accelerated to a speed comparable to the speed of light. At RHIC's top energy, gold nuclei travel at 99.995% of the speed of light, where the relativistic Lorentz factor reaches about 100. In this case, the size of incident nuclei in the moving direction is contracted by a factor of about 1/100. In the laboratory reference frame, one observes two disks colliding with each other.

At the beginning of the collision, the system stays in the the initial pre-equilibrium state in which partons from the incident nucleons scatter with each other. Hard scattering process with large momentum transfer generate jets and heavy flavor quarks. A few models have been proposed to describe the dynamics at the parton scattering stage, including the color-string model [Mat87], color glass condensate [McL10] and perturbative QCD model [Wan97]. However, it is still much of unknown about the parton scattering stage and the discussion of the dynamics happened in that stage is ongoing.

After a short time $\tau_0$ of frequent scatterings, quarks and gluons reach a local, thermal equilibrium. It is believed that QGP is formed in this stage. As the collision system expands, it also cools down. When the the temperature cools down to the phase transition temperature, hadronization process starts and quarks bind in hadrons again. The newly generated hadrons also go through a scattering stage, in which new hadrons may generated via inelastic collisions as well as decay. When the temperature cools down to the chemical freeze-out temperature $T_{ch}$, inelastic collisions stop and hadron components are fixed. Hadrons continue to fly out of the collision area and still experience elastic collisions. Finally when the temperature reaches the kinematic freeze-out temperature $T_{fo}$, no more collisions between hadrons can happen. At this time the momentum spectrum is fixed. What the heavy ion experiments measured are hadrons after the kinematic freeze-out.

Even hadrons went through so many stages before reaching the detector, the information from the parton phase is not completely washed out. By measuring the final state hadrons, the properties of QGP can be learned.

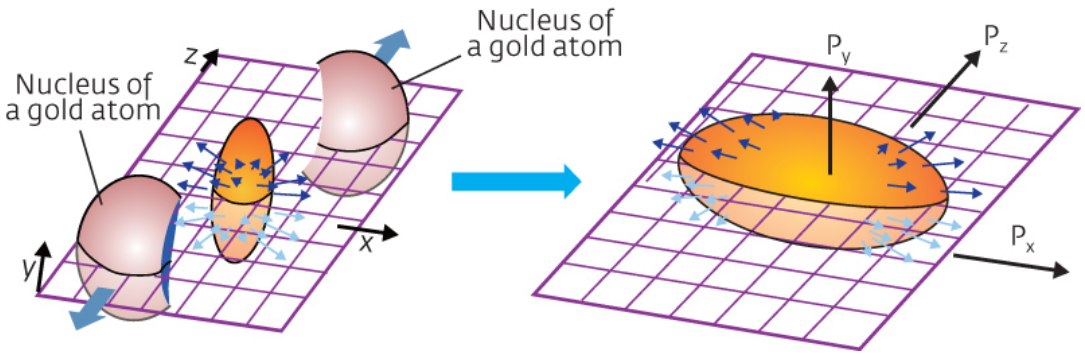


**Figure 1.6**: Initial coordinate space anisotropy converts to momentum space anisotropy.

### 1.2.2 Transverse Azimuthal Anisotropy

One of the most important observables to reveal the parton stage properties is the transverse azimuthal anisotropy of final state hadrons, which is largely determined by processes at the parton stage.

Fig. 1.6 illustrates a major source of azimuthal anisotropy in non-central Au + Au collisions, in which spectators keep moving in their incident directions and a significant fraction of energy is deposited in the collision region that has an 'almond' shape. The pressure difference from the center to the surface is the same for all directions, and it pushes matter in the fireball out in a collective motion, regardless of particles' species and locations. However, in short axis, because that the distance between the center and the surface is shorter than that along the long axis, the pressure gradient is larger. Therefore the matter along the short axis will be pushed out harder than that along the long axis. By that, the initial coordinate space anisotropy is converted to the momentum space anisotropy.

Although the initial anisotropy in coordinate space contributes mostly the azimuthal anisotropy in momentum space at the final stage, it is not the only source. Other effects, like decay, jets, ridge and HBT etc., can create different azimuthal correlations at various levels. The chiral magnetic wave, which will be discussed in detail in Chapter 4, can induce an electric quadruple momentum leading to different azimuthal anisotropy of positive and negative charged particles. This effect, if exists, can be observed via charged pions.

## 1.3 QCD Vacuum Transition and Local Parity Violation

Partiy violation in weak interactions was been proposed and observed in 1950's [LY56, WAH57]. It is believed that parity is conserved in strong interactions. However, more recent studis suggested that, in hot and dense matter created in high energy heavy ion collisions, metastable domains may be created, in which parity time-reversal symmetries are locally violated [KPT98]. This can happen because of the QCD vacuum transition. QCD vacua corresponds to local and global potential energy minimum of the gauge field configuration. Different QCD vacua can transit between each other via instantons and sphalerons. At low energy, QCD vacuum transition can only happen via instantons, which refers to the quantum tunneling effect between states and is exponentially suppressed. However, it is suggested that at high energy, there is sufficient energy to climb over the potential barrier to another states and the exponential suppress factor may disappear, which is the sphalerons solution [Man83, KM84, KMW08]. QCD vacuum transition has a profound understanding – it creates different number of the left-handed and right-handed quarks. This is parity violation in strong interactions. However, this can happen only in metastable domains, which are localized in space and time. Therefore, it is called Local Parity Violation (LPV).

If a metastable domain with LPV exist, with the help of a strong external magnetic field it can manifest itself via the chiral magnetic effect. Meanwhile, a chiral magnetic wave, which is the coupling of chiral magnetic effect and chiral separation effect, may also exist in heavy ion collisions. These phenomena will be discussed in details in Chapter. 4. In this dissertation, the difference of the azimuthal anisotropy of $\pi^+$ and $\pi^-$ in different centralities and energies will be presented as a function of event-by-event charge asymmetry. A linear relation between the two is argued to be the consequence of the chiral magnetic wave.

## 1.4 Online Event Selection with High Performance Computing

The other part of the dissertation is the development of the STAR High-Level Trigger (HLT). The idea of a HLT is putting a high performance PC cluster at the end of the trigger pipeline, to collect information from all detectors and perform a full event reconstruction. The advantage of doing so is that based on the fully reconstructed events, complex event selection criteria can be implemented for special physics interests, especially for rare processes. A fast online event reconstruction can also be used to monitor data quality in real time. In the high luminosity era, a high-level trigger can effectively reduce the recording rate, while still fully utilizes the fully luminosity.

In the STAR experiment, the data acquisition system operates at a speed that is two orders of magnitude faster than that in the initial design, together with the continuously increasing RHIC luminosity, they pose quite a challenge for data processing and storage. For instance, STAR took more than 800 million of Au + Au 200 GeV in 2010 and more than billion events in 2011. For each year, more than 500 TB of disk space is needed to store a single copy of these data. What makes things more challenging is that, it usually takes several months of work of a few thousands of CPUs to produce these data sample for data taken in a single year. With the continuously increasing RHIC luminosity and STAR data taking capability, the pressure on the computing and storage will only increase.

Out of the large data volume, a small fraction of events are rare and are of special interest, examples include but not limited to events containing high $p_T$ , di-electron, heavy flavor and light nuclei. A high-level trigger can reconstruct tracks and identify particle species in real time, based on which rare events can be selected. This approach can significantly enrich the rare events sample and help to relief the pressure on computing. In addition, because of the ability of real time event reconstruction, HLT can also be used to monitor the real time performance of the accelerator and detectors.

In Chapter 3, we will discussed the performance, application and physics output

of the current STAR high-level trigger. Its new development and upgrade will also be discussed.

# CHAPTER 2

# The STAR Experiment

## 2.1 The Relativistic Heavy Ion Collider

The Relativistic Heavy Ion Collider (RHIC) built in Brookhaven National Laboratory is the first dedicated accelerator-collider facility for heavy ion physics, and it is also the only polarized proton accelerator in the world. Because of its unique design, RHIC is very flexible and can accelerate particles within a large mass range and a wide energy range. Since its first operation in 2000, RHIC has successfully accelerated proton ($p$), deuteron ($d$), copper (Cu), gold (Au) and Uranium (U) beams. Proton beams usually operates at 100 GeV and 250 GeV. Heavy ion beams, especially the Au beams, can operate from 200 GeV/nucleon down to 7.7 GeV/nucleon, the latter is even lower than the injection energy. RHIC has two separated storage rings and can accelerate different particle species simultaneously. This feature makes RHIC capable of providing not only symmetric collisions, like $p+p$, Cu + Cu, Au + Au and U + U, but also asymmetric collisions, like $d$ + Au and Cu + Au.

Fig. 2.1 shows the scenario of accelerating gold ions in the RHIC accelerator complex. The Au ions are produced by a pulsed sputter ion source with charge $Q = -1$ and are sent to the first accelerator in the injector chain the Tandem Van de Graaff accelerator [Thi84]. The Van de Graaff is a linear elector-static accelerator with stripping foil inside. When leaving the Van de Graaff, Au ions obtain the kinetic energy of ~ 1 MeV/nucleon and charge $Q = +12$. There are two Van de Graaff operates in parallel, therefore, different ions can be provided for asymmetric collisions. After Van de Graaff, Au ions are further stripped to charge $Q = +32$ and transferred through a transfer line to

the Booster synchrotron. Booster synchrotron will strip most of the electrons and finally has Au ions to be accelerated to 95 MeV/nucleon. The outgoing Au ions from Booster are in the state of charge $Q = +77$ and are sent to the next accelerator, the Alternating-Gradient Synchrotron (AGS). The ion bunches from Booster are debunched and then rebunched to larger bunches in AGS, and accelerated to 8.86 GeV/nucleon. The last two electrons of Au atom are striped when exiting AGS resulting the state of $Q = +79$. Au ion bunches are injected in the two RHIC rings in which they are accelerated to the top energy 100 GeV/nucleon.

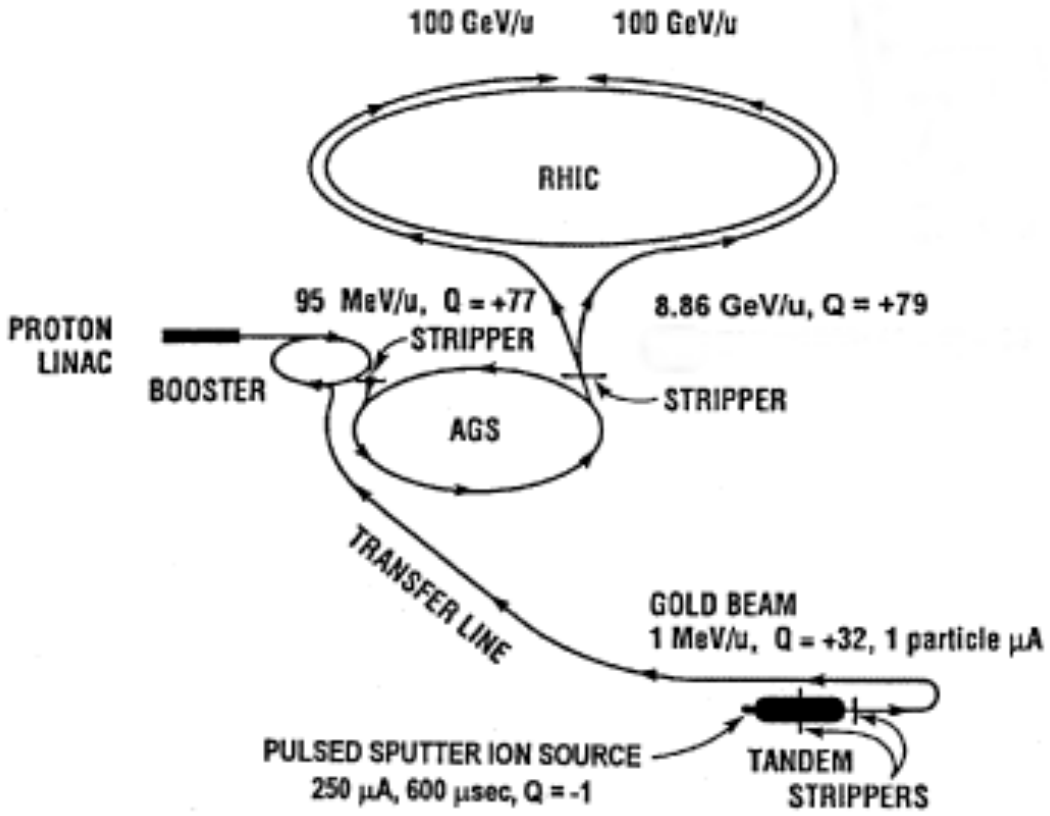


**Figure 2.1**: The Relativistic Heavy Ion Collider acceleration scenario for gold ions. Figure token from [HFF03].

RHIC is the last part in the accelerator chain. It consists of two separated 3.8 km long beam pipes equipped with superconducting magnets for beam focusing and bending. The top energy in RHIC is 100 GeV/nucleon for Au ions and this number increases with increasing charge-to-mass ratio, i.e. 125 GeV/nucleon for lighter nuclei and 250 GeV for

protons.

There are six interaction points on the RHIC circle where detectors for physics experiments can be placed. Particle collisions can happen at all of the interaction points at the same time, allowing different experiments to take data simultaneously. For now STAR and PHENIX experiment take the interaction point sites at 6 o'clock and 8 o'clock respectively and the 4 o'clock interaction point is used by the radio-frequency (RF) equipment of the accelerator.

## 2.2 The STAR Detectors

The Solenoidal Tracker at RHIC (STAR) is one of the two large experiments operating at RHIC. The most prominent feature of the STAR detector complex is its large, uniform acceptance. The collision area at STAR is covered by concentric cylindrical detectors, including a Time Projection Chamber (TPC), a Time of Flight (TOF) detector and a Barrel Electromagnetic Calorimeter (BEMC). This year, two new detectors, a Heavy Flavor Tracker (HFT) and a Muon Telescope Detector (MTD), are partly installed for testing. All detectors, except MTD, sit in in a homogeneous magnetic field along the beam line direction generated by the STAR magnets. The maximum magnetic field strength is $B_Z$ = 0.5 T and it can also run with a half field configuration with $B_Z$ = 0.25 T. Fig. 2.2 illustrates the barrel part of the up to date STAR detector complex.

The Time Projection Chamber is the main detector of STAR, and it covers the full azimuthal angle and pseudo-rapidity $|\eta| < 1.8$. TPC records the trajectories of particles traveling through its gas volume. Because of the magnetic field, charged particles move along helices, and the geometry of which carries the kinematic information. TPC also records the ionization energy loss of charged particles, by which, together the momentum information derived from tracking, particles can be identified. TPC will be discussed in detail in next section. The TPC is surrounded by the Time of Flight (TOF) detector. The TOF measures the time of flight between the moment of collision and the moment

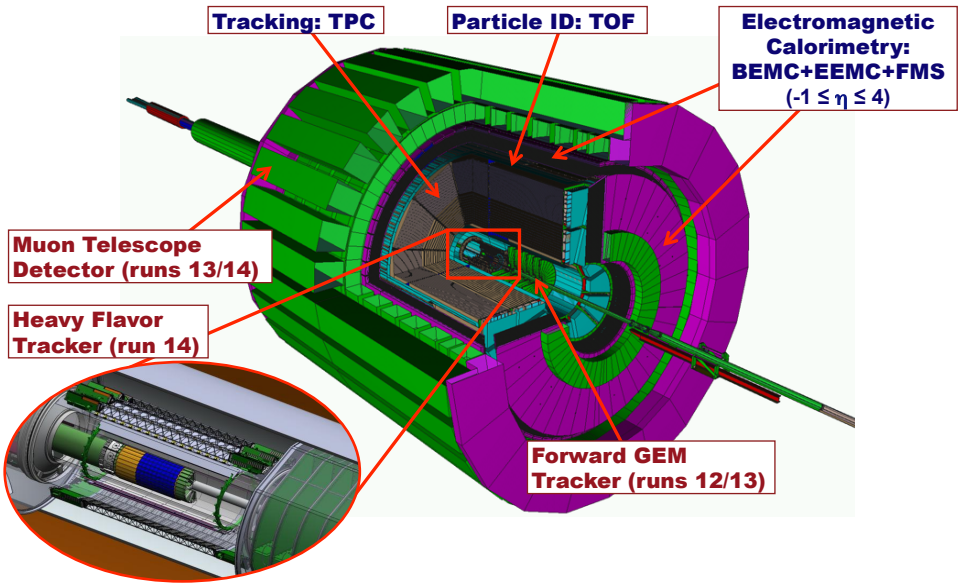


**Figure 2.2**: STAR detector complex.

of particles reaching the TOF. This measurement can be translated into the velocity of particles. Because particles with different mass and the same momentum have difference velocity, they can be separated from each other. Outside of the TOF is the Barrel Electric Magnetic Calorimeter (BEMC), which measures the energy deposition of particles. The energy deposition can be used to distinguish high momentum photons and electrons from hadrons. The next layer in the detector complex is the STAR magnet. Most of hadrons cannot survive the bulky material of STAR magnet, but muons, with small cross sections, can penetrate the magnet and reach the the outmost detector, the Muon Telescope Detector (MTD).

In the forward direction, there is a Forward GEM Tracker (FGT), an End-cap Electromagnetic Calorimeter (EEMC), a Beam Beam Counter (BBC), two upgraded pseudo Vertex Position Detectors (upVPD) and two Zero-Degree Calorimeters (ZDC). The FGT takes the place of the Forward TPC (FTPC) with a pseudo-rapidity coverage of $1 < |\eta| < 2$, and it focuses on the tracking of forward leptons. The BBC consists of two scintillator annuli mounted on the east and west side out of the STAR magnets, with a pseudo-rapidity coverage of $3.3 < |\eta| < 5.0$. The two upVPDs are installed 5.4 m away from the TPC center on both sides. It provides the start time to TOF for trigger purposes. ZDC is the farthest detector from the collision center. The two ZCDs are

located at 18 m from the TPC center, from east and west. They measure the shower energy deposited in scintillators by neutrons and serve as a trigger detector as well as a monitor of the RHIC luminosity.

Out these subsystems, TOF, EMC, upVPD, BBC and ZDC are fast detectors. They can be used as trigger detectors to reject background events. More discussion on trigger detectors can be found in Sec. 2.2.2.

An overview of STAR detector complex can be found in Ref. [AAA03], along with details of its subsystems.

### 2.2.1 Time Projection Chamber

The Time Projection Chamber [ABB03a, ABB03b] is the main tracker of STAR. As shown in Fig. 2.3, STAR TPC is a cylindrical detector with a length of 420 cm, and inner and outer radii of 50 cm and 200 cm, respectively. The whole inner volume of the TPC is filled with P10 gas (10% methane, 90% argon) with a pressure of 2 mbar above the atmospheric pressure. In the center of TPC, there is a central membrane which divides the gas volume into east and west halves. The TPC has a uniform electric field inside, which is defined by the central membrane, the inner and outer field cage, and the end caps. The central membrane is operated at 28 kV and the end caps are at ground. The inner and the outer field cages provide a series of equal-potential rings that divide the each half of the TPC into 182 equally spaced parts. This configuration makes the electric field in the TPC pointing from the central membrane to the end caps with uniform gradient.

When a charged particle passes through the TPC gas volume, its trajectory is a helix because of the magnetic field $B_z$. The projection of the helix in $x-y$ plane is a circle, whose curvature is determined by particle's transverse momentum. Gas atoms near a particle trajectory can be ionized by the high energy particle passing by. The electrons from the ionization process will drift to the two ends the TPC driven by the electric field. The typical drift velocity is 5.45 cm/μs at 130 Vcm drift field. At the two ends of TPC, drifting electrons are be collected by the TPC read out system to generate

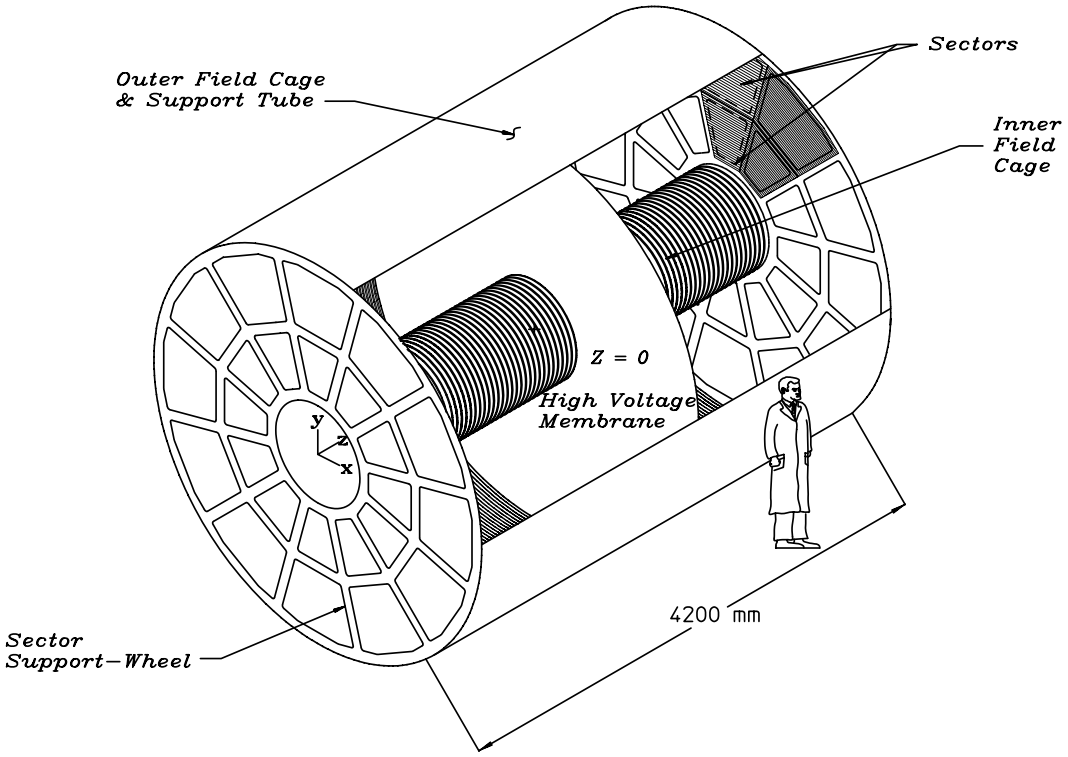


**Figure 2.3**: STAR Time Projection Chamber

signals.

The TPC read out system is based on the Multi-Wire Proportional Chambers (MWPC) with readout pads. In total, there are 24 sectors with 12 at each end. Fig. 2.4 shows one TPC sector as an example. The position of fired pads by drifting electrons indicates the $x-y$ position of a TPC hit and the time when it is fired gives the $z$ position. This is where the name Time Projection Chamber comes from.

Because that the ionization energy loss $\mathrm{d}E/\mathrm{d}x$ is different for different particles with the same momenta, it can be used to identify different particle species. The mean rate of $\mathrm{d}E/\mathrm{d}x$ is given by the Bethe-Bloch formula[BAB12]. Fig. 2.5 shows the ionization energy loss $\mathrm{d}E/\mathrm{d}x$ of different particle species as a function of momentum. With $\mathrm{d}E/\mathrm{d}x$, $\pi$, $K$ and $p$ can be separated up to 0.6 GeV/c, $\pi$ and $K$ can be separated from $p$ up to 1 GeV/c. Muon and electron yields are usually much lower than hadrons. In SATR, a normalized deviation of ionization energy loss from its expected value is defined as

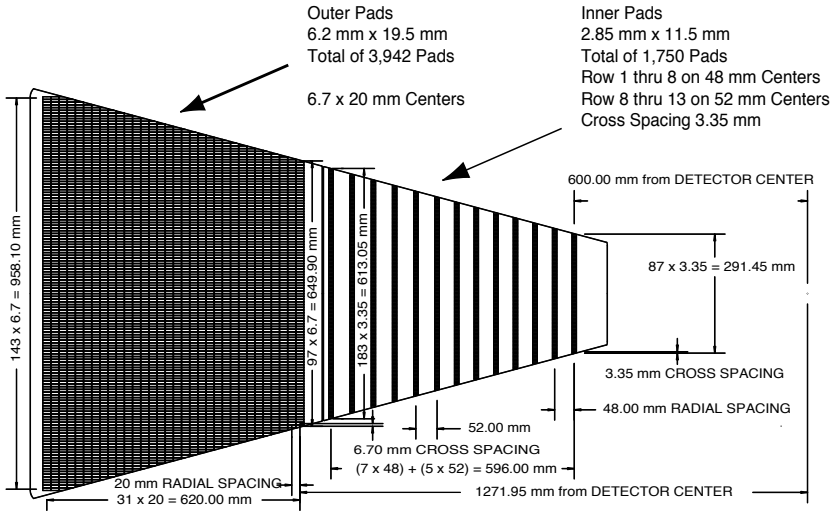


**Figure 2.4**: A TPC readout sector.

$$n\sigma_i = \frac{1}{R}\log\frac{\mathrm{d}E/\mathrm{d}x_{\mathrm{measured}}}{\langle \mathrm{d}E/\mathrm{d}x\rangle_i}, \tag{2.1}$$

where $i = \pi, K, p$ and etc.. $\langle \mathrm{d}E/\mathrm{d}x\rangle_i$ is mean energy loss rate given by Bethe-Bloch equation for particle species $i$, $\mathrm{d}E/\mathrm{d}x_{\mathrm{measured}}$ is measured $\mathrm{d}E/\mathrm{d}x$ of a certain particle and $R$ is the $\mathrm{d}E/\mathrm{d}x$ resolution. The variable $n\sigma_i$ is used for particle identification in physics analysis.

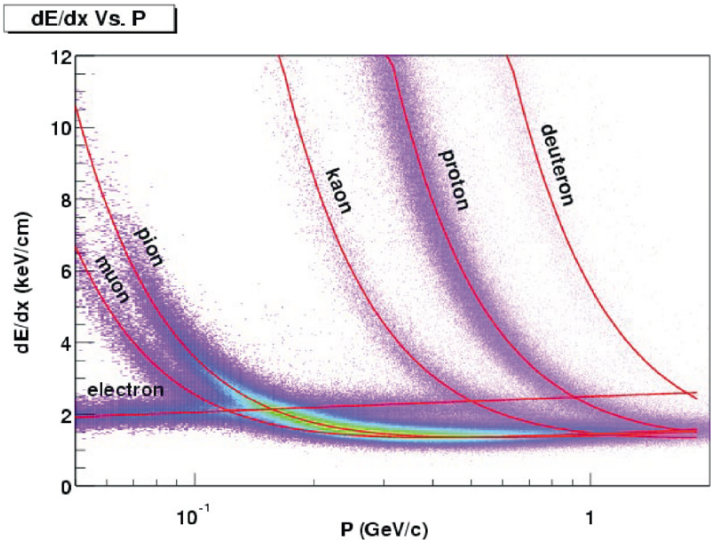


**Figure 2.5**: Ionization energy loss of charged particles in STAR TPC.

### 2.2.2 Fast Detectors

The Time Projection Chamber records comprehensive and complex information, but its readout is slow. To match the high bunch crossing rate of about 9.4 MHz at RHIC and comparatively low data recording rate, i.e. DAQ rate of about 1000 Hz, fast detectors are pipelined in a trigger system in order to select events with physics interests. Below a few fast detectors will be discussed. The trigger system itself will be discussed in the next section.

The Zero Degree Calorimeter (ZDC) [ADG03] is the main detector providing the minimum bias trigger and central trigger. There are two ZDCs in STAR sitting at ~ 18 m from the collision point, beyond the RHIC di-pole magnets. Each ZDC covers ~ 2.5 mrad centered at 0°. The ZDCs are hadronic colorimeters which measure the emitted neutrons near the beam line direction. The di-pole magnets bend the trajectories of charged particles, but not neutrons. Therefore, only outgoing neutrons can reach the ZDCs. The coincidence of the east and west ZDC signals, with each of them is required to be greater than ~ 40% of a single neutron's energy [BCE03], defines a minimum bias trigger. The ZDC coincidence rate is also used to monitor the beam luminosity [Whi98, BCW98]. There are two ZDCs for each of the four experiments at RHIC. The physics analysis discussed in this thesis is based on minimum bias events triggered by ZDC.

STAR Barrel Electro-Magnetic Calorimeter (BEMC) is used to trigger on high $p_T$ processes, including jets, direct photons and heavy quarkoniums. The BEMC consists of 60 modules placed in between the TOF and STAR solenoid magnets, with each module covers 6° in $\phi$ and 1.0 unit in $\eta$ direction, In total, STAR BEMC covers the full azimuthal angle and $|\eta| < 1$. STAR BEMC uses lead and plastic scintillator to sample shower energy deposited in each segments, i.e. BEMC towers. Those towers can be fired by high $p_T$ electrons, photons and $\pi^0$ and the fired towers can be used as a trigger signal. By matching the fired towers and TPC tracks, electrons and photons can be identified. This method can also be used to suppress the pile-up tracks in TPC.

A Time-of-Flight (TOF) detector [SBD06] was fully installed in year 2009, taking the space of the original Central Trigger Barrel (CTB, now retired) between TPC and

BEMC with a coverage of $\phi = 2\pi$ and $|\eta| < 1$. STAR TOF is based on the technology of Multigap Resistive Plate Chamber (MRPC), which consists of a stack of resistive plates with gas filled in between. This structure creates a series of gas gaps. The outer surfaces are applied with electrodes to create a strong electric field in the chamber and make it work in the avalanche mode. Overall, there are 120 TOF trays and each contains 32 MRPC modules inside. The TOF system measures the time of flight of particles between when they are emitted and when they hit one TOF tray. The TOF itself can provide the time when a particle hit on it, i.e. the stop time. The start time is provide by the the Vertex Position Detector (VPD), which is is also regarded as a part of the TOF system. There are two VPD detectors located at $\sim 5.4$ m on the east and west side along the beam direction. The TOF system can be used a trigger detector is because it has very good time resolution. In Au + Au collisions at $\sqrt{s_{NN}} = 200$ GeV, the time resolution of TOF is about $\lesssim 100$ ps including the contribution of VPD.

The other functionality of TOF system, besides as a trigger detector, is that by converting the time of flight of a particle to its speed, different particle species can be identified. This is because that different particles with different mass but the same momentum has different speed. Fig. 2.6 shows the inverse speed for different particles as a function of momentum. TOF can separate pions from kaons up to $p \sim 1.6$ GeV/c and kaons from protons up to $p \sim 3$ GeV/c. Combining the PID capability of TOF and TPC, electrons can be well separated from hadrons, which makes the di-electron analysis possible.

Both of the BEMC and the TOF are used in STAR High Level Trigger, which will be discussed in detail in Chapter 3.

### 2.2.3 STAR Trigger System

In many high energy experiments, the collision rate is much higher than the operation speed of detectors and the rate of data acquisition (DAQ) system, thus a trigger system is needed to reduced the event rate. In the trigger system, faster detectors are used to monitor the happening events and determine whether to start the amplification

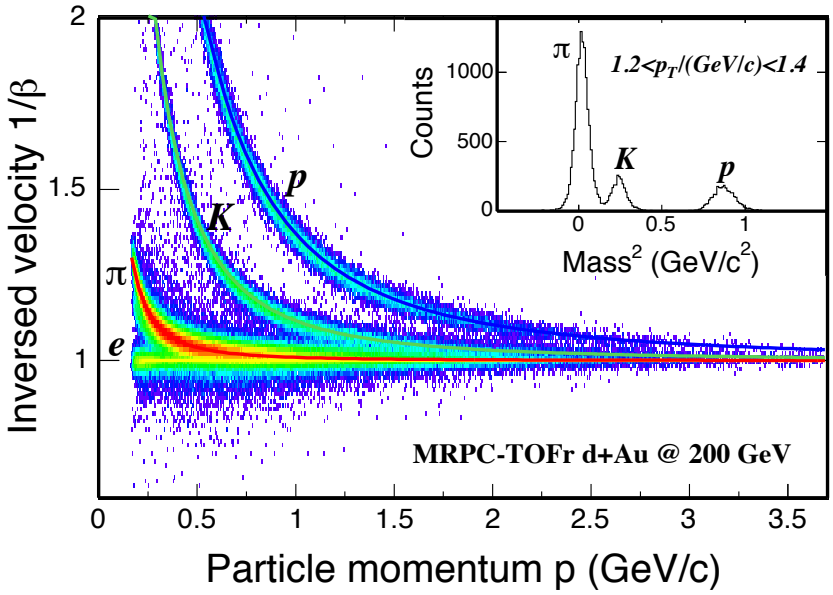


**Figure 2.6**: TOF measured $1/\beta$ as a function of particle momentum. Pions can be separated from kaons up to $p \sim 1.6$ GeV/c and kaons can be separated from protons up to $p \sim 3$ GeV/c. The small plot shows the TOF measured invariant mass, $m^2 = p^2(1/\beta^2 - 1)$. Plot taken from [Don05].

digitization acquisition (ADA) cycle of slow detectors as well as the DAQ system. On the other hand, a large fraction of the collisions are not physically interesting. For instance, beam may hit on the residual gas atoms in the beam pipe making gas event, and it may also hit on the beam pipe making beam pipe events. Such beam-gas background should also be suppressed by the trigger system. A typical trigger system is a chain of fast detectors with buffers in between. Buffers are used to match detectors with different speed. Usually lower level triggers reject events based on simpler criteria containing only one or two variables, while higher lever triggers can do more complicated analysis based on information from multiple detectors. A high level trigger uses PC clusters and making trigger decisions based on analysis very similarly to the offline analysis. Usually higher trigger only works on those events that are not rejected by lower level triggers. Therefore, a trigger system is a hierarchy of detectors. A general review of trigger system can be found in Ref. [LK04].

In STAR, the collision rate for Au + Au events is about 50 kHz and this rate for

high luminosity $p+p$ collisions can reach up to 4 MHz, which is in the same order of magnitude of the RHIC bunch crossing rate. On the other hand, even after two sequential upgrades, the STAR DAQ [LLL03] rate is only 1000 Hz. That means, the STAR trigger system [BCE03, ABD03] should reduce the rate by more than three orders of magnitude, while still meets various of requirements, including triggering on central and minimum bias events in Au + Au and $d$ + Au collisions, triggering on ultra-peripheral collisions, trigger on jets, triggering on cosmic ray events, rejecting background events, minimizing trigger deadtime, opening TPC amplifier grid in < 1.5 ms, accommodating new detectors and etc.. This list can grow when new physics requirements come up.

The STAR trigger system consists of three levels. Level 0 trigger looks at every bunch crossing to determine whether there is a requested interaction happening in this crossing. Level 0 issues a trigger with in 1.5 μs if it detects a interested signal. Every piece of the trigger detectors send information to a data Data Storage and Manipulation (DSM) board. There is a tree of DSM boards at Level 0, analyses are done at every tree level and results are sent the next level. Final results from DSM boards are sent to the Trigger Control Unit (TCU) board in which trigger commands are issued. In Fig. 2.7, the Level 0 DSM tree of the year of 2005 is shown as an example, while the CTB is not used anymore.

Level 1 and 2 trigger do more complex analysis on events that are accepted by Level 0 when selected detector are busy digitizing their data. Level 1 has a time budget of ~ 100 μs and Level 2 has about 5 ms. If an event is accepted by Level 2, then both the detectors and the DAQ system will be notified.

There used to be a Level 3 trigger system [ABD03] based on real time tracking. It had been in limited function since around 2002, but later it lost maintenance because it could not catch up with STAR's DAQ system upgrades. Now it has been replaced by a high level trigger system, which will be discussed in Chapter 3.

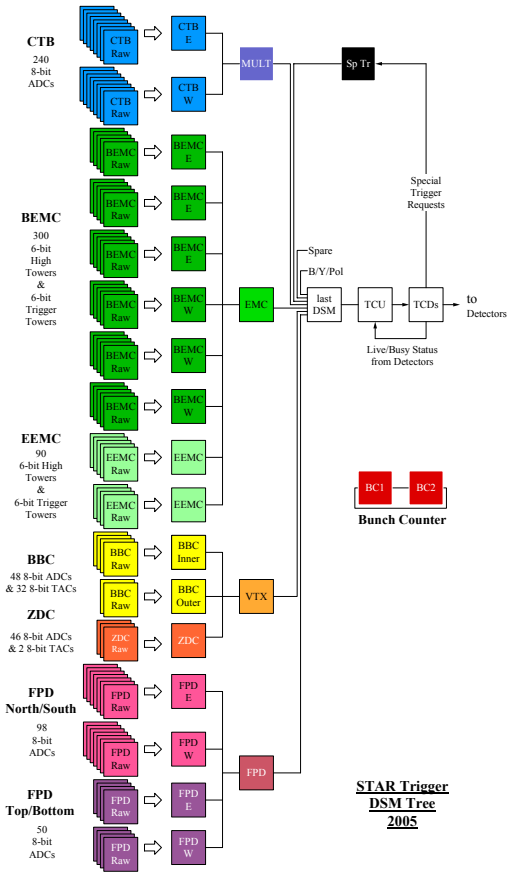


**Figure 2.7**: The DSM tree of the STAR level 0 trigger in 2005. Each detector module send information to a DSM node and the information will be reduced and send to the next tree level. The final tree sum will be sent to the TCU, which will issue trigger commands.

# CHAPTER 3

# The STAR High Level Trigger

At STAR, a typical collision rate is 50 kHz for Au + Au, 1 MHz for $p+p$ $\sqrt{s}$ = 200 GeV collisions, and 4 MHz for $p+p$ $\sqrt{s}$ = 500 GeV collisions. STAR can take data at a rate, after the DAQ1000 upgrade in the year of 2009, as high as 1000 Hz for Au + Au collisions at $\sqrt{s_{NN}}$ = 200 GeV. In section 2.2.3, we discussed a multi-level trigger system which, based on fast hardwares together with simple trigger algorithms, allows STAR to reject most of the background events and reduce the event rate down to a level that can be handled by the DAQ system. At this point, signals from all detectors are digitized and available for further processing. This the place where the High Level Trigger (HLT) is implemented. Equipped with a high performance PC cluster, the HLT collects information from all subsystems, reconstructs a complete event and analyze it in real time, and issue a trigger decision.

In the STAR experiment, HLT will play increasingly important role in event selection because of the continuously increasing RHIC luminosity and the upgraded DAQ capability. In the past a few years, RHIC luminosity has achieved $30 \times 10^{26}$ cm$^{-2}$s$^{-1}$ for Au-Au at 100 GeV/nucleon, $33 \times 10^{30}$ cm$^{-2}$s$^{-1}$ for p-p at 100 GeV and $105 \times 10^{30}$ cm$^{-2}$s$^{-1}$ for for p-p at 255 GeV. In the year of 2014, these numbers are expected to reach $40 \times 10^{26}$ cm$^{-2}$s$^{-1}$, $60 \times 10^{30}$ cm$^{-2}$s$^{-1}$ and $300 \times 10^{30}$ cm$^{-2}$s$^{-1}$ respectively [FBB12]. Fig. 3.1 shows the integrated luminosity delivered by RHIC and the data set recorded by STAR. The rapidly increasing data volume imposes a significant challenge for computing at STAR. A high-level trigger based on full event reconstruction will select events with great physics interest, such as high $p_T$ , di-electrons, exotics and UPC collisions, in order to fully utilize RHIC's high luminosity and STAR's upgraded DAQ capability, as well as deliver measurements timely.

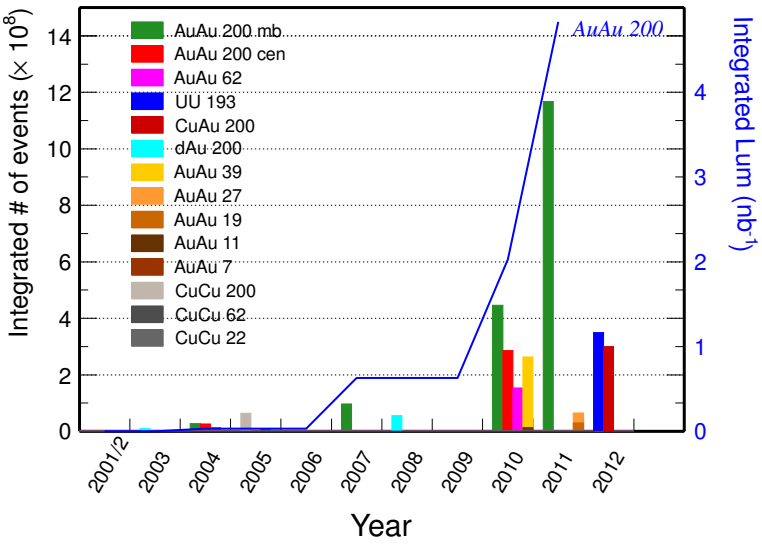


**Figure 3.1**: Heavy-ion minimum bias/central data sets (histograms) and integrated luminosity (line) recorded by the STAR detector. From [Don12].

## 3.1 Overview

The prototype of STAR HLT was tested in 2009, and in 2010 it was included in data taking. In $\sqrt{s_{NN}}$ = 200 GeV Au + Au collisions, the HLT served as an event tagger which tags events that contain three kinds of tracks/track combinations, namely, high $p_T$ track, heavy fragment and di-electron. During the RHIC Beam Energy Scan (BES) program, STAR HLT has been used as an event monitor to select *good events*. The detail of event categories and their corresponding trigger criteria will be discussed later.

The architecture of STAR's current HLT is shown in Fig. 3.2. It consists of two parts, the Sector Level three (SL3) and the Global Level three (GL3). SL3 is made of 24 computers (the TPX computers), each corresponding to one sector of STAR TPC. Cluster finding and track reconstruction are performed in SL3, sector by sector. When tracking is finished, tracks from all sectors are sent to GL3 machines in which they are assembled and analyzed together with information from other subsystems to make a real-time decision on event selection. Two subsystems are currently included in HLT, they are the Time of Flight detector (TOF) and the Barrel Electromagnetic Calorimeter (BEMC). In the future, information from Muon Telescope Detector (MTD) and the Heavy Flavor Tracker (HFT) will also be included.

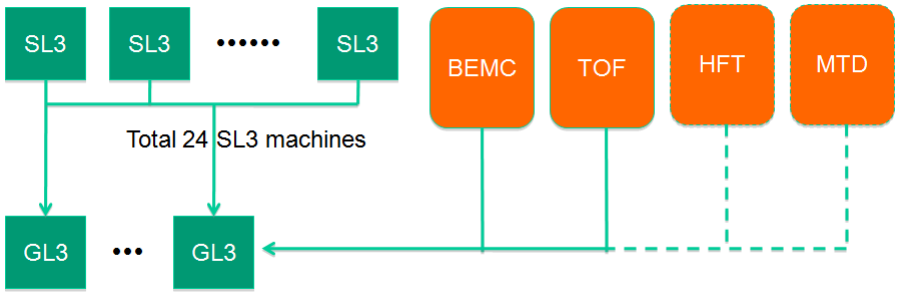


**Figure 3.2**: Architecture of the STAR high-level trigger. Solid lines connect the currently used subsystems and dashed lines connect subsystems that will be included in the future.

### 3.1.1 TPC Track Reconstruction

One of the most computing intensive parts of HLT is the track reconstruction. A typical Au + Au collision at $\sqrt{s_{NN}}$ = 200 GeV can leave more than 30k hits inside the TPC. For central Au + Au collisions and $\sqrt{s}$ = 500 GeV $p+p$ collisions, this number can increase to 70k and 90k, respectively. The latter is even larger than the former due to the pile-up in TPC where earlier or later collisions are also detected as part of the selected collision. Sorting out track information from a collection of hits as large as mentioned above is a significant computing burden. What make this task even more challenging is the time limit. HLT must make a trigger decision before the data being written to tape. That means that the HLT needs to keep up with the speed of the DAQ system, which can be as high as 1000 Hz. A few techniques, including sector tracking, TPC hit mapping, conformal mapping tracking, etc., have been implemented in HLT in order to achieve a high processing speed.

As mentioned before, the SL3 consists of on 24 TPX computers and each of them reconstructs tracks recorded by one TPC sector only. Since TPX machines process data in parallel, 24 times of speed-up is naturally achieved.

The TPC hit map is used to translate a grid point (consisting of sector number, pad row number, pad number and time bucket) to the corresponding corrected hit coordinates $(x, y, z)$. The grid is divided by all 24 sectors, all 45 pad rows, one for every 30 pads and one for every 40 time buckets. The map was developed to combine both the calculation

and correction for TPC hits in one step. The raw TPC signal sent to HLT consists of four integers for each hit, namely, the sector number, the row number, the pad row number and the time bucket number. Hit $(x, y)$ coordinates are calculated for the first three numbers, and the time bucket as well as the measured drift velocity are converted into $z$ coordinate. During the conversion, several corrections are made. Those include the correction on detector shifting and twisting, the correction on non-uniformity of the magnetic field, and the correction on the distortion due to space charge. All of the corrections are made based on offline reconstruction software, and the final, convoluted correction are applied online for each space point in the TPC. Points in between grids are calculated as weighted average of adjacent grids. In this way, all corrections on hit positions are folded in one strike. Because of the TPC hit map the CPU time for hits reconstruction is reduced from ~ 1 s per event to ~ 20 ms per event.

During the tracking process, hits are divided into mutually excluding subsets and tracks are reconstructed by next-hit-on-track finding with a *follow-your-nose* approach. The current STAR HLT tracker is based on conformal mapping, for which the original version was implemented by the STAR Level-3 trigger group [Yep96, ABD03]. In the Conformal mapping, the original coordinates $(x_i, y_i)$ of hit $i$ are transformed to new coordinates $(x_i', y_i')$, where $R_i$ is the distance between hit $i$ and the reference point $(x_t, y_t)$ in $x - y$ plane.

$$x_i' = \frac{x_i - x_t}{R_i^2} \tag{3.1}$$

$$y_i' = -\frac{y_i - y_t}{R_i^2} \tag{3.2}$$

$$R_i^2 = (x_i - x_t)^2 + (y_i - y_t)^2 \tag{3.3}$$

Since the projection of a TPC track in $x - y$ plane is a circle, this transformation makes it a straight line if we choose an arbitrary point along the circle as the reference point. Fig. 3.3 shows the transformation based on conformal mapping. The path length $s$ in $x-y$ plane is proportional to the $z$ coordinate. Therefore, fitting a helix is equivalent to fitting two straight lines, one in $x - y$ plane, one in $s - z$ plane. Once track finding is completed, hits belongs to the same track are transformed back to their original

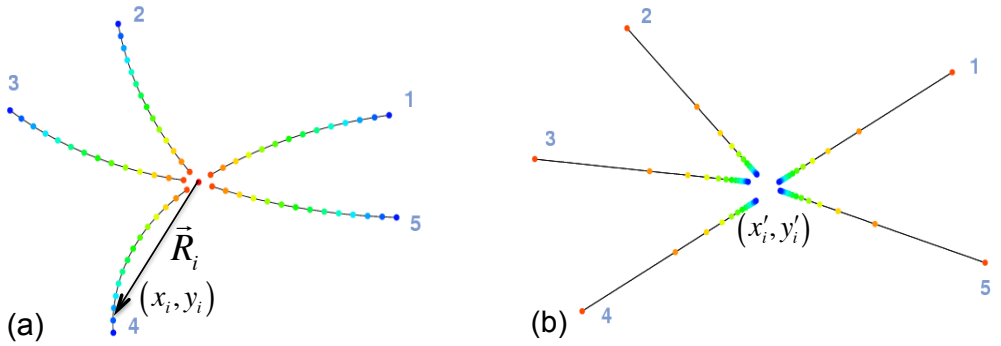


**Figure 3.3**: TPC track projections in $x-y$ plane. (a) Before conformal mapping. (b) After conformal mapping.

coordinates and fitted with a helix model in real space to extract track parameters.

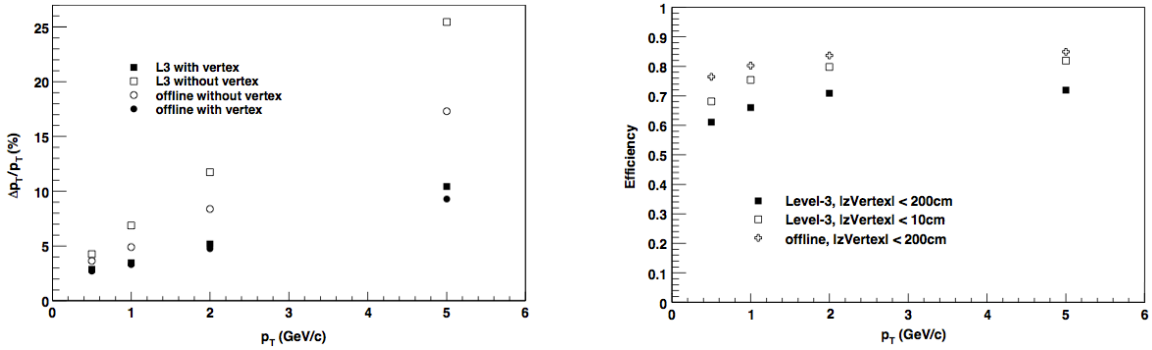


**Figure 3.4**: STAR Level-3 tracker performance determined by Monte-Carlo tracks in Au + Au collision at $\sqrt{s_{NN}}$ = 130 GeV. Left: transverse momentum resolution. Right: tracking efficiency as a function of $p_T$ . Figures taken from [ABD03].

The performance of SL3 tracker has been studied with Monte-Carlo events of Au + Au collisions at $\sqrt{s_{NN}}$ = 130 GeV by the STAR Level-3 trigger group[ABD03]. Tracking efficiency and $p_T$ resolution are shown in Fig. 3.4. Besides Monte-Carlo studies, one is also interested in checking the HLT tracking performance w.r.t. to offline reconstruction. This study is valuable because the offline tracker, combined with careful calibration/tuning under little timing pressure, can be regarded as the best of what one can achieve in practice. Because the HLT tracker and the offline tracker use the same set of hits, this study can be carried out by hits association. In our case, a HLT track is associated with

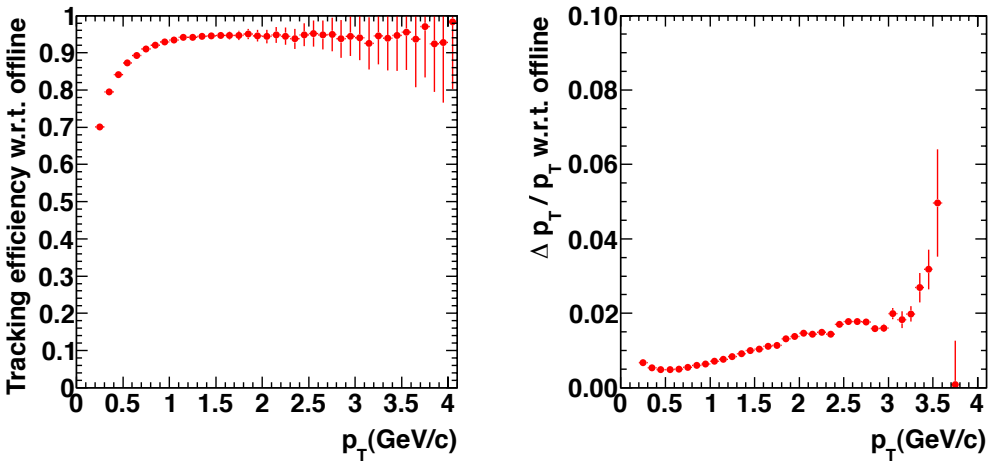


**Figure 3.5**: STAR High Level Trigger tracking performance in Au + Au collisions at $\sqrt{s_{NN}}$ = 200 GeV. Left: Tracking efficiency. Assuming offline efficiency to be one. Right: $p_T$ resolution of reconstructed tracks.

a offline track if they share a minimum of ten common hits out of 45 hits in total. If more than one HLT tracks have more than 10 common hits with an offline track, the one with the most common hits is considered as the reconstructed track and the others, clones. Note that this procedure is the same as that used in evaluating tracking performance with Monte-Carlo tracks, except that here the reference is the offline tracks instead of Monte-Carlo tracks. The tracking efficiency w.r.t. offline and the relative $p_T$ difference between HLT and offline, based on this study with real events of Au + Au collisions at $\sqrt{s_{NN}}$ = 200 GeV, is presented in Fig. 3.5. It is found that the HLT can reconstruct more than 90% of input tracks when $p_T > 1$ GeV. Relative $p_T$ difference between HLT and offline tracker is smaller than 2% when $p_T > 3$ GeV. The low tracking efficiency w.r.t. to offline at low $p_T$ is mainly due to the sector-tracking scheme. Because low $p_T$ tracks tends to cross multiple sectors, there is additional efficiency loss when merging track segments in different sectors into one track.

### 3.1.2 Calibration

The HLT takes great advantage of knowledge and tools available from offline computing. The TOF calibration table was made following the same procedure used in

offline, and was loaded online by the HLT to apply fast corrections. The EMC calibration uses the same gain and pedestal table that are used by STAR's lower level triggers. The TPC $\mathrm{d}E/\mathrm{d}x$ calibration is made by adjusting the $\mathrm{d}E/\mathrm{d}x$ gain with gain factors obtained from the previous run, for inner and outer sectors separately. The calibration for TPC hit position, as mentioned in Sec. 3.1.1, is achieved by folding offline corrections to a multi-dimensional grid, and the correction to each TPC hit is applied according to the weighted mean of grids surrounding the cell that the hit belongs to. The TPC hit map is usually built each year before the run starts, and needs to be updated only when beam energy is changed and/or beam type is changed, e.g. from gold beam to proton beam. Additional corrections that depend on the luminosity are applied with

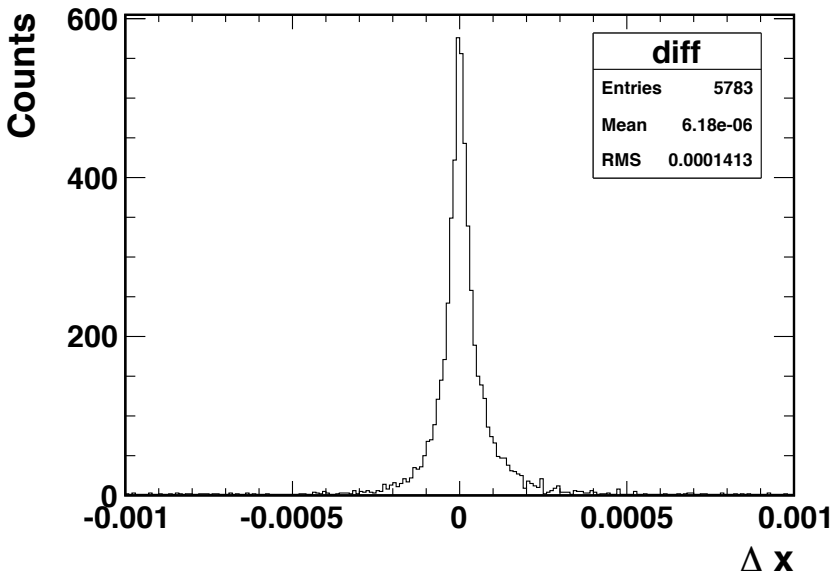


**Figure 3.6**: TPC hits $x$-coordinates difference between offline reconstruction and HLT TPC map reconstruction.

live input from STAR's Beam Beam Counter coincidence rate, which follows closely the RHIC luminosity. A similar calibration procedure can be used in the future for HFT and MTD. With the calibration the difference between the TPC hit position from the HLT an that from offline is on the order of 0.03 cm (Fig. 3.6), which is smaller to the typical hit errors (0.1 cm). After the calibration the EMC energy resolution is 15%, and the TOF timing resolution can reach down to ~ 90 ps. Both are comparable to offline achievements to the first order.

### 3.1.3 Online monitoring

During data taking, HLT consistently generate QA plots of triggered events counting, multiplicity, track parameters, vertex position, beam line position, etc. Online monitoring helps us identify run time problems in real time. In Fig. 3.7, a few online monitoring plots are shown to demonstrate the monitoring functionality.

### 3.1.4 Event Selection and Physics Results

During RHIC run from 2010 to 2012, STAR HLT has been used to successfully select events containing heavy fragments, di-electrons and high $p_T$ tracks. In particular events triggered or tagged by the first two triggers have been analyzed and yielded important physics results. The trigger details and the corresponding physics achievements are discussed below.

In heavy ion collisions, most of the produced final state particles are single hadrons, like $\pi$, $K$ and $p$. However, there are probabilities to form stable combined states, such as deuteron, triton, helium-3, helium-4 and their anti-particles. Here those are collectively called heavy fragments. Thermal model [BS07] and coalescence model [SY81] are usually used to estimated the yields of these rare particles. The presence and the yield of heavy fragments carry important information about the production dynamics under extreme conditions. In particular, the existence of particles like anti-helium-4 has significant implications in cosmology. If anti-helium or even heavier anti-nuclei are observed with the sensitivity of current space-based detector, such as the Alpha Magnetic Spectrometer [ABB94], it may imply that large amount of anti-matter exist elsewhere in the Universe. Thus the existence and the yield of anti-helium 4 in accelerator collider experiments can serve as a baseline for the study of its origin in cosmos. In HLT, charge-2 particles can be separated from others on the plot of $(\mathrm{d}E/\mathrm{d}x)$ versus rigidity, as shown as red points in Fig. 3.8. By comparing to the theoretically expected values (curves) for each particle species, we can identify charge-2 particles and their anti-particles. The heavy fragment trigger is set to take events that had at least one track with a $\mathrm{d}E/\mathrm{d}x$ that is larger than a threshold set to three standard deviations below the expected value for helium-3

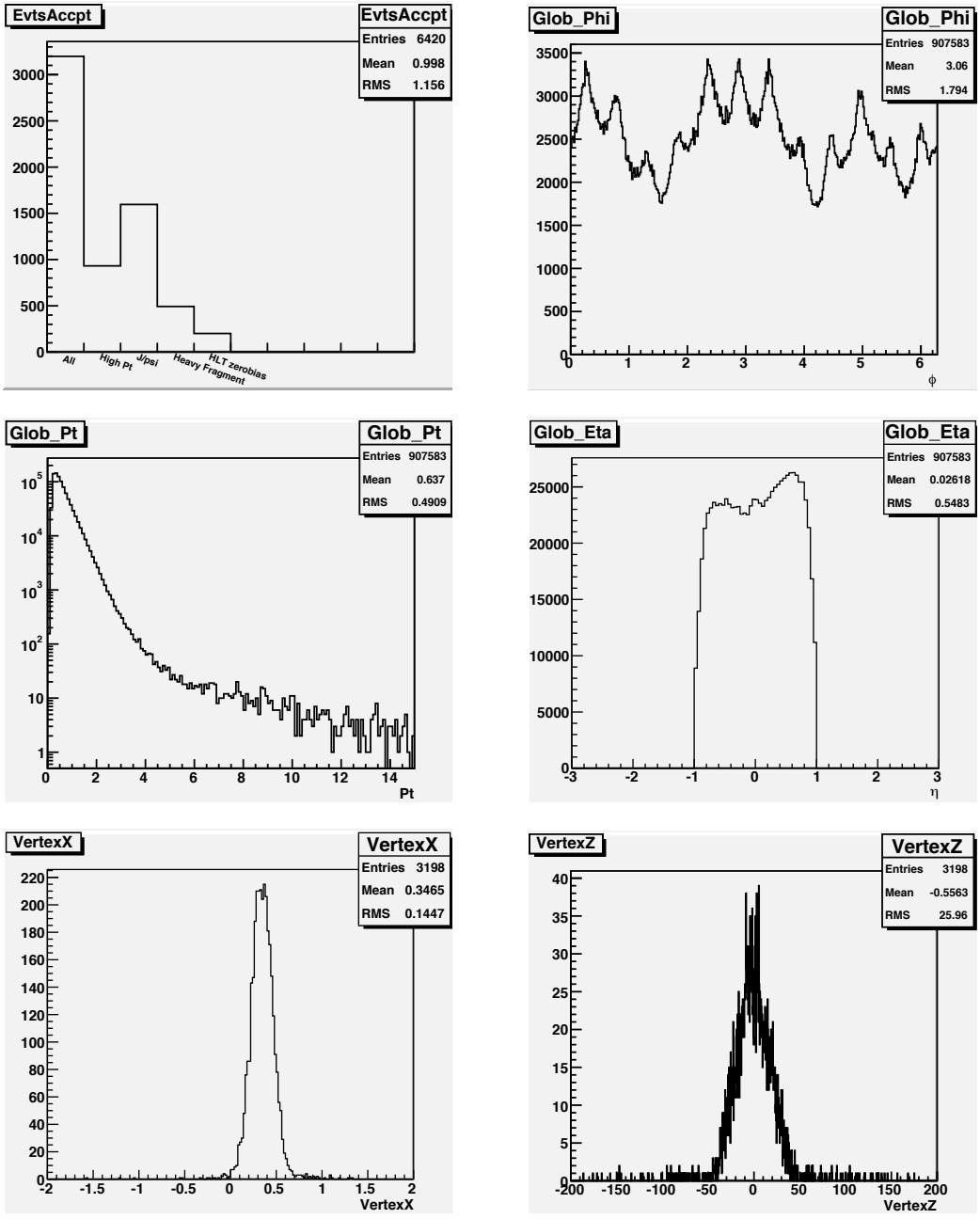


**Figure 3.7**: Selected online monitoring plots of High Level Trigger from run 11071066 in year 2010. From up down, left to right, the plots show the real time accumulate statistics of the number of event being accepted by HLT, the azimuthal angle $\phi$, transverse momentum $p_T$ and pseudo-rapidity $\eta$ distribution of global tracks and the position of primary vertices.

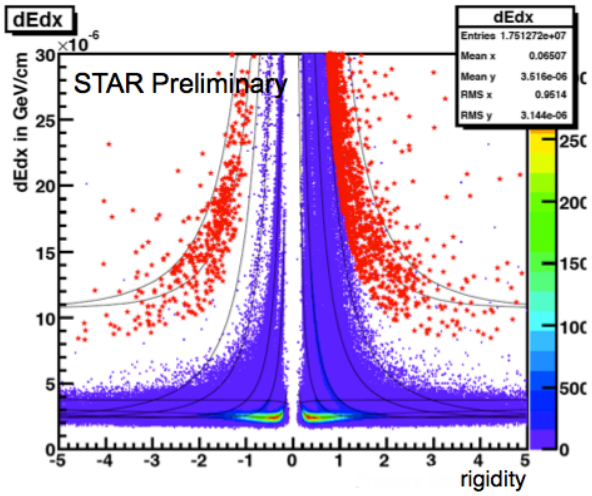


**Figure 3.8**: TPC ionization energy lose, d$E$/d$x$, for charged particles. Red dots represent the charge-2 candidates trigger by STAR HLT.

at the same rigidity. Events triggered by HLT are sent to a particular data stream for express processing and analyzing. With the combined PID capability of TPC and TOF, as shown in Fig. 3.9, STAR has found 16 $^4\overline{He}$ in $\sqrt{s_{NN}}$ = 200 GeV Au + Au collisions. This discovery has been published in *Nature* [AAA11] and has attracted a fair amount of media attention from around the world.

Di-electrons are useful electromagnetic probes, as real and virtual photons (detected as di-electron or di-muons) are emitted from the entire reaction volume throughout the evolution of a heavy-ion collision. Once created, most of them leave the interaction volume unchanged due to their negligible final-state interaction with the medium. Electromagnetic probe are unique because they give direct access to the in-medium modifications of hadronic states via di-lepton invariant mass spectra. Furthermore, electromagnetic probes can be used to infer the temperature of the system during its hottest phase via direct thermal photon and di-lepton radiation [**?**]. Di-electrons are also useful for heavy quark measurements. It has been shown that elliptic flow of baryons and mesons converges when scaled by their Number of Constituent Quarks (NCQ) [AAA04a, AAA07], which implies that particles are produced by coalescence. However, heavy quarks (charm and beauty) are expected to thermalize much more slowly than light partons, and exhibit a different flow pattern. Thus the measurement of the elliptic flow of heavy flavors offers

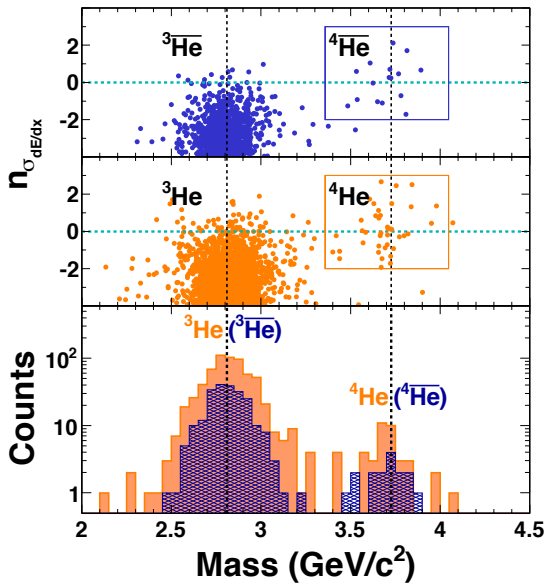


**Figure 3.9**: TPC and TOF combined particle identification for $^4\overline{He}$. TPC gives the ionization energy lose, while TOF gives the invariant mass of particles. Figure taken from [AAA11].

insights into the mechanism of rapid thermalization. In HLT, the di-electron trigger select events with high $p_T$ electron pairs. Electron pairs are identified by the combined information from TPC d$E$/d$x$ and the TOF detector. In addition, electrons' trajectory are required to match a BEMC tower with energy greater than a threshold of 0.5 GeV. The momenta of the electron and positron are required to be larger than 1.4 GeV and 1.2 GeV respectively. Fig. 3.10 shows the invariant mass distribution of electron and positron pair trigger by HLT as well as the like sign background.

STAR HLT also triggered events with high $p_T$ particles for studying hard processes. Fig.3.12 shows transverse momentum distribution of HLT triggered high-$p_T$ events. The two jumps at $p_T$ = 6 and 7.5 GeV reflect the trigger enhancement.

When the collision energy is around or below $\sqrt{s_{NN}}$ = 11 GeV, backgrounds from beam on beam-pipe collisions are quite substantial at STAR. For instance, in Au + Au collisions at $\sqrt{s_{NN}}$ = 7.7 GeV only about 3% of the events are from real collisions. Because of this, a cleaner signal is necessary for both accelerator tuning and counting of events towards the physics goal. The lower level triggers do not help here because they

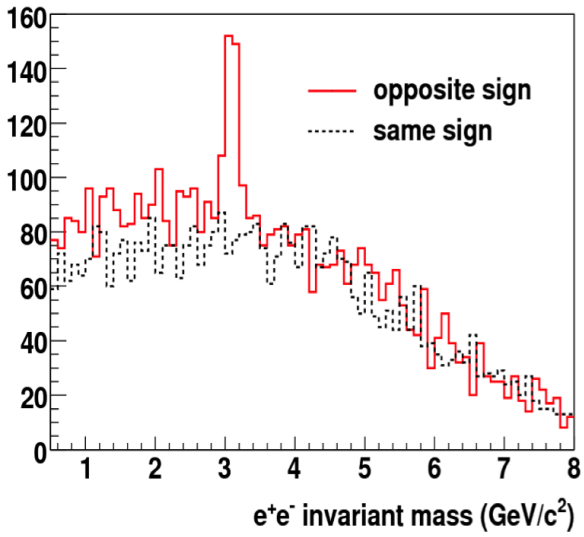


**Figure 3.10**: Invariant mass distribution of electron and positron pair trigger by HLT and the like sign background.

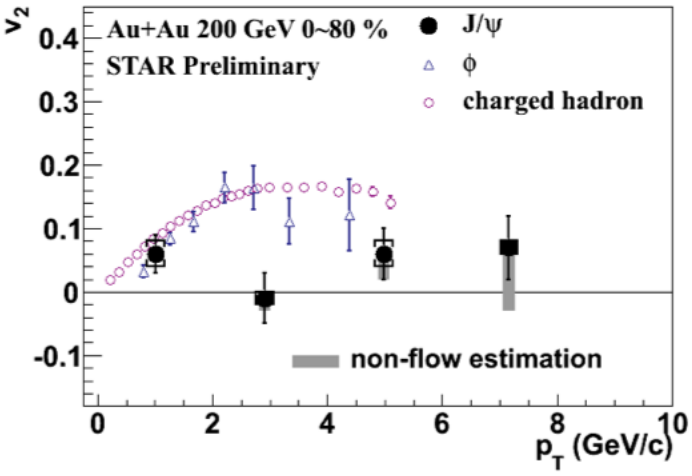


**Figure 3.11**: Elliptic flow of $J/\psi$ in Au + Au Collisions at $\sqrt{s_{NN}}$ = 200 GeV.

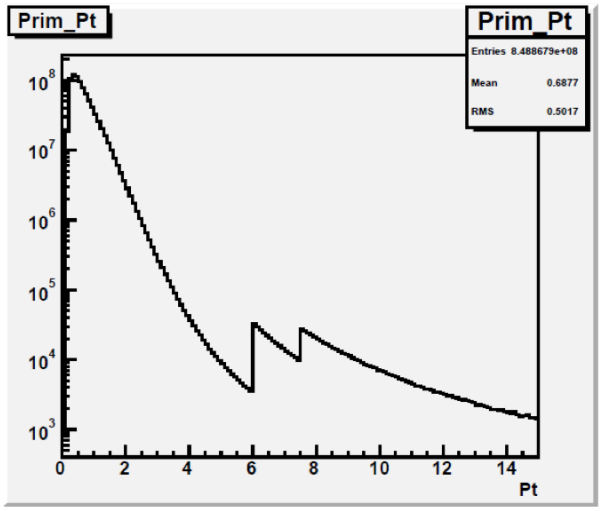


**Figure 3.12**: Transverse momentum distribution of HLT triggered high-$p_T$ events.

are optimized for efficiency rather than background rejection. Since the HLT reconstructs the 3-dimensional primary vertex position online, it has been used to provide the fraction of good events as live feedback to the STAR experiment and the Collider Accelerator Department. Fig. 3.13 shows the primary vertices reconstructed by STAR offline software and HLT in Au + Au collisions at $\sqrt{s_{NN}}$ = 7.7 GeV. The left panel clearly shows the beam pipe events while the good vertices around the original point can also be found in the right panel which is produced by STAR HLT. The overall efficiency and purity of the HLT tagged "good events" were both 95%.

More details about the STAR high level trigger data processing, trigger set-up and online calibration can be found in [Qiu11].

## 3.2 Upgrade plan for the STAR HLT

### 3.2.1 Hardware upgrade

As mentioned previously in Sec. 3.1.1, in the current setup the HLT reconstructs tracks with clusters within one sector. In total there are 24 DAQ machines (2 quadcore, 2.6 GHz) and each of them takes care of cluster finding and sector tracking for one TPC sector. The advantages of tracking with DAQ machines are that i) data is already in the

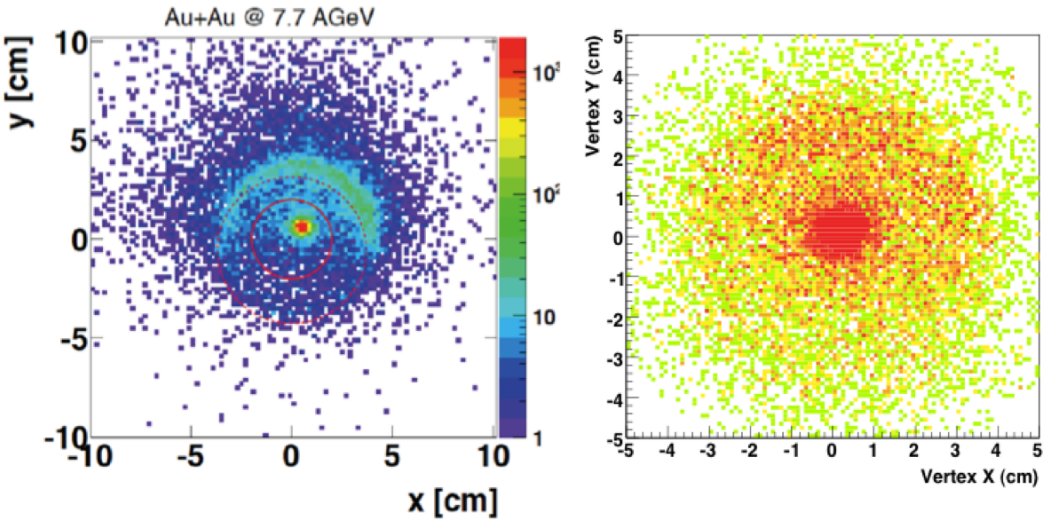


**Figure 3.13**: Primary vertices reconstructed by STAR offline software (left) and HLT (right) in Au + Au collisions at $\sqrt{s_{NN}}$ = 7.7 GeV.

memory, no additional time is needed for I/O, and ii) tracking is performed in parallel for 24 TPC sectors. This setup had worked well in run 2009 and run 2010. However, because of the continuously increasing luminosity, starting from run 2011 those DAQ computers were overloaded with tasks of cluster finding thus little CPU resource were left for HLT tracking. When this happens, HLT has to be taken out of the run in order to ensure that the cluster finding has the maximum CPU resource, so that the DAQ experience the slowing down as less as possible. This happened occasionally in run 2011 and it happened definitely in run 2012. To ensure that HLT can continue to operate, it is planned to build a dedicated computer farm for the HLT, starting with a small computer cluster in 2013 with the possibility of expansion in the future. This way HLT will not interfere with STAR's *normal* data flow, and no longer compete with DAQ system for computing resources. Running HLT independently will also increase the robustness of the system, and retain the scalability for further upgrades, in terms of hardware and software architecture, according to specific requirements.

### 3.2.2 Software upgrade : Cellular Automaton Tracking, Kalman Filter track fitting and Kalman Filter particle reconstruction

In this section, we will first discuss track reconstruction techniques and the Cellular Automaton tracker to be adopted by the STAR HLT, followed by the Kalman Filter particle reconstruction.

Tracking technique has advanced over decades, from the recognition by human eyes in early years when using bubble and cloud chamber and when both the multiplicity and data volume are low, to track finding algorithms that intensively rely on parallel computing to process huge amount of data from accelerator collider experiments. However, the general track reconstruction procedure is still the same. The first step, which is called track finding or pattern recognition, is to sort out hits and/or other measurements which belong to a track. The second step, the tracking fitting, is to fit those hits that are believed to come from the same track to obtain track parametrization. Usually track finding and track fitting are related but separate steps. However, in some of the recent adaptive algorithms, they are merged.

Reviews of the tracking methods can be found in [Gro87, Man04, SF10, Kis08]. Conformal mapping method (used in SL3) and the Hough transform method are the two simplest traditional methods. As discussed before conformal method transform a circle into a straight line, which makes the track finding and track fitting easier. Hough transform method takes a different approach – with proper transformation it solves the problem directly in parameter space in stead of measurement space. For instance, for a straight line track parametrization, $y = ax + b$, the parameters $a$ and $b$ need to be determined from the measurement space points $(x_i, y_i)$. In stead of solving this problem in measurement space, Hough transform method transfers the track model into parameter space and obtain, $b = -ax + y$. In this case, each measurement point $(x_i, y_i)$ gives a straight line in the $a-b$ plane. All of the straight lines given by measurements will make a peak somewhere in the $a-b$ plane, which indicate the values of desired parameters $a$ and $b$. Conformal mapping method and Hough transform method are usually classified

as global methods, which treat all measurements simultaneously. On the contrary, local methods treat measurements sequentially, e.g. search for the next hit following some track segments.

One of most widely used tracking method in current high energy physics experiments is the Kalman Filter method. It was originally developed by R.E. Kalman in 1960 to deal with discrete-data linear filtering problem [Kal60], and was introduced to the high energy physics community for track finding and track fitting in 1980s [Fru87]. In contrast to traditional methods, the Kalman Filter does not need to know all hits of a certain track at the first place, and it adds hits in sequential steps. Track parameters are optimized at each step with the recently added hit, and are used in the projection to find the next hit. Details of the Kalman Filter will be discussed later.

Another group of methodology of track reconstruction is the adoptive method, it includes the combinatorial Kalman filter method [MS99] and the neural networks [Den88, Pet89]. In adoptive methods, the track finding and track fitting are performed in a single step. It is not in the plan to use those methods in STAR HLT thus they won't be discussed in details.

#### 3.2.2.1 Cellular Automaton Track Finding

The Cellular Automaton (CA) track finding, a recent tracking algorithm described in Ref. [GKK93, KKK97, Kis06], can be regarded as a hybrid method in between local and global methods. As illustrated in Fig. 3.14, the CA tracker starts track finding with the building up of track segments, then it connects track segments according to track models. When track segments are connected, links between hits are established and bad links are removed. Good track candidates will survive and be available for track fitting.

The process of building track segments, also called seeding, is a crucial step in the CA tracker. In this process, a hit from a certain layer is selected and its connections to hits in the upper and lower layers are made. With those connections, all possible routes are established, each consisting of two line segments. The best route is the one that is close to a straight line the most. This is determined by finding the route with the

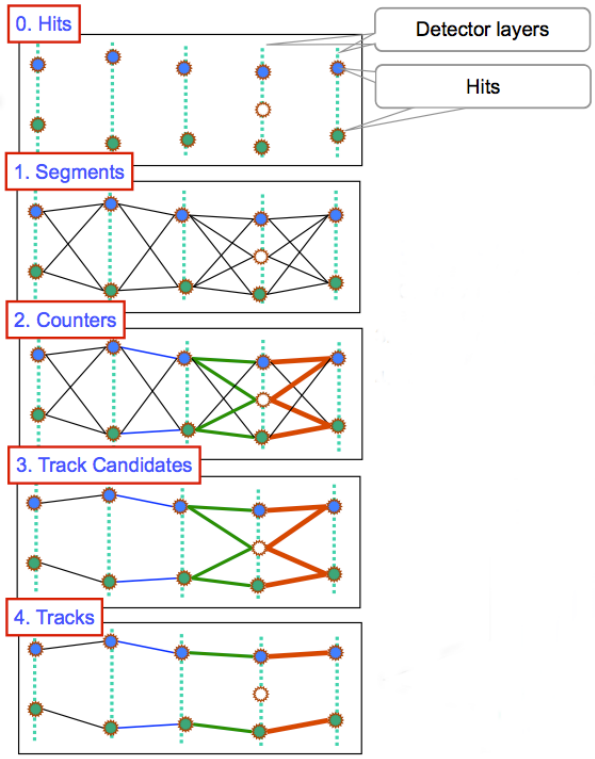


**Figure 3.14**: Track finding steps based on cellular automaton

minimum $\widetilde{\mathrm{d}s}^2$ quantity as defined Eq. (3.7). Meanings of other variables used in Eq. (3.7) are illustrated Fig. 3.15. The slope difference between the upper and lower line segment of a route is given by Eq. (3.4) and Eq. (3.5), for y and z direction, respectively. The combined difference, defined in Eq. (3.6), needs to be minimum for a route to be chosen as the best one. In the case of STAR and ALICE TPC, $\mathrm{d}x$ is the difference between pad rows and thus is fixed by the TPC geometry. Therefore, finding the minimum $\mathrm{d}s^2$ is equivalent to finding the minimum $\widetilde{\mathrm{d}s}^2$. In addition to being the minimum, $\mathrm{d}s^2$ is also required to be smaller than a predefined $\chi^2$ cut. That is, $\min\left[\widetilde{\mathrm{d}s}^2\right] < \chi^2 \mathrm{d}x_u^2 \mathrm{d}x_d^2$. Routes that satisfy the requirements are selected and available for further processing. This procedure is called *Neighborhood finding*.

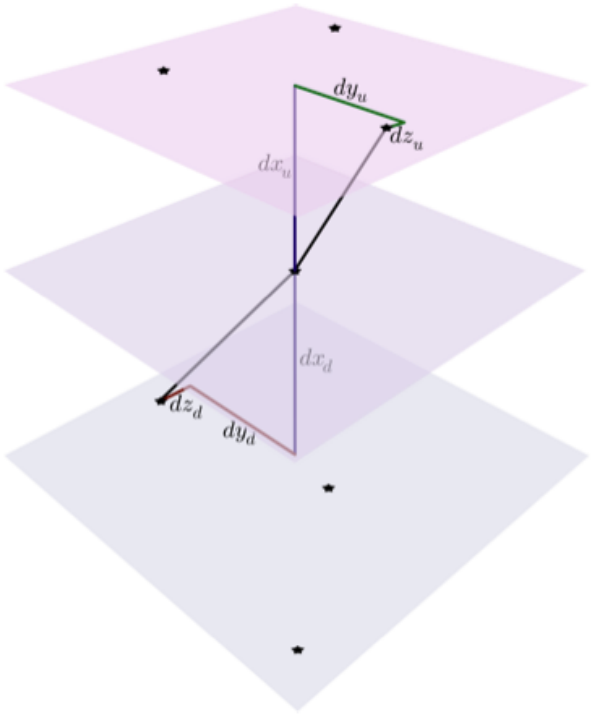


**Figure 3.15**: Neighborhood Finding for a hit in cellular automaton tracker. From [Kre09].

$$\begin{aligned} \mathrm{d}s_y &= \frac{\mathrm{d}y_d}{\mathrm{d}x_d} - \frac{\mathrm{d}y_u}{\mathrm{d}x_u} \\ &= \frac{\mathrm{d}y_d\mathrm{d}x_u - \mathrm{d}y_u\mathrm{d}x_d}{\mathrm{d}x_u\mathrm{d}x_d} \end{aligned} \tag{3.4}$$

$$\begin{aligned} \mathrm{d}s_z &= \frac{\mathrm{d}z_d}{\mathrm{d}x_d} - \frac{\mathrm{d}z_u}{\mathrm{d}x_u} \\ &= \frac{\mathrm{d}z_d\mathrm{d}x_u - \mathrm{d}z_u\mathrm{d}x_d}{\mathrm{d}x_u\mathrm{d}x_d} \end{aligned} \tag{3.5}$$

$$\begin{aligned} \mathrm{d}s^2 &= \mathrm{d}s_y^2 + \mathrm{d}s_x^2 \\ &= \frac{(\mathrm{d}y_d\mathrm{d}x_u - \mathrm{d}y_u\mathrm{d}x_d)^2 + (\mathrm{d}z_d\mathrm{d}x_u - \mathrm{d}z_u\mathrm{d}x_d)^2}{\mathrm{d}x_u^2\mathrm{d}x_d^2} \end{aligned} \tag{3.6}$$

$$\begin{aligned} \widetilde{\mathrm{d}s}^2 &= \mathrm{d}s^2\mathrm{d}x_u^2\mathrm{d}x_d^2 \\ &= (\mathrm{d}y_d\mathrm{d}x_u - \mathrm{d}y_u\mathrm{d}x_d)^2 + (\mathrm{d}z_d\mathrm{d}x_u - \mathrm{d}z_u\mathrm{d}x_d)^2 \end{aligned} \tag{3.7}$$

The neighborhood finding procedure are repeated until neighbors are exhausted for all hits in all layers, and at the end, links between hits are made, as shown in the stage 2 and 3 in Fig. 3.14. Every linked hit has two neighboring hits from upper and lower layers, except the ones from the inner most and outer most layer. Only one-to-one mutual links

are kept and others are removed. Those survived hit chains, connected by bi-direction links, are relatively good track candidates and can be used as the input for track fitting.

In stage 2 and 3, tree-like structures appear following the simple rule of neighborhood finding. Analogies between the track finding and the game of "Life" can be recognized [Kis08]. This is where the name of cellular automaton coming from.

The cellular automaton track finding has several advantages. Firstly, the arithmetic is quite simple, as shown in Eq. (3.4 – 3.7). Secondly, the data requirement has a good locality. Because one only needs to consider hits from the two adjacent detector layers, and the data can be arranged together in memory naturally. Thirdly, even the track segment building is performed locally, the resulting track candidates are completed at the global level. In low hit density cases, these track candidates can be used almost directly. In the case of high hit density, they are good seeds for track fitting methods, e.g. the Kalman Filter.

Because of the simple mathematics used in track finding, the core part can be vectorized by using SIMD instructions shipped with most modern CPU chips. In addition, building links for hits are tasks that are independent of each other. Therefore, it is intrinsically a parallel algorithm.

#### 3.2.2.2 Kalman Filter Track Fitting

It is planned in STAR HLT to apply the Kalman Filter track fitting after the CA tracking. The core of the Kalman Filter (KF) consists of a set of mathematical equations which efficiently give the optimized estimation of the inner state of a dynamic system. The optimization here is achieved by minimization the squared error. Any system that has a inner state varying with respect to time is a dynamic system. Given its general usability and suitability for computer process, Kalman filter has been widely applied in areas like process control, navigation, spacecraft tracking, etc..

Kalman filter was introduced to high energy physics for track reconstruction in 1980s by R. Frühwirth [Fru87]. This method was called *progressive* track fitting method [Bil84, BFR85] at the beginning and then later recognized as an application of the

Kalman filter. In the language of Kalman filter, a given dynamic system is determined by a state vector $\boldsymbol{x}$. The system equation Eq. (3.8) describes how the state vector propagates from time $k-1$ to $k$.

$$\boldsymbol{x}_{k,t} = \mathbf{F}_{k-1}\boldsymbol{x}_{k-1,t} + \boldsymbol{w}_{k-1} \tag{3.8}$$

The measurement equation Eq. (3.9) describes the relationship between the the state vector $\boldsymbol{x}$ and our measurement $\boldsymbol{m}$ at time $k$.

$$\boldsymbol{m}_k = \mathbf{H}_k\boldsymbol{x}_{k,t} + \boldsymbol{\epsilon}_k. \tag{3.9}$$

Here $t$ represents the true values. Matrices $\mathbf{F}$ and $\mathbf{H}$ describe the time evolution and measurement of the system, respectively. $\boldsymbol{w}$ and $\boldsymbol{\epsilon}$ are random noise, namely, process noise and measurement noise, respectively. It is required that the noise has zero mean, i.e. $E\{\boldsymbol{w}\} = 0$ and $E\{\boldsymbol{\epsilon}\} = 0$. A few covariance matrices can also be defined,

$$\mathbf{R}_k^i = \mathrm{cov}\{\boldsymbol{r}_k^i\} \tag{3.10}$$

$$\mathbf{Q}_k = \mathrm{cov}\{\boldsymbol{w}_k\} \tag{3.11}$$

$$\mathbf{V}_k = \mathbf{G}_k^{-1} = \mathrm{cov}\{\boldsymbol{\epsilon}_k\} \tag{3.12}$$

The covariance of the difference between the estimation and the true value is

$$\mathbf{C}_k^i = \mathrm{cov}\{\boldsymbol{x}_k^i - \boldsymbol{x}_{k,t}\} \tag{3.13}$$

where the estimation of $\boldsymbol{x}_k$ using measurement up to time $i$ is denoted by $\boldsymbol{x}_k^i$.

The first stage of Kalman filter is the *prediction* stage. According to the system equation Eq. (3.8), one can estimate the state vector as well as the covariance matrix with the measurements 1 through $k-1$.

$$\boldsymbol{x}_k^{k-1} = \mathbf{F}_{k-1}\boldsymbol{x}_{k-1} \tag{3.14}$$

$$\mathbf{C}_k^{k-1} = \mathbf{F}_{k-1}\mathbf{C}_{k-1}\mathbf{F}_{k-1}^T + \mathbf{Q}_{k-1} \tag{3.15}$$

With the measurement equation Eq. (3.8), one can predict the measurement at time $k$ and define the true measurement as well as the predicted measurement as residuals

$$\boldsymbol{r}_k^{k-1} = \boldsymbol{m}_k - \mathbf{H}_k\boldsymbol{x}_k^{k-1} \tag{3.16}$$

while the covariance matrix of the residuals is

$$\boldsymbol{R}_k^{k-1} = \boldsymbol{V}_k + \mathbf{H}_k \mathbf{C}_k^{k-1} \mathbf{H}_k^T \tag{3.17}$$

The next stage is the *filtering* stage. The stage vector in time $k$, $\boldsymbol{x}_k^k$, should be very close to $\boldsymbol{x}_k^{k-1}$. The difference should be related to the residuals, which is involved the measurement in time $k$, $\boldsymbol{m}_k$. Therefore,

$$\boldsymbol{x}_k = \boldsymbol{x}_k^{k-1} + \mathbf{K}_k \left( \boldsymbol{m}_k - \mathbf{H}_k \boldsymbol{x}_k^{k-1} \right) \tag{3.18}$$

Here $\boldsymbol{x}_k^k$ is simplified as $\boldsymbol{x}_k$. $\mathbf{K}_k$ is called gain matrix. What makes the Kalman filter special is the choice of the gain matrix. Kalman filter choose the gain matrix to minimize the mean of square error. One form of such gain matrix is

$$\mathbf{K}_k = \mathbf{C}_k^{k-1} \mathbf{H}_k^T \left( \mathbf{V}_k + \mathbf{H}_k \mathbf{C}_k^{k-1} \mathbf{H}_k^T \right)^{-1} \tag{3.19}$$

$$= \mathbf{C}_k \mathbf{H}_k^T \mathbf{G}_k. \tag{3.20}$$

The covariance matrix, residuals and the covariance matrix of residuals are also updated in the filtering stage.

$$\mathbf{C}_k = \left(1 - \mathbf{K}_k \mathbf{H}_k\right) \mathbf{C}_k^{k-1} \tag{3.21}$$

$$\boldsymbol{r}_k = \boldsymbol{m}_k - \mathbf{H}_k \mathbf{K}_k = \left(1 - \mathbf{H}_k \mathbf{K}_k\right) \boldsymbol{r}_k^{k-1} \tag{3.22}$$

$$\mathbf{R}_k = \left(1 - \mathbf{H}_k \mathbf{K}_k\right) \mathbf{V}_k = \mathbf{V}_k - \mathbf{H}_k \mathbf{C}_k \mathbf{H}_k^T \tag{3.23}$$

The $\chi^2$ increment is

$$\chi_k^2 = \chi_{k-1}^2 + \chi_+^2 \tag{3.24}$$

$$\chi_+^2 = \boldsymbol{r}_k^T \mathbf{R}_k^{-1} \boldsymbol{r}_k \tag{3.25}$$

At this stage, estimation at time $k$ is made based on all measurements up to time $k$, which is an optimized, most up-to-date estimation. If one has measurements in the future, for example at time $k+1$, they can also be used to update the estimation at time $k$. This stage is called *smoothing* stage. Details of the smoothing is not covered here because in track reconstruction the smoothing stage is not necessary and thus bypassed.

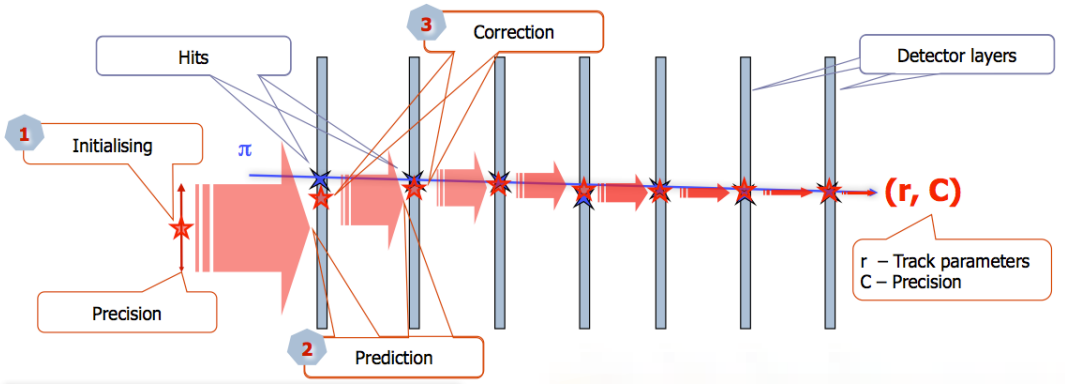


**Figure 3.16**: Fit track parameters with Kalman filter.

A track trajectory recorded by the detector can be regarded as a dynamic system if one view hits from the same track lining up in time series. The system's state vector consists a set of track parameters. in Kalman filter track fitting starts from an arbitrary initial value $\boldsymbol{r}$ and adds hits one at a time. With the last hit being added, one obtains the optimized track parameters as well as the corresponding covariance matrix. The Kalman filter based fitting process is illustrated in Fig. 3.16.

In most high energy physics experiments, the track reconstruction takes most of the event reconstruction time. Thus it is desirable to make the tracking run as fast as possible. Similar to what is done to the CA track finder, the Kalman filter has also been vectorized in order to fully utilize the computing power of CPU's. It has been reported that the vectorized version of Kalman filter track fitting program runs orders of magnitude faster than the original version [GKK08].

#### 3.2.2.3 Kalman Filter Particle Reconstruction

The idea of Kalman filter can be extended to reconstruct decay vertices and primary vertex [GK07]. In this case, reconstructed tracks are used as measurements to estimate the state of their mother particle, which can be a neutral particle or even a primary vertex. The software package that implements this idea is named KFParticle. Instead of fitting tracks by using hits, KFParticle fits primary and decay vertex by using tracks. The parameters of vertices are obtained as components of the state vector after the filtering process. KFParticle gives unified treatment on the primary and secondary

vertex finding. Since it is also based on Kalman filter and the track parameters as well as the corresponding covariance matrix are available for use, KFParticle does the vertex finding very fast. On the other hand, using KFParticle to reconstruct secondary vertex is different from the transitional topological reconstruction technique. Some key quantities, like distance of closest approach (DCA) between two helices, have build-in counter-part in KFParticle. Because the Kalman filter only involves matrix operations inside, it is much faster than the calculation based on geometry, which is usually performed by numerical iterations and is slow.

### 3.2.3 Integration

The CA tracker developed by the GSI-Frankfurt group uses vectorization, multi-threading and the General Purpose GPU (GPGPU) to accelerate the track reconstruction at different levels. It has been demonstrated to have good precision, high speed, and more importantly, high scalability. The CA tracker has been used in the high-level trigger of LHC/ALICE experiment and offline track seeding of RHIC/STAR experiment. It will also be used in the online triggering and offline data analysis of CBM experiment at FAIR/GSI. In STAR, it is an on-going effort of replacing the old HLT tracker, based on conformal mapping, by the CA tracker in order to obtain better tracking quality and high scalability. This replacement will put STAR HLT in a good position to benefit from future expansion of the online computer farm with new hardware, so that the full power of parallel computing can be exploited.

A few issues need to be sorted out in order to run the CA tracker in STAR HLT environment. As discussed in Sec. 3.1.1, STAR HLT uses a TPC hit map to reconstruct and correct hit position in one step. The resulting hits are defined in STAR's global coordinates. Since the CA tracker does the sector-tracking in sector's local coordinates, coordinates of TPC hits need to be transformed before being fed into CA tracker. The transformation is to rotate hits in all sectors to the super sector, sector 12, that is, rotate

by an angle $\alpha$,

$$\alpha = \begin{cases} i \cdot \frac{\pi}{6} & \text{if } 1 \le i \le 12, \\ (24 - i) \cdot \frac{\pi}{6} & \text{if } 13 \le i \le 24. \end{cases} \tag{3.26}$$

while $i$ is sector number. After the rotation, $x$ and $y$ are swapped while the sign of $z$ is changed. The direction of magnetic filed is reversed because that $z$ is reversed.

The CA tracker finds track candidates sector by sector, with only hits within each sector. This way hit-searching volume is reduced and the speed is increased. It also makes sector tracking tasks independent of each other, which means, they can be executed in parallel if necessary. After the sector tracking, a merger algorithm is applied to merge tracks crossing sector boundaries. Tracks found by the CA tracker contain no information/knowledge of the primary collision vertex, although many of them are physically originated from the primary vertex. From the software point of view, at this stage technically all of them are regarded as global tracks.

With CA tracks found, there are two options for the next step. In the first one, one can convert tracks into STAR HLT's GL3 track format that was used previously. This way all of the existing GL3 functionality can be recycled, including primary vertex finding, TOF and BEMC matching, physics analysis and trigger decision making. In the second option, one can use the KFParticle to reconstruct primary vertex and obtain primary vertex, then rewrite GL3 software so that it can work with KFParticle. From the longer point of view, because that KFParticle can be used to reconstruct secondary decay vertices and can be easily parallelized, the second option is what STAR HLT should choose. However, after an initial evaluation, it is found that it takes an amount of work larger than expected to be adapt it to STAR HLT. Thus in order to not to disrupt the data taking and HTL upgrade plan for run 2013, it is decided to leave it for future development. The option one will be used for run 2013.

In Fig. 3.17 the work flow of the STAR HLT with CA tracker is shown as planned for run 2013. The basic track QA, from running the tracker in a offline mode (standing alone mode), is shown in Fig. 3.18.

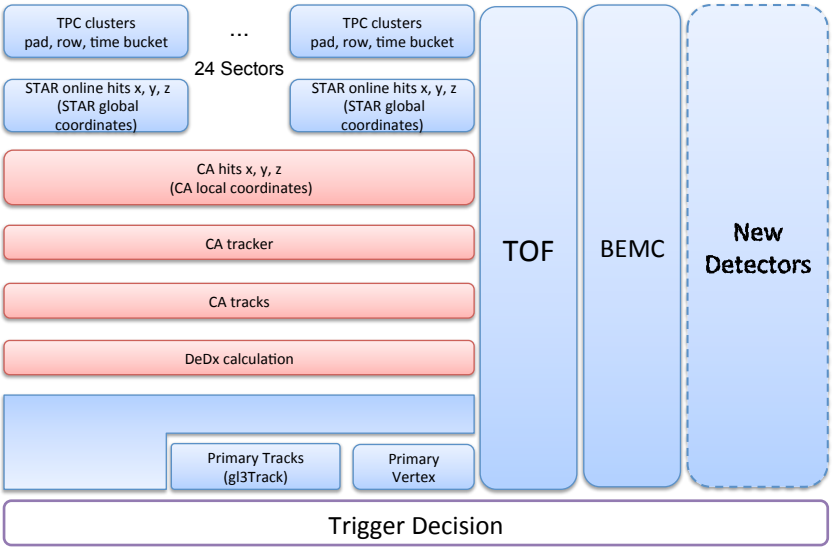


**Figure 3.17**: The upgraded work flow of the STAR High-Level Trigger with CA tracker.

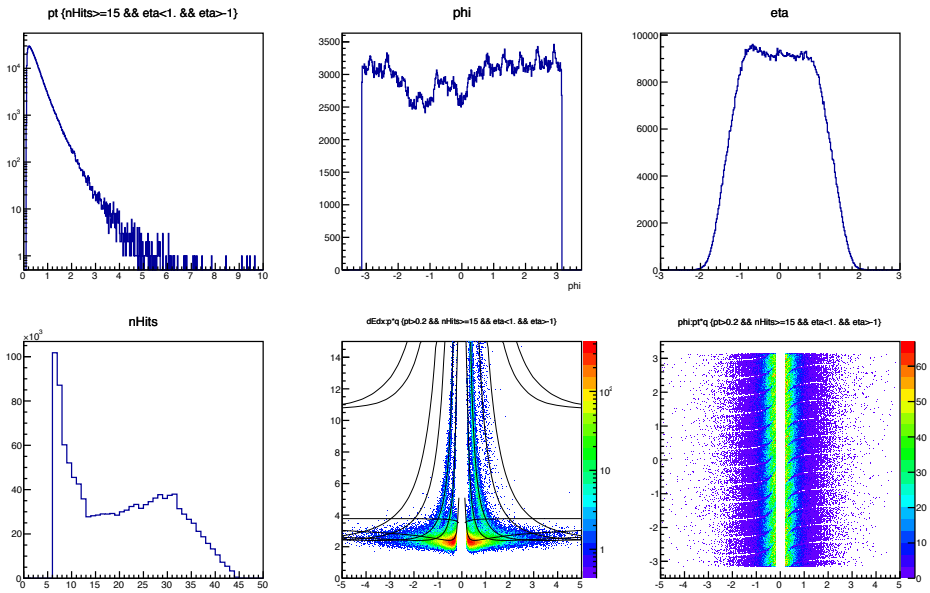


**Figure 3.18**: Basic QA plot of the STAR HLT with CA tracker.

## 3.3 High Performance Computing

The capability of processing high event rate, large data volume and perform complicated physics analysis in limited time is a key factor for the success of high energy experiments. To achieve and maintain that capability, a High-Level Trigger demands cutting edge computing technologies, from both the hardware and software, to provide adequate computing power.

In the past three to four decades, the CPU processing power had doubled every 18 months or so, following a trend that was predicted by the Moore's law [Moo06]. However, this trend will not continue forever, as transistors would eventually reach the limit of miniaturization at atomic levels. In fact, the increase of CPU processor frequency had slowed down about ten years ago and the multi-processor CPU became the main stream configuration roughly at the same time. In advanced computing, parallelism is no longer optional but mandatory, because serial applications will not benefit from the extra cores automatically. Almost every developer need to think parallel computing in order to fully utilize the capability of multi-core CPU's. Late in 2000's, a new trend, namely the heterogeneous computing, started with the general purpose graphics processing unit (GPGPU). With the evolution of semiconductor industry, more and more devices, such as GPU, digital signal processor (DSP), co-processor or field-programmable gate array (FPGA), has unignorable computing power. The idea of heterogeneous computing is to provide high performance computing by integrating computing resources from various devices. GPGPU is the most remarkable device in this wave of co-processor development by means of providing huge computing power on a single chip.

In the following section, a few technologies of parallel computing at various levels will be discussed. If implemented properly, all of them can enhance the HLT performance.

### 3.3.1 Vectorization

In parallel computing, vectorization usually means perform a single operation on multiple operands, i.e. single instruction, multiple data (SIMD). For data parallel ap-

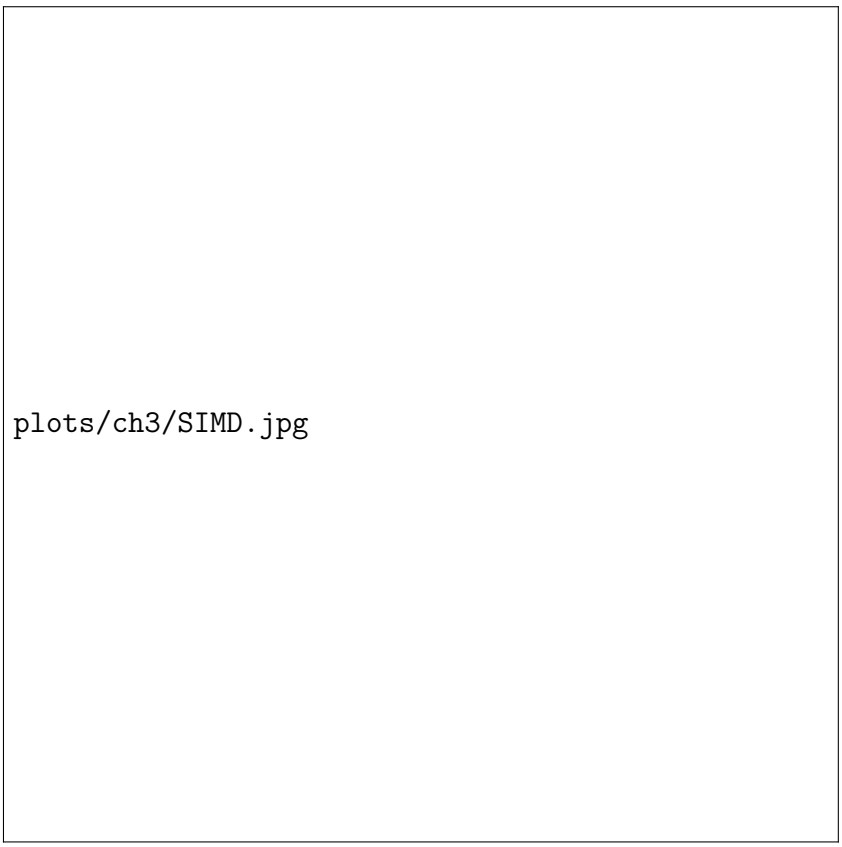


**Figure 3.19**: Scalar operation compares to SIMD operation. With a fore integer long vector, fore add operation is doing simultaneously instead of doing them one by one.

plications, SIMD can increase the system's throughput by a factor determined by the vector's length. SIMD instructions was first used in vector supercomputers in 1970s and are now available for almost all of the modern CPU's. For instance, x86 based CPUs manufactured by Intel and AMD are provided with instruction sets, like MMX, 3DNow!, SSE and AVX, to support SIMD operations. Fig. 3.19 illustrates how the SIMD operation increases the system's performance.

In high energy physics experiments, data parallelism can be found almost everywhere. However, implementing applications with SIMD instructions is not an easy task. Data needs to be organized in appropriate structures and the arithmetic needs to be expressed with SIDM instructions properly, while the interfaces are usually not user friendly.

As mentioned in Sec. 3.2.2.1 and 3.2.2.2, the CA track finder and the Kalman filter

track fitter has already been vectorized. A special C++ library, namely the Vc class, wraps the intrinsic vector types and functions by portable and user friendly API's [KL12]. According to the measurement done by GSI-Frankfurt group, vectorization gives up-to 4.5 times speedup for the CA tracker [GKK08].

### 3.3.2 Multithreading

Since early 2000's, main stream CPU's are equipped with more than one processor cores. The driven force behind the migration from single core to multi-core is the power of CPUs. For a CPU running at frequency $F$, its power can be expressed as

$$P = ACV^2F + VI_{\text{leak}}, \tag{3.27}$$

while A is a active factor representing what fraction of transistors are active, $C$ is capacitance, $V$ is the voltage and $I_{\text{leak}}$ is the current due to leakage of transistors [GHK12]. According to Eq. (3.27), the processing power increases linearly with respect to the capacitance and frequency, but quadratically with respect to the voltage. It seems that the increase of frequency will not cause the power to increase too much. However, in practice in order to increase frequency one also need to increase the voltage as well as the capacitance. Traditionally, voltage can be reduced by reducing the size of transistors. By that the frequency increases smoothly for more than two decades until in the first a few years of 2000's, the transistor's size almost reached it physical limits. When that happens, the frequency can no longer increase while keeping an affordable power level at the same time. However, one should keep in mind that the ultimate goal is not increasing the frequency but delivering more computing power on a single chip. To achieve this goal, various innovations have been developed and the simplest one is to copy a single core multiple times on a chip, which is called multi-core architecture.

Multi-thread programming is needed to fully utilize the cores for accelerating a single application. Multiple threads within a single process share process resources, such as memory address space, file descriptors, network sockets and etc., but are scheduled and executed independently by the operating system. If there are more than one cores available in a system, threads are executed on different cores concurrently. Therefore,

a task can be finished in a shorter time if compared to the case of being executed on a single core.

Tasks that can be divided into independent sub-tasks are ideal for multi-thread computing. In the TPC tracking process, reconstruction of tracks in a single sector is a well defined independent task while in total 24 of such tasks can be executed in 24 threads in parallel. Since there is no data dependency neither the communication between sector tracking tasks, a linear speedup with respect to the number of cores is expected.

The support for multithreading has been around for a long time in modern operating systems. In UNIX-like systems, one usually uses system libraries, such as PThread, to implement multi-thread applications. Low level libraries as such-like provide a powerful and flexible mechanism to manage threads, however, they also expose low level details to developers. In addition to the algorithms' logic, a lot of effort need to be devoted to the management of thread and memory. To alleviate the problem, recently Intel developed a C++ template based library named Intel Thread Building Blocks (TBB). The TBB hides the low level details and let developers to focus on the algorithms and data structure design. The CA tracker have included the functionality to use the TBB library to accelerate sub-tasks, like hit sorting and sector tracking. However, one cannot expect to have the multi-thread acceleration for free, because of the overhead paid on thread creating, management, task dispatching and etc.. One benefits from such efforts only when the acceleration gain overweigh the overhead. Usually this happens for the case of very large data volume and intensive arithmetics. This option is included in the CA tracker but its gain and overhead need to be evaluated with the hit density of STAR TPC in the future.

### 3.3.3 Heterogeneous Computing

Heterogeneous computing means to combine computing power of various devices in order to achieve unified high performance. In resent years, the most noticeable trend is the development and application of GPGPU. In 2007, NVIDIA released the Compute

Unified Device Architecture (CUDA) which allows GPU to perform general purpose computing tasks instead of processing graphic applications. Given GPU's parallel architecture, it is preferred to execute a large number of thread concurrently at a lower frequency rather than execute only a few thread at a high frequency like CPU does. This architecture provides way more raw computing power and memory bandwidth than the contemporary CPU's, as shown in Fig. 3.20.

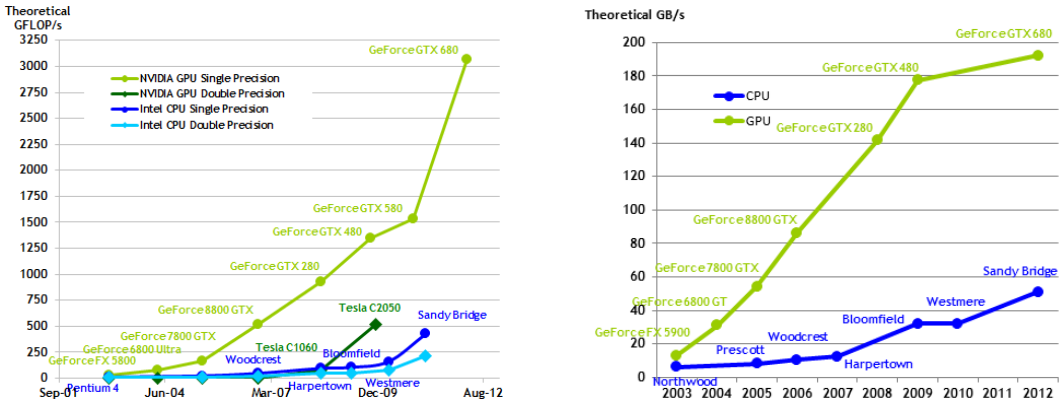


**Figure 3.20**: floating-Point Operations per Second (FLOPS) and memory bandwidth for GPU comparing to CPU.

A simplified design of GPU comparing to CPU is illustrated in Fig. 3.21. It is shown that GPU has more transistors for arithmetic and logic units (ALU), which are the data processing cores called streaming processors, but less transistors for control circuits and cache. Because of its simpler structure than CPU cores, GPU can easily contain hundreds or even thousands of streaming processors. This makes the GPU extremely computing-intensive, but it cannot deal with complicated logic as sophisticated as CPU does.

In Fig. 3.22 a typical executing model of a GPU accelerated program is shown. Since GPU provides extremely high performance on simple algorithms, massive data processing is performed by GPU threads in parallel. Serial code and parts with complicated logic, like conditional branches, are performed on CPU. This working mode takes the advantage of both CPU and GPU, and results in a high throughput system. The parallel architecture of GPU's provides the high performance, but it also brings in extra difficulties in programming. NVIDIA CUDA framework is an extension to the C/C++ programming


**Figure 3.21**: A simplified design of GPU comparing to CPU.

language. It exposes architecture details, like streaming processing arrangement, memory hierarchy, etc., to developers and make the process of implementation cumbersome. On the other hand, because streaming processors in GPU is not as sophisticated as those in CPU cores, one has to carefully chose algorithms and express them in a appropriate way so that they fit the GPU architecture in order to gain high performance.

Track reconstruction is a suitable task for GPU acceleration. Indeed the ALICE group has ported the CA tracker to CUDA. From their experience, it is found that simple porting does not work very well, but with a customized thread scheduler the GPU can be saturated around 75% [GRA11]. The application of GPU in STAR will be discussed in the next section.

Beside the CUDA platform, there are other efforts targeting the heterogeneous computing. OpenCL, stands for open computing language, is an open standard for parallel programming of heterogeneous systems. Other than specifying a certain brand of GPU, OpenCL in general can be used on any computing device, providing dramatic speedups for computationally intensive applications while maintaining a good portability. OpenCL is now available for Intel, AMD and NVIDIA chips.

Instead of making simplified processors, Intel still favors x86 architecture. In 2012, Intel released the commercial product based on their new Many Integrated Core (MIC) architecture. The MIC architecture integrates 60 x86 cores on one chip and works as a accelerator with CPU's. Although the integrated cores run at a lower frequency, with the right task configuration they can also provide huge computing power. In fact, more

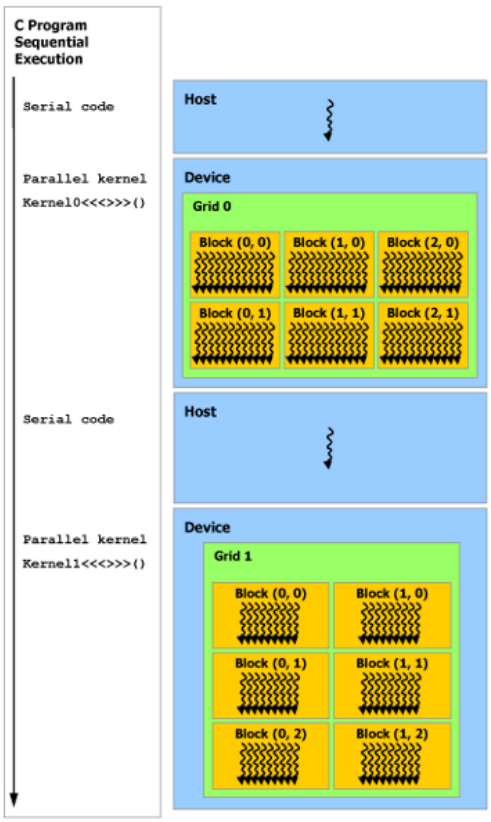


**Figure 3.22**: A typical executing model of a GPU accelerated program.

than 1 TFLOPS per card has been reported. Because MIC architecture uses the same instruction sets as that of mainstream CPU's, programming on it is claimed to be as easy as on traditional CPU's. A few groups in high energy physics community have shown interests in MIC and its applications.

### 3.3.4 A Prototype of GPU Accelerated Secondary Vertex Finder

One of the physics goals of STAR high-level trigger is to select exotics like di-V0. V0 topology consists of two charged tracks originating from a common point. In STAR, reconstructing V0 topology usually requires calculating the distance of closest approach (DCA) between two helices. Mathematically, it is a two-dimensional minimization problem that needs to be solved numerically. STAR helix model is expressed in 3D coordination space. A single search for the DCA point involves numerical iterations which can have up to tens of steps. On the other hand, the number of combinatorial candidates, i.e. track pairs, scales with the square of the multiplicity, and can easily reach the order of a million. Therefore, calculating DCA of all track pairs is the most time consuming task in physics analysis.

Fortunately, DCA calculation for a large number of track pairs is an ideal case for GPU acceleration. To start the DCA calculation one only needs the parameters of the two tracks of a pair, seven float numbers for each. The output is one float number, the DCA. Therefore, little data needs to be copied in and out of GPU. With one thread for processing one track pair, tasks are completely independent of each other and no thread communication is needed. In addition, there is sizable workload for the calculation of a track pair, which is worth to launch a thread.

The run time performance for GPU is sensitive to the algorithm used because of the limited capability of processing complicated logics. In GPU each eight streaming processors (SP) are grouped together to make a streaming multiprocessor (SM) and all the SP in a SM can only execute the same instruction at any given time. This means that, if a thread running on one SP advanced into a branch different from the thread running on another SP in the same SM, mutual waiting is unavoidable and will significantly

reduce the overall performance. Therefore, algorithms run on GPU needs to be carefully adjusted to be as *plain* as possible.

HLT uses the helix model implemented in STAR standard library to calculate DCA between two helices. In this implementation, the task is performed in two steps. Firstly, the DCA between a point and a helix is calculated by Newton iteration method. Secondly, points along the second helix are scanned in predefined steps and the minimum value is taken as the DCA. Both steps are optimized before being ported to GPU. In the first step, Newton method is stable and fast. The key to obtain extremely high performance of Newton method is to provide a initial guess as precise as possible. In the original implementation, only the $x$ and $y$ coordinates of the point are used to guess the initial position of the DCA point, and an iteration is needed to find in which phase of the helix the DCA point could possibly sit. Indeed, the $z$ coordinate of the point already indicated the phase containing the DCA point and thus can be used. With $z$ coordinate known, the calculation can be performed with the right phase of helix directly. Since this step is repeated intensively in the whole calculation, a small improvement on the performance of this step will be magnified by many times. The second step is optimized by replacing the bi-direction scan by a down-hill scan. As a result, the optimized DCA calculation code runs roughly six times faster than the original version on CPU. The differences between the DCA's calculated with and without optimization mentioned above are shown in Fig. 3.23. The two DCA calculations are in good agreement while the optimized one runs much faster.

The optimized version of DCA calculation code was then ported to CUDA, and tested on a NVIDIA GTX280 card ( which contains 240 cores consisting of 30 SM's each contains 8 SP's ). The porting to GPU gives us 10 times speedup. Together with the algorithm optimization, the final DCA calculation code running on GPU is 60 times faster than the original version running on CPU.

After porting the DCA calculation algorithm to GPU, a prototype V0 finder is built based on the DCA. In this V0 finder, CPU takes care of tasks like daughter track selection, data preparing, I/O and etc., while the DCA calculation is offloaded to GPU. In order to test the effectiveness of this GPU accelerated V0 finder, $\Lambda$ particles are

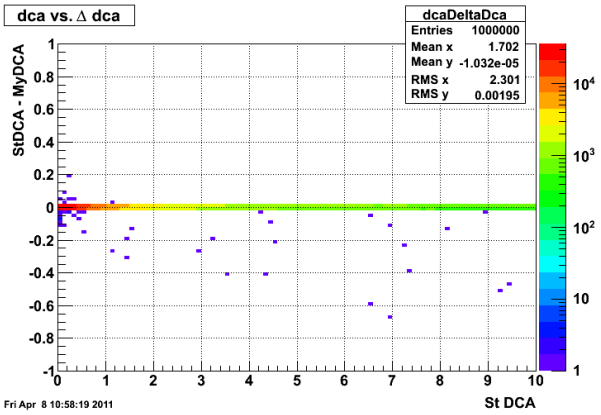


**Figure 3.23**: The different between the DCA given by the original StHelix class and that given by my optimized version.

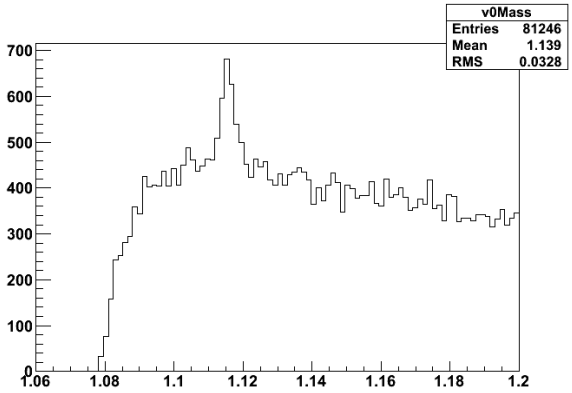


**Figure 3.24**: The invariant mass distribution of Λ meson reconstructed by GPU accelerated V0 finder from HLT tracks.

reconstructed from V0s found by the V0 finder. The invariant mass distribution of Λ candidates is shown in Fig. 3.24, in which a prominent peak of Λ can be seen.

The performance of the prototype of V0 finder has demonstrated that GPUs can be used to accelerate V0 reconstruction and gain. However, 10 times of speedup with 240 cores seems not good enough. Fine tuning in the future is needed to achieve a higher performance. GPU application in HLT will be continuously studied. Other co-processors, like Intel MIC which is advertised to have performance compatible to GPU but with a simple programming model, is also worth to investigate.

# CHAPTER 4

# Charge Asymmetry Dependency of Pion Event Anisotropy in Au + Au Collisions

In this chapter the charge asymmetry dependency of pion event anisotropy is presented and its connection to the Chiral Magnetic Wave is discussed. The azimuthal anisotropy $v_2$ of positive and negative pions at low transverse momentum, $0.15 < p_T < 0.5$ GeV, is measured in all centrality classes in Au + Au collisions at $\sqrt{s_{NN}}$ =200, 62.4, 39, 27 and 19.6 GeV. For each centrality at a given energy, the $p_T$ integrated $v_2$ is studied as a function of event-by-event charge asymmetry. It is found that $v_2$ of $\pi^-$ ($\pi^+$) linearly increases (decreases) with charge asymmetry for most centrality classes and for all of the beam energies under study. As a consequence, the difference between the $v_2$ of $\pi^-$ and $\pi^+$ increases linearly with increasing charge asymmetry.

Features mentioned above have been predicted by the theory of chiral magnetic wave (CMW), which, with finite baryon density under strong magnetic field, manifests itself in a finite electric quadrupole moment. The deformation due to this quadrupole moment will lead to a difference in azimuthal anisotropy $v_2$ between positive and negative particles. This effect can be observed via charged pions. The theoretical calculation suggests that the difference is proportional to charge asymmetry of the system. Note that the difference of integrated $v_2$ between particles and anti-particles, for various particle species, has been already observed for a wider range of energies in another study [AAA13]. However, the exact mechanisms that cause such splittings are yet to be determined. There are a number of models on the market to investigate the splitting [**?**, XCK12]. Therefore, besides checking the existence of the possible chiral magnetic wave, the study of the charge asymmetry dependency of $\pi^+/\pi^-$ azimuthal anisotropy will also shed a light

on the the $v_2$ difference between particles and anti-particles.

In following sections, we first describe the physics motivation in Sec. 4.1. Analysis technical details, including event selection and particle identification, are presented in Sec. 4.2. Methods for measuring event-by-event charge asymmetry and $v_2$ are discussed in Sec. 4.3 and 4.4. Results are reported in Sec. 4.5 followed by the discussion of systematic uncertainties in Sec. 4.6.

## 4.1 Introduction

In relativistic heavy ion collisions, incident nuclei collide with each other with significant amount of energy. Violate collisions happen at the quark and gluon level via strong interactions. The strong interaction between objects with color charge is one of the four fundamental interactions of nature, and is well described by the Quantum chromodynamics.

As a successful theory, the QCD also accommodates numerous new concepts and perspectives in understanding of our world. One of the most remarkable concepts in QCD is the *vacuum*. In contrast to its literature implication, in QCD vacuum does not mean nothing, but is fully filled with fluctuating quark and gluon field. A particular state of such quantum field with global or local minimum energy is called a vacuum. There are infinity number of QCD vacuums, however, a particular one of them, the *true* vacuum, corresponds to the absolutely lowest energy. Only the true vacuum is stable and all others are metastable states. Different QCD vacuum configuration can be characterized by the Chern-Simons topological charge, i.e. Chern-Simons number [CS74], which can be expressed as the spatial integration of gluonic field as [Dia03]

$$N_{CS} = \frac{1}{16\pi^2}\int \mathrm{d}^3\mathbf{x}\,\epsilon^{ijk}\left(A_i^a\partial_j A_k^a + \frac{1}{3}\epsilon^{abc}A_i^a A_j^b A_k^c\right). \tag{4.1}$$

The Chern-Simons number can vary by integers which corresponds to the QCD vacuum transition between different states. There are two kinds of transitions for a QCD vacuum to transit from one state to another. The first one is called *instanton*, which represents the process of quantum tuning. It allows the vacuum transit from one state to another

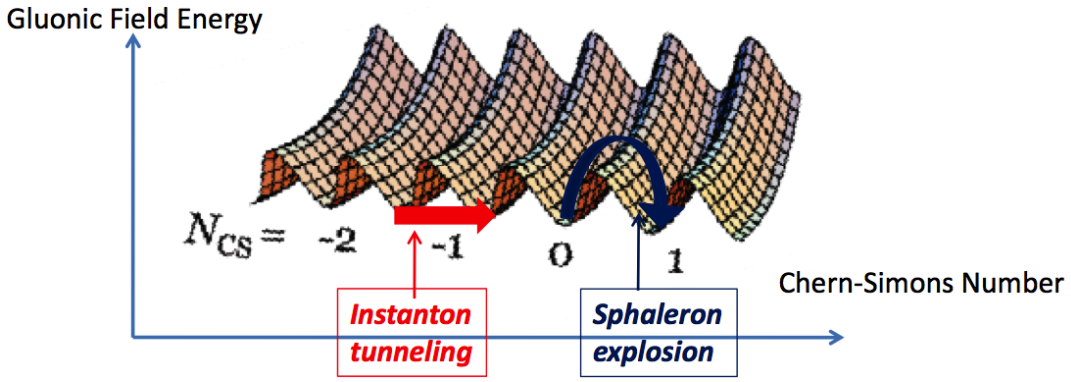


**Figure 4.1**: Gluonic field energy as a function of winding number. Originally from [Dia03].

with energy lower than the potential energy barrier. The second one is called *sphaleron*, which represents the vacuum transition by climbing over the potential energy barrier with sufficient energy. Fig. 4.1 illustrates the gluonic field energy as well as the two types of vacuum transition. What should be mentioned here is that the vacuum transition is localized in space and time. Thus, it is a *local* phenomenon.

A gauge field configuration can be characterized by a topological charge $Q_W$, the winding number. This integer is given by the integration of gluonic field tensor $F^a_{\mu\nu}$

$$Q_W = \frac{g^2}{32\pi^2}\int \mathrm{d}^4x F^a_{\mu\nu}\tilde{F}^{\mu\nu}_a. \tag{4.2}$$

$Q_W$ also represents the difference of Chern-Simons number between $t = -\infty$ and $t = +\infty$,

$$Q_W = N_{CS}(+\infty) - N_{CS}(-\infty). \tag{4.3}$$

Any field configurations with non-zero $Q_W$ lead to non-conservation of axial currents. In QCD, the axial current $j^5_\mu$, which represents the flow of net handedness, is given by

$$j^5_\mu = \sum_f \langle\bar{\psi}_f\gamma_\mu\gamma_5\psi_f\rangle_A, \tag{4.4}$$

while $\phi_f$ is quark field. The divergence of $j^5_\mu$ can then be expressed as

$$\partial^\mu j^5_\mu = 2\sum_f m_f\langle\bar{\psi}_f\gamma_\mu\gamma_5\psi_f\rangle_A - \frac{N_f g^2}{16\pi^2}F^a_{\mu\nu}\tilde{F}^{\mu\nu}_a, \tag{4.5}$$

here $m_f$ is the quark mass, $N_f$ is the number of quark flavors. Integration of Eq. (4.5) gives the net handedness, i.e. the difference of the number of left handed and right

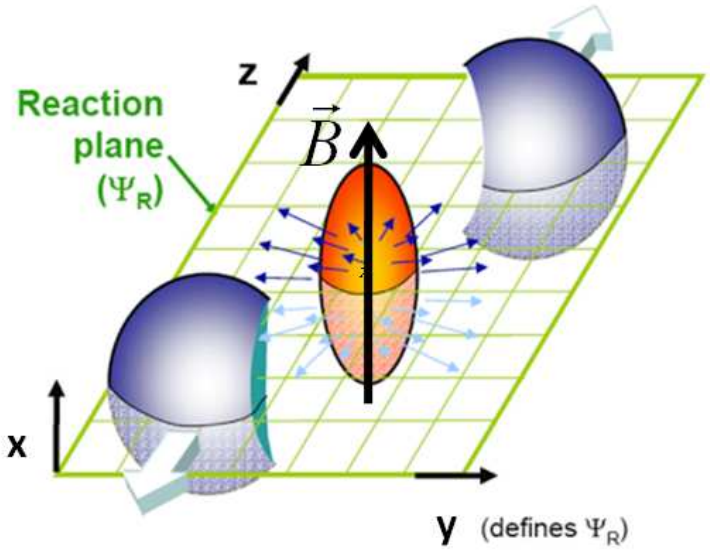


**Figure 4.2**: A middle centrality heavy ion collision with generated magnetic field perpendicular to the reaction plan.

handed quarks. Compare Eq. (4.2) and Eq. (4.5) at chiral limit, i.e. $m_f = 0$, the net handedness at $t = \infty$ is

$$(N_L - N_R)_{t=\infty} = 2N_f Q_W \tag{4.6}$$

This import equation shows that non-zero topological charge generates chiral imbalance, i.e. parity is violated in strong interactions. However, as mentioned before that vacuum transition is a local phenomenon, thus this phenomenon is called Local Parity Violation (LPV).

### 4.1.1 Chiral Magnetic Effect and Chiral Separation Effect

Chiral asymmetry described in the previous section cannot be observed directly in relativistic heavy ion collisions. However, if it exists, it can manifest itself in other mechanisms with experimentally observable consequences. Chiral Magnetic Effect (CME) is such a mechanism which comes from the interplay between the chiral asymmetry and an external strong magnetic field.

In a non-central heavy ion collision, the overlapped area of the incident nuclei, traveling in the beam line direction ( $z$ direction), has an almond shape. The collision

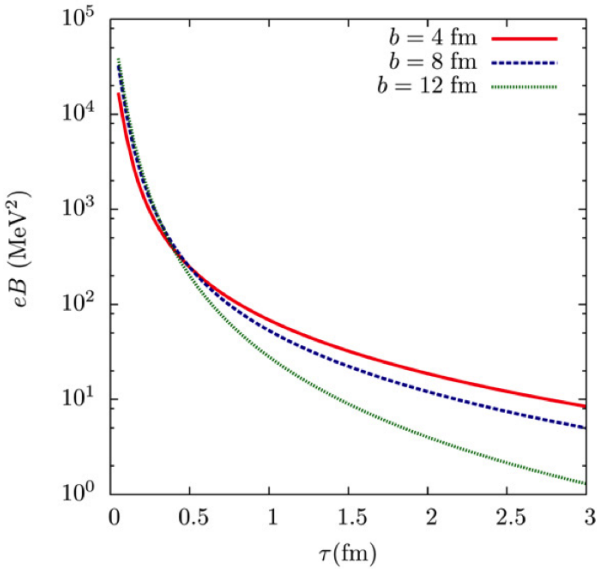


**Figure 4.3**: Magnetic field in the center of Au + Au collisions $\sqrt{s_{NN}}$ = 200 GeV. From [KMW08].

creates a fireball with significant amount of energy deposition in the almond-shape area, as shown in orange in Fig. 4.2. The rest parts of the incident nuclei are spectators, and they keep moving along their original directions. Carrying with positive charges, forward and backward moving spectators generate two electric currents moving in opposite directions, and by which a magnetic field is induced in the middle of the collision region. Because that the speed of spectators is close to the speed of light, the generated magnetic field can be extremely strong. Theoretical calculations indicate that the magnetic field generated in relativistic heavy ion collisions can be as strong as the QCD energy scale, i.e. $eB \sim \Lambda^2_{QCD}$. Numerical calculations performed for Au + Au collisions are shown in Fig. 4.2. At the early stage the produced magnetic field can reach up to $10^{15}$ T. Under a such strong magnetic field, the chiral magnetic effect begins to take place, as shown in Fig. 4.4. Consider a few left- and right-handed up and down quarks moving in a strong magnetic field $\boldsymbol{B}$. The red arrows represent the direction of quark momenta, while the blue arrows represent the direction of quark spin. Because of the $\boldsymbol{B}$ field is so large, the Landau energy level is also very large. All quarks can only stay at the lowest Landau level, i.e. moving alone or opposite to the direction of $\boldsymbol{B}$ field, shown in the cartoon for stage 1. The case for a QCD vacuum transits to a gauge field configuration with

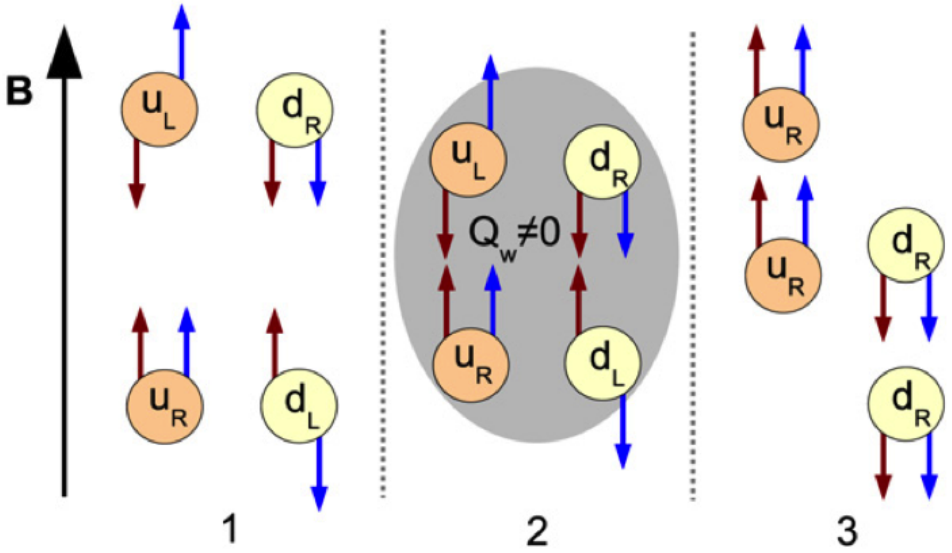


**Figure 4.4**: Chiral magnetic effect. (1) A few quarks moving along the strong magnetic field. (2) Vacuum transit to a gauge field configuration with non-zero topological charge. (3) Chirality of quarks changed via momentum reversal channel. From [KMW08].

non-zero $Q_W$, here assuming $Q_W = -1$, is shown in the cartoon for stage 2. According to Eq. (4.6), $N_L$ will decrease and $N_R$ will increase, i.e. some left-handed quarks will be converted to right-handed. At chiral limit, quark's chirality equates to its helicity. Therefore, chirality change can be done by either flipping the spin or reversing the momentum. Since the spin and $\boldsymbol{B}$ field coupling energy is proportional to the magnitude of $\boldsymbol{B}$ field, the flipping of the spin is suppressed because of the extremely strong $\boldsymbol{B}$ field. Thus left-handed quarks will reverse their momenta as the situation shown in the cartoon for stage 3. In this stage, up and down quarks move in opposite directions along the direction of magnetic field, which creates an electric current $\boldsymbol{j}_V$. This is the so called **Chiral Magnetic Effect**, and it can be expressed with the formula

$$\boldsymbol{j}_V = \frac{N_c e}{2\pi^2}\mu_A \boldsymbol{B}, \tag{4.7}$$

here, $N_c$ is the number of colors in QCD and $\mu_A$ is axial chemical potential caused by non-zero $Q_w$. At the end, for the case illustrated by the cartoon the vector current will create a charge difference of $Q = 2e$ between the two sides of reaction plane, where $e$ is the elementary charge.

For general cases the created charge difference can be summarized as, in units of $e$,

$$Q = 2Q_W \sum_f |q_f|, \tag{4.8}$$

while $q_f$ is the charge of a quark of flavor $f$. Since this process is discussed at chiral limit and with extremely strong magnetic field, Eq. (4.8) actually sets an upper limit of how much charge can be separated by the reaction plane due to the chiral magnetic effect. This charge separation has an effect on the correlation among particles that are emitted. To see the out-of-plane charge separation, the three-particle correlation function has been proposed[Vol04]. The experimental results [AAA09] and its alternative interpretations [Pra10] will be discussed later.

The chiral counter-part of Eq. (4.7) is

$$\boldsymbol{j}_A = \frac{N_c e}{2\pi^2}\mu_v \boldsymbol{B}, \tag{4.9}$$

here $\boldsymbol{j}_A$ is axial current, i.e. $\boldsymbol{j}^5_\mu$ in Eq. (4.4) and $\mu_V$ is quark chemical potential. This formula describes the **Chiral Separation Effect** (CSE), as the chiral duo version to the chiral magnetic effect. It shows that non-zero quark chemical potential triggers an axial current along the external magnetic field. This effect is originally derived in the circumstance of dense matter that is believed to exist in the core of neutron stars [SZ04, MZ05]. Since relativistic heavy ion collisions can create a matter that has density comparable to that of neutron stars, it is argued that CSE may also be found in heavy ion collisions.

### 4.1.2 Chiral Magnetic Wave

Comparing Eq. (4.7) to (4.9), one can find that these two effects are closely connected. Indeed the chiral magnetic effect and the chiral separation effect can induce each other [KSY10], forming an seamless excitation in the plasma called **Chiral Magnetic Wave** (CMW) [KY11]. Since CME and CSE gives electric charge current and chiral charge current, respectively, CMW stems from the coupling between the density waves of electric and chiral charge. Qualitatively speaking, a local fluctuation of electric charge density induces a local fluctuation of axial current, Eq. (4.9), which induces a local fluc-

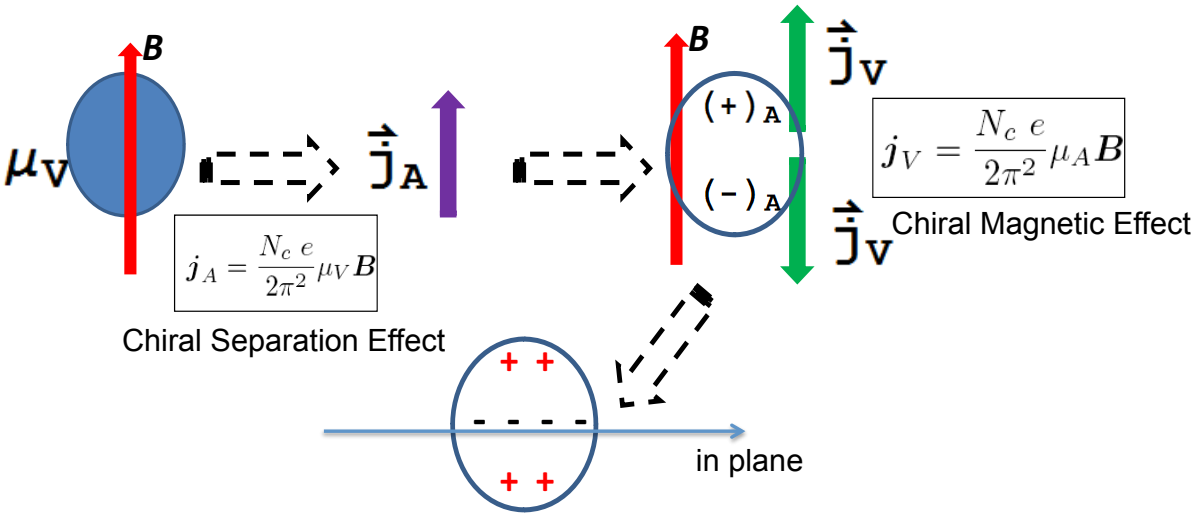


**Figure 4.5**: The evolution of a chiral magnetic wave triggered by a local fluctuation of electric charge density induces a static electric quadrupole momentum.

tuation of axial chemical potential. The local fluctuation of axial chemical potential then induces a fluctuation of electric current, Eq. (4.7), which in turn induces a fluctuation of electric charge density. These two processes make a complete cycle and form a wave of electric and chiral charge density.

The chiral magnetic wave has experimentally observable consequences. As discussed above, CSE triggered by a local fluctuation of electric charge density will induce an axial flow, which eventually makes a chiral charge dipole perpendicular to the reaction plane. The CME will then induce electric currents at the two poles. Since the two poles have net chiral charge with opposite signs, the CME induced electric current for each will flow in opposite directions [GMS11]. Finally, this process induces a static electric quadrupole momentum in the fireball. The electric quadrupole momentum acquires additional positive charge near the two poles and additional negative charge near the equator of the fireball, as illustrated in Fig. 4.5. Numerical calculation( Fig. 4.6) has confirmed the formation of electric quadrupole induced by CMW [BKL11].

The electric quadrupole momentum will be reflected in the emission angle distribution of final state charged particles. If such an electric charged configuration exists, more negative particles will be expected in the in-plane direction and more positive par-

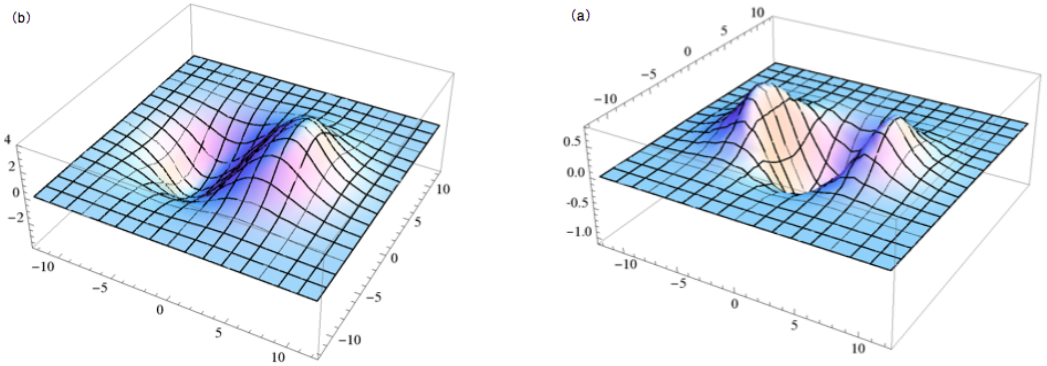


**Figure 4.6**: (a) A chiral dipole given by CMW equation in transverse plane. (b) Electric charge density in transverse plane. Background charge distribution has been subtracted. Calculated with $eB = m_\pi^2$, life time of magnetic field $\tau = 10\,\text{fm}$, $T = 165\,\text{MeV}$ and impact parameter $b = 3\,\text{fm}$. From [BKL11].

ticles will be expected in the out-of-plane direction. Therefore, azimuthal anisotropy $v_2$ of negative charged particle will be enhanced. The azimuthal distribution asymmetry between positive and negative particles can be expressed as radial integration of electric current

$$N_+(\phi) - N_-(\phi) \propto \int j_e^0(R,\phi)\, R\mathrm{d}R. \tag{4.10}$$

The 0th Fourier harmonic of this asymmetry relates to the net charge density

$$\bar{\rho}_e = \int R\mathrm{d}R\mathrm{d}\phi j_{e,B=0}^0(R,\phi). \tag{4.11}$$

The 2th harmonic relates to the CMW induced quadrupole

$$q_e = \int R\mathrm{d}R\mathrm{d}\phi \cos(2\phi)\left[j_e^0(R,\phi) - j_{e,B=0}^0(R,\phi)\right]. \tag{4.12}$$

The ratio of Eq. (4.11) and Eq. (4.12) can be used to parameter the asymmetry between the positive and negative particle azimuthal distribution

$$r = 2\frac{q_e}{\bar{\rho}_e}. \tag{4.13}$$

The charged particle azimuthal distribution can be expressed as

$$\begin{aligned}\frac{\mathrm{d}N_\pm}{\mathrm{d}\phi} &= N_\pm[1 + 2v_2\cos(2\phi)] \\ &\approx \bar{N}_\pm[1 + 2v_2\cos(2\phi) \mp A_{ch} r\cos(2\phi)],\end{aligned} \tag{4.14}$$

here $A_{ch} = (N_+ - N_-)/(N_+ + N_-)$ is the event-by-event charge asymmetry, $N_+$ and $N_-$ are the number of positive and negative particles, respectively. The charged particle $v_2$ can be expressed as a charge asymmetry dependent part on top of the *usual* elliptic flow

$$v_2^{\pm} = v_2 \mp \frac{r A_{ch}}{2}. \tag{4.15}$$

A straight forward consequence of Eq. (4.15) is that the difference between the $v_2$ of positive and negative particles is proportional to the event-by-event charge asymmetry, and the slope represents the strength of the effect of electric quadrupole momentum induced by the chiral magnetic wave. It is also argued that this effect, if exists, should be seen most likely via pions, as the measurement for other particles like protons and kaons are complicated by the more different absorption cross sections between $p$ and $\bar{p}$, and $K^+$ and $K^-$ [BKL11]. Therefore, we expect the $v_2$ of $\pi^+$ and $\pi^-$ follow the Eq. (4.16)

$$\begin{aligned} v_2(\pi^-) - v_2(\pi^+) &= r A_{ch} + C_0 \\ &= 2\left(\frac{q_e}{\bar{\rho}_e}\right) A_{ch} + C_0, \end{aligned} \tag{4.16}$$

here $C_0$ is an arbitrary constant which can be determined experimentally.

### 4.1.3 Measure Local Parity Violation at STAR

As discussed in Sec. 4.1.1, QCD vacuum transition in hot and density matter can create "$P$-violating bubbles" with asymmetry in the number of left-handed and right-handed quarks. The Chiral magnetic effect induces an electric current along the direction of the magnetic field. This out-of-plane electric charge separation manifests itself via preferential same-charge particle emission along the direction of the magnetic field, and opposite-charge particles emission oppositely along the direction of the magnetic field. A $P$-odd sine term in the Fourier series of the charge particle azimuthal distribution can be used to describe such effect.

$$\begin{aligned} \frac{\mathrm{d}N_\alpha}{\mathrm{d}\phi} \propto & 1 + 2v_{1,\alpha}\cos(\Delta\phi) + 2v_{2,\alpha}\cos(2\Delta\phi) + \cdots \\ & + 2a_{1,\alpha}\sin(\Delta\phi) + 2a_{2,\alpha}\sin(2\Delta\phi) + \cdots \end{aligned} \tag{4.17}$$

In Eq. (4.17), coefficients $a$ reflects the $P$-violating effect, $\alpha$ represents the sign of electric charge of particles, $\Delta\phi = (\phi - \Psi_{\mathrm{RP}})$ is azimuthal angle with respect to the reaction plane

and coefficients $v$ are the usual flow harmonics, i.e. $v_1$ for direct flow and $v_2$ for elliptic flow.

However, the vacuum transition happens locally in space and time independently and generates topological charge for each $P$-violating bubble randomly. Therefore, the electric charge separation direction in each bubble, which is determined by the sign of topological charge, is also random. After averaging over a large number of events, the coefficients $a$ should be zero. The observation of this effect is only possible via the correlation of coefficients, such as $\langle a_\alpha a_\beta \rangle$. $\langle\rangle$ denotes averaging over a large event sample. Direct measurement of such correlation includes two-particle correlation from different sources other than the CMW induced charge separation. To extract the $P$ violation signal, a three-particle correlator is proposed [Vol04]

$$\langle \cos(\phi_\alpha + \phi_\beta - 2\Psi_{\mathrm{RP}}) \rangle \tag{4.18}$$

$$= \langle \cos\Delta\phi_\alpha \cos\Delta\phi_\beta \rangle \langle \sin\Delta\phi_\alpha \sin\Delta\phi_\beta \rangle$$

$$= \langle [\langle v_{1,\alpha} v_{1,\beta} \rangle + B_{in}] - [\langle \alpha_{1,\alpha} \alpha_{1,\beta} \rangle + B_{out}] \rangle \,. \tag{4.19}$$

$B_{in}$ and $B_{out}$ represents the correlations in the in-plane and out-of-plane direction respectively. $\langle a_\alpha a_\beta \rangle$ is caused by the $P$ violation. Comparing to the $\langle a_\alpha a_\beta \rangle$, $\langle v_{1,\alpha} v_{1,\beta} \rangle$ is negligible, while background related to $(B_{out} - B_{in})$ is studied experimentally [AAA10a]. If there is an out-of-plane electric charge separation, Eq. (4.18) is expected to be negative for same charge correlation, i.e. $\alpha = \beta$, and positive for opposite charge correlation, i.e. $\alpha \neq \beta$.

The STAR experiment, with large and uniform acceptance, is suitable to study the azimuthal correlations. Fig. 4.7 shows the STAR measurement of the centrality dependence of three-particle correlator, Eq. (4.18), in Au + Au collisions at $\sqrt{s_{NN}}$ = 200 GeV. STAR's measurement of same- and opposite-charge is consistent with expectations based on out-of-plane electric charge separation. Models without LPV mechanism built-in cannot reproduce STAR data. Since the publication of STAR data [AAA09, AAA10a], alternative explanations have been offered in a number of publications [Pra10, BKL10, Wan10], so far this subject is not conclusive yet.

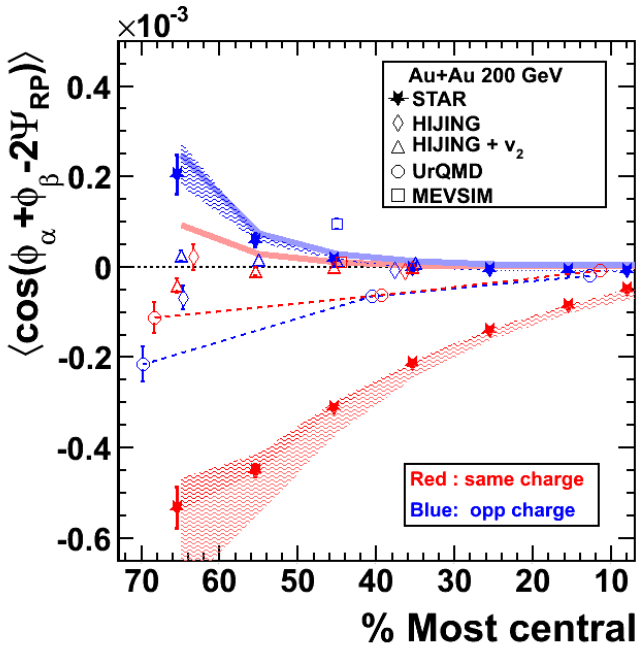


**Figure 4.7**: STAR's measurement of $\langle\cos(\phi_\alpha + \phi_\beta - 2\Psi_{\rm RP})\rangle$ in Au + Au collisions at $\sqrt{s_{NN}}$ = 200 GeV, [AAA09, AAA10a].

## 4.2 Event Selection and Particle Identification

The data used in this analysis are Au + Au minimum bias events taken by the STAR experiment at RHIC during year 2010 and 2011, including center of mass energies $\sqrt{s_{NN}}$ = 200, 62.4, 39, 27 and 19.6 GeV. The low energy runs under $\sqrt{s_{NN}}$ = 39 GeV took place as part of the RHIC Beam Energy Scan (BES) program. In this program, data of Au + Au collision at $\sqrt{s_{NN}}$ = 11.5 and 7.7 GeV are also taken but with much less statistics, thus results at these two energies will not be reported. All data used here were taken by STAR Time Projection Chamber (TPC). The TPC provides kinematic parameters of a track as well as the particle identification information based on the ionization energy loss. A Zero Degree Calorimeter (ZDC) and a Vertex Position Detector (VPD) are combined to implement the minimum bias trigger. Details of data sets used are shown in Table 4.1.

In order to investigate the centrality dependency, each data set is divided into nine bins according to the distribution of reference multiplicity, defined as the multiplicity

| $\sqrt{s_{NN}}$ | Vertex Cut | Number of Events |
|---|---|---|
| 200 GeV | $\lvert V_z\rvert < 30$ cm, $\lvert V_r\rvert < 2$ cm, $\lvert \mathrm{vpd}V_z - V_z\rvert < 3$ cm | 238 $M$ |
| 62.4 GeV | $\lvert V_z\rvert < 40$ cm, $\lvert V_r\rvert < 2$ cm, $\lvert \mathrm{vpd}V_z - V_z\rvert < 4$ cm | 62.7 $M$ |
| 39 GeV | $\lvert V_z\rvert < 40$ cm, $\lvert V_r\rvert < 2$ cm | 100 $M$ |
| 27 GeV | $\lvert V_z\rvert < 40$ cm, $\lvert V_r\rvert < 2$ cm | 40 $M$ |
| 19.6 GeV | $\lvert V_z\rvert < 40$ cm, $\lvert V_r\rvert < 2$ cm | 20 $M$ |

**Table 4.1**: Data selection criteria used in this analysis and total number of events obtained. All in Minimum bias events.

of charged particles in $|\eta| < 0.5$. Fig. 4.8 shows an example of the reference multiplicity distribution in Au + Au collisions at $\sqrt{s_{NN}}$ = 200 GeV for both real data and Monte-Carlo simulation. A weighting procedure is applied to correct the data in order to match the simulation. At very peripheral collisions, 60 - 80%, the real data is lower than the simulation due to the loss of vertex efficiency with low multiplicity in TPC. Therefore, events in this region need to be weighted by a larger factor. The effect of beam luminosity is considered in weighting. Generally speaking, at the beginning of each fill when the luminosity is relatively high, low average reference multiplicity will be recorded because of the low efficiency of detectors at high hit density and vice versa.

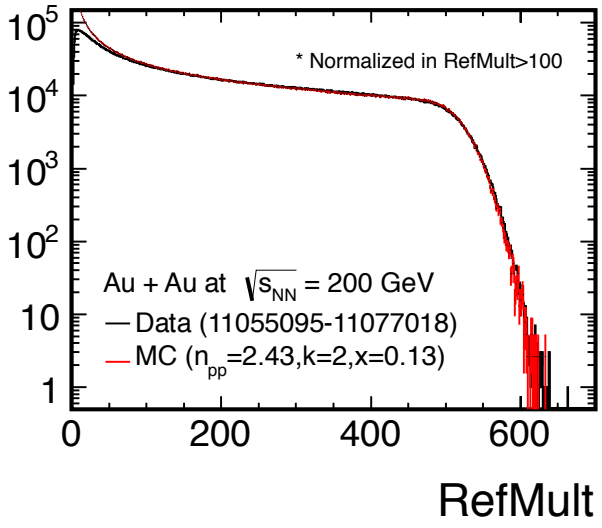


**Figure 4.8**: Reference multiplicity distribution in Au + Au collisions at $\sqrt{s_{NN}}$ = 200 GeV.

A C++ class (StRefMultCorr) has been provided in STAR as a standard class to

handle the centrality determination and generate event weight according to the centrality and luminosity at the same time. All centrality determination in this analysis are from the StRefMultCorr class.

A set of basic track quality cuts used are listed in Table 4.2. A TPC track can have up to 45 hits, a minimum of 15 TPC hits used in track fitting is required for every track participating the analysis. A single, long TPC track may be reconstructed as two shorter tracks if there exists a large gap between two hits, this phenomena is called track splitting. These two short tracks have almost identical track parameters and only one of them can be used. Requiring the ratio of number of fitting hits over the number of maximum possible hits larger than 0.52 can effectively suppress the track splitting. A minimum transverse momentum of 0.15 GeV is required, because at lower $p_T$ range tracking efficiency is too low and the track reconstruction process becomes not reliable. Since decayed particles do not contribute to the physics we are looking for, the distance of closest approach (DCA) to primary vertex of global tracks is required to be smaller than 1 cm to select primary tracks.

| Cut Parameter | Value |
|---|---|
| NHitsFit | $\geq 15$ |
| NHitsFit / NHitsPoss | $> 0.52$ |
| $p_T$ | $> 0.15$ GeV/c |
| $\|\eta\|$ | $< 1.0$ |
| global DCA | $< 1.0$ cm |

**Table 4.2**: Basic track quality cuts.

## 4.3 Event-by-event Charge Asymmetry

Because of the fluctuations in the initial stage, only a fraction of incident charge can be observed in the middle rapidity range, and the distribution has a positive mean value because the incident charge is positive. The event-by-event charge asymmetry is

defined as the ratio of net charge over the total multiplicity

$$A_{ch} = \frac{N_+ - N_-}{N_+ + N_-}. \tag{4.20}$$

All charged particles, except protons and antiprotons with very low $p_T$ , are needed to calculate the $A_{ch}$ for each event. Additional cuts for charge asymmetry measurement are listed in Table 4.3.

| Cut Parameter | Value |
|---|---|
| $p_T$ | < 12 GeV |
| $\|n\sigma_{proton}\|$ | > 3, if $p_T$ < 0.4 GeV |

**Table 4.3**: Additional cuts for charge asymmetry measurement.

Observed charge asymmetry in Au + Au $\sqrt{s_{NN}}$ = 200 GeV events for all centralities are shown in Fig. 4.9. From peripheral to central collisions, the $A_{ch}$ distribution becomes narrow. Since the interested observable is the $A_{ch}$ dependency of $v_2$ of charged pions, each centrality needs to be divided into several bins according to the $A_{ch}$ distribution. The vertical red lines in Fig. 4.9 and 4.10 divide each centrality into five subsets with roughly equal statistics. $v_2(\pi^+)$ and $v_2(\pi^-)$ are measured in each $A_{ch}$ bin.

The charge asymmetry $A_{ch}$ observed directly from data is distorted by finite tracking efficiency. To correct for it, HIJING [GW94] events are generated and a *true* $A_{ch}$ is calculated event by event based on charged particles that fall into STAR TPC acceptance and survive kinematic cuts as used in real data. The observed $A_{ch}$ can be calculated based on the same set of particles, but after being convoluted with TPC tracking efficiency (see Fig. 4.11 for its typical values). Ideally one should use the efficiency for each particle species in the convolution process. In practice since pions dominant the final state particles, tracking efficiency of charged pions was used. In Fig. 4.12 the true and observed charge asymmetry distribution of HIJING events is shown for 30 - 40% centrality. These two values has a linear relation as shown in Fig. 4.13. With the relation between true $A_{ch}$ and the observed $A_{ch}$ known, the $A_{ch}$ before efficiency loss can thus be extracted.

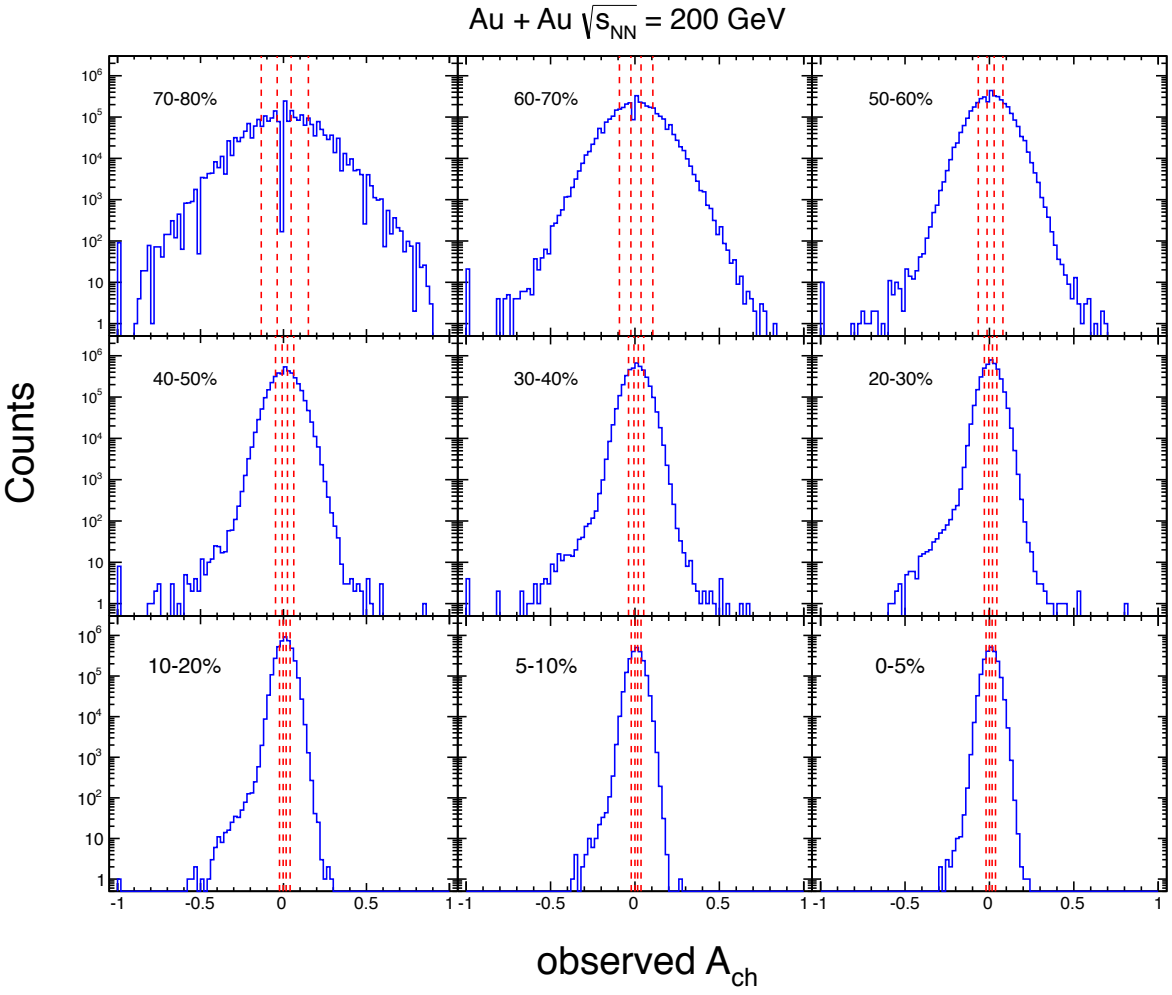


**Figure 4.9**: Observed charge asymmetry distribution in Au + Au collisions at $\sqrt{s_{NN}}$ = 200 GeV. Vertical red lines divide each centrality bin into five bins with roughly the same number of events.

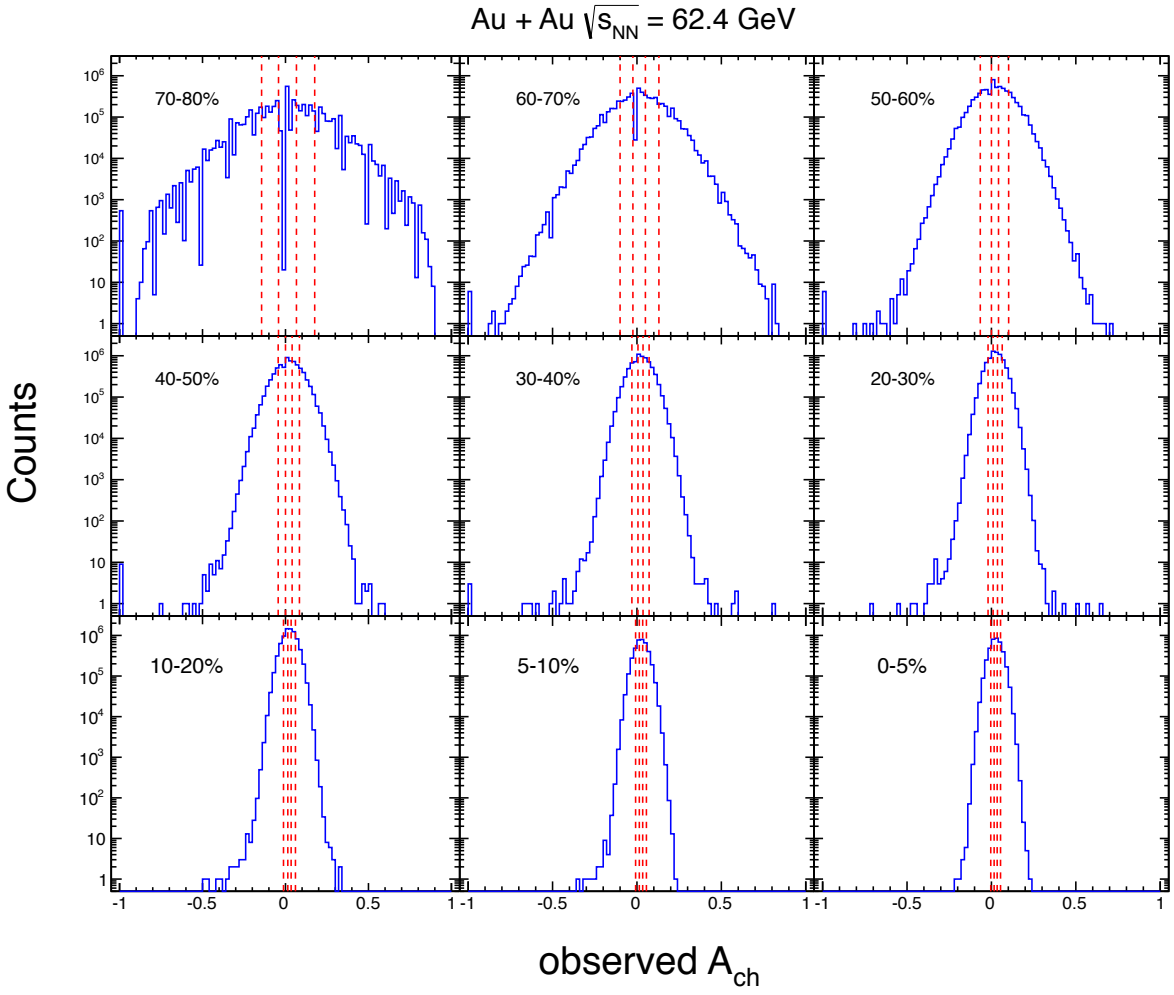


**Figure 4.10**: Observed charge asymmetry distribution in Au + Au collisions at $\sqrt{s_{NN}}$ = 62.4 GeV. Vertical red lines divide each centrality bin into five bins with roughly the same number of events.

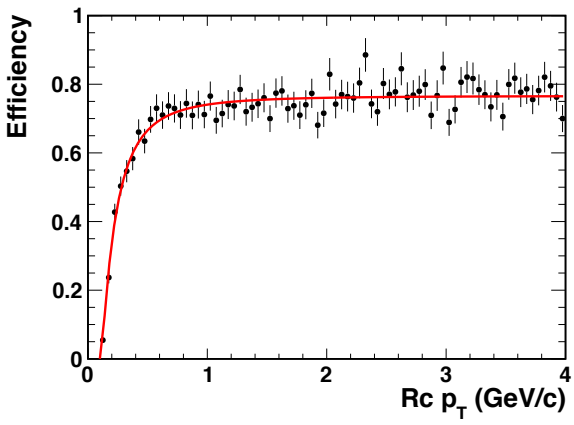


**Figure 4.11**: Tracking efficiency as a function of reconstructed transverse momentum for charged pions in Au + Au collisions, 30 - 40%, at $\sqrt{s_{NN}}$ = 200 GeV.

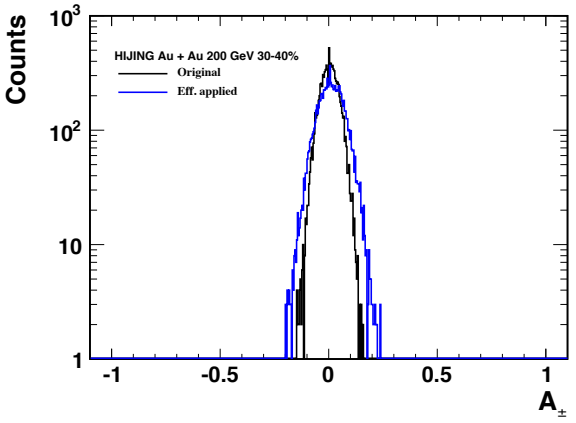


**Figure 4.12**: true and observed charge asymmetry distribution of HIJING events of 30 - 40% centrality.

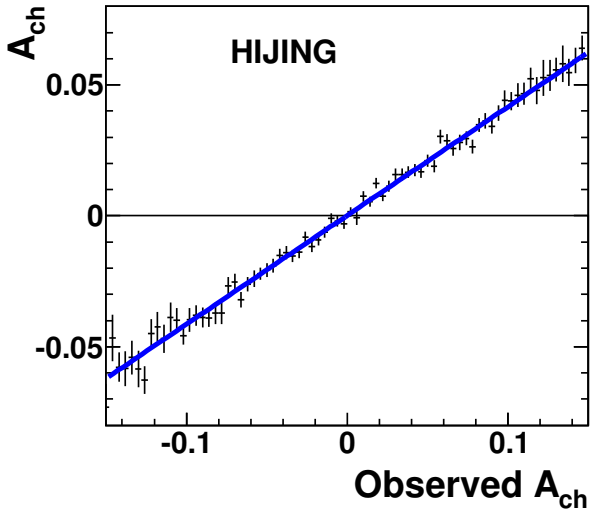


**Figure 4.13**: The relation between the true and observed charge asymmetry of HIJING events, 30 - 40% centrality.

## 4.4 $v_2$ Measurement

In heavy ion collisions, the reaction plane is determined by the line connecting the centers of the two colliding nuclei and the beam line. By convention its azimuthal angle is denoted by $\Psi_{\mathrm{RP}}$. The particle azimuthal distribution with respect to the reaction can be expanded in Fourier series [VZ96],

$$E\frac{\mathrm{d}^3N}{\mathrm{d}^3p} = \frac{1}{2\pi}\frac{\mathrm{d}^2N}{p_T\mathrm{d}p_T\mathrm{d}y}\left(1+\sum_{n=1}^{\infty}2v_n\cos\left[n(\phi-\Psi_{\mathrm{RP}})\right]\right). \tag{4.21}$$

Sine terms are vanished due to the symmetry of the system with respect to the reaction plane. Coefficients

$$v_n = \langle\cos\left[n(\phi-\Psi_{\mathrm{RP}})\right]\rangle \tag{4.22}$$

are called flow harmonics and are used to characterize the event azimuthal anisotropy, where $\langle\cdot\rangle$ denotes event average. The measured event azimuthal anisotropy is mostly converted from the asymmetry of the overlapped area of two colliding nuclei in the plane that is transverse to the beam. At RHIC the dominant term is the second harmonics, $v_2$, as it is originated from the almond shape of the overlapped area of the two colliding nuclei.

The standard method to measure the flow harmonics is the event plane method [PV98]. Since the reaction plane is not directly measurable, one can estimate it via

particle correlations. The estimated reaction plane is called event plane, and it differs from the reaction plane by a factor, namely the event plane resolution. The measurement of flow harmonics with respect to the event plane is called observed harmonics $v_n^{\rm obs}$. The true harmonics is the $v_n^{\rm obs}$ divided by the event plane resolution.

The event plane method is based on two-particle correlations, which is largely induced by flow, but include contributions from correlations that has nothing to do with the reaction plane, such as decay, jets etc. Those correlations are collectively called non-flow. To remove the non-flow contribution, cumulant method based on multi-particle correlation has been proposed [BDO01b]. The basic idea of the cumulant method is that the few particle correlation can be subtracted from the multi-particle correlation, and the residual is more close to real flow.

In this analysis, the pion event anisotropy $v_2$ was measured by two methods, the event plane method and the Q-Cumulants method.

### 4.4.1 Event Plane Method

To determine the event plane, one first calculate the flow vector

$$Qn,x = \sum_i w_i \cos(n\phi_i) = \boldsymbol{Q}_n \cos(n\Psi_n), \tag{4.23}$$

$$Qn,y = \sum_i w_i \sin(n\phi_i) = \boldsymbol{Q}_n \sin(n\Psi_n). \tag{4.24}$$

Here $\Psi_n$ is the $n^{th}$ order event plane angle, $\phi_i$ is the azimuthal angle of particle $i$, $w_i$ is a particle weight to optimize the event plane resolution. The summation runs over all of the particles in a event. The event plane can be obtained as

$$\Psi_n = \left(\tan^{-1}\frac{\sum_i w_i \sin(n\phi_i)}{\sum_i w_i \cos(n\phi_i)}\right)/n. \tag{4.25}$$

and the observed harmonics $v_n^{\rm obs}$,

$$v_n^{\rm obs} = \langle \cos[n(\phi - \Psi_n)] \rangle. \tag{4.26}$$

Final $v_n$ measurement is obtained as

$$v_n = \frac{v_n^{\rm obs}}{\mathscr{R}_n} \tag{4.27}$$

The $n^{th}$ order event plane resolution is defined as

$$\mathscr{R}_n = \langle \cos[n(\Psi_n - \Psi_{\mathrm{RP}})] \rangle \tag{4.28}$$

and can be estimated by studying the correlation between sub-events. A event can be divided into two sub-events A and B with the same number of tracks according to the tracks' charge, pseudo-rapidity or by randomly choosing. The event plane of the two sub-events, $\Psi_n^A$ and $\Psi_n^B$, can be estimated respectively. The the sub-event plane resolution is

$$\mathscr{R}_{n,\mathrm{sub}} = \langle \cos[n(\Psi_n^A - \Psi_n^B)] \rangle \tag{4.29}$$

The full event plane resolution can be thus obtained as

$$\mathscr{R}_k(\chi) = \frac{\sqrt{\pi}}{2}\chi \exp(-\chi^2/2)[I_{(k-1)/2}(\chi^2/2) + I_{(k+1)/2}(\chi^2/2)] \tag{4.30}$$

where $I$ is the modified Bessel function and $\chi = v_n\sqrt{M}$.

In an ideal case, the reaction plane azimuthal angle distribution should be flat as nuclei collide at random angles. However, in practice the event plane distribution is usually not flat because of the imperfect detector acceptance and efficiency. A few methods have been developed to compensate the uneven distribution of event plane angle. The phi weight method uses the inverse azimuthal angle distribution of particles as weight for each particle participated in the event plane reconstruction. However, if the acceptance at a certain $\phi$ angle range is completely gone, the phi method will not be reliable because the weight goes to infinity. In this case, another method called re-center method can be used. The flow vector showing in Eq. (4.24) and (4.24) should have zero mean values over a large event sample for the case of an ideal detector. The non-zero means reflect the inefficiency of the detector. Subtracting $\langle Q_n \rangle$ from $Q_n$ of each event, $Q_n - \langle Q_n \rangle$ will be forced to center at zero. Event plane calculated from the re-centered flow vector $Q_n - \langle Q_n \rangle$ will thus has a flat distribution. If the event plane distribution is still not flat after phi weight or re-center correction due to serious acceptance loss, a shifting method can be applied to make it flat [BBB97].

As what mentioned before, measurements obtained with the event plan method may be influenced by non-flow effects. Short range correlations, such as HBT correlation and

jet correlation, are among the sources of nonflow. A pseudo-rapidity gap, $\eta$-gap, between the particles for event plane reconstruction and the particle of which $v_n$ will be measured, a.k.a particle of interests (POI), can be used to suppress these effect. In this analysis, in order to measured the $v_n$ of the particle of $0 < \eta < 1$, particles from $-1 < \eta < -0.3$ are used to reconstruct event plane. This procedure has been applied to the analysis of $v_2$ of charged pion at $\sqrt{s_{NN}}$ equals to and lower than 39 GeV.

### 4.4.2 Q-Cumulant Method

The cumulant method measures the flow harmonics from two- or multi-particle correlations [BDO01c, BDO01b, BDO01a]. The advantage of the cumulant method is the correlations between fewer particles, i.e. lower order cumulant, can be subtracted from higher order cumulant. Studies showed that at RHIC $v_n$ measurements from four and more particles cumulant are believed to be almost free of non-flow effects [AAA05a].

The cumulant method starts with the flow vector of a single particle, $[\cos(n\phi), \sin(n\phi)]$, which can be written as

$$u_n = e^{in\phi}. \tag{4.31}$$

Two-particle correlation can be written as flow plus a non-flow term

$$\left\langle u_{n,1} u^*_{n,2} \right\rangle = \left\langle e^{in(\phi_1 - \phi_2)} \right\rangle = v_n^2 + \delta_n. \tag{4.32}$$

Here $v_n^2$ is flow contribution to two-particle correlation, $\delta_n$ represents non-flow contribution, $u^*_{n,2}$ is the complex conjugate of $u_{u,2}$ and $\langle \cdot \rangle$ denotes averaging over all particles pairs in a event and all events in a sample. The two-particle cumulant equals to the two-particle correlation

$$c_n\{2\} = \left\langle u_{n,1} u^*_{n,2} \right\rangle. \tag{4.33}$$

In case of four-particle correlation

$$\left\langle u_{n,1} u_{n,2} u^*_{n,3} u^*_{n,4} \right\rangle = \left\langle e^{in(\phi_1 + \phi_2 - \phi_3 - \phi_4)} \right\rangle = v_n^4 + 2 \cdot 2 \cdot v_n^2 \delta_n + 2\delta_n, \tag{4.34}$$

while the four-particle cumulant is

$$c_n\{4\} = \left\langle e^{in(\phi_1 + \phi_2 - \phi_3 - \phi_4)} \right\rangle - 2 \left\langle e^{in(\phi_1 - \phi_3)} \right\rangle^2 = -v_n^4. \tag{4.35}$$

The Fourier harmonics $v_n$ can be estimated via two- and four-particle cumulant.

$$v_n\{2\} = \sqrt{c_n\{2\}} \tag{4.36}$$

$$v_n\{4\} = \sqrt[4]{-c_n\{4\}} \tag{4.37}$$

According to Eq. (4.32), the $v_n\{2\}$ estimation given by Eq. (4.36) also includes non-flow, just like the event plane method. Because that the dominant non-flow is at two particle correlation level, and two-particle correlations have been subtracted from four-particle correlations as showed in Eq. (4.35), $v_n\{4\}$ given by Eq. (4.35) is almost free of non-flow effect. $v_n\{2\}$ and $v_n\{4\}$ are two independent estimations of the same Fourier harmonics, with the latter being less affected by non-flow but requires more statistics to achieve the same significance as that of the former.

Calculating cumulant is computing intensive, as one has to exhaust all quadruplets. In high energy heavy ion collisions, a typical event contains roughly a thousand of final state particles. Direct calculation of four particle cumulant is very difficult, if not impossible at all. A generating function method was proposed to calculate cumulant with linear complexity, i.e. number of required operations linearly related to the multiplicity $M$. However, this method involves tedious analytically calculations and one needs to perform the analysis twice to obtain the differential flow, with the first pass merely to obtain the integrated flow.

The Q-Cumulant is a newly developed method to calculate cumulant [BSV11, Bil12]. It is more straightforward if compared to the method based on generating function. The additional advantage of the Q-Cumulant method is that it provides fast (one loop over data) and exact non-biased (no approximations and no interference between different harmonics) estimation of correlators. The cumulant are expressed in terms of the moments of the magnitude of the corresponding flow vector $Q_n$ which can be easily calculated,

$$Q_n \equiv \sum_{i=1}^{M} e^{in\phi_i} \tag{4.38}$$

From now on, we will use $\langle \cdot \rangle$ to denote single-event average over all particles and use $\langle\langle \cdot \rangle\rangle$ to denote event-level average over all events in a sample. The single-event average

of two- and four-particle azimuthal correlations can be then formulated as

$$\langle 2 \rangle = \frac{|Q_n|^2 - M}{M(M-1)}, \tag{4.39}$$

$$\langle 4 \rangle = \frac{|Q_n|^4 + |Q_{2n}|^2 - 2 \cdot \Re\left[Q_{2n} Q_n^* Q_n^*\right]}{M(M-1)(M-2)(M-3)} - 2\frac{2(M-2) \cdot |Q_n|^2 - M(M-3)}{M(M-1)(M-2)(M-3)}, \tag{4.40}$$

while $M$ is the multiplicity in use. Averaging over all events and can be performed as

$$\langle\langle 2 \rangle\rangle \equiv \langle\langle e^{in(\phi_1 - \phi_2)} \rangle\rangle \equiv \frac{\sum_{events} \left(W_{\langle 2 \rangle}\right)_i \langle 2 \rangle_i}{\sum_{events} \left(W_{\langle 2 \rangle}\right)_i}, \tag{4.41}$$

$$\langle\langle 4 \rangle\rangle \equiv \langle\langle e^{in(\phi_1 + \phi_2 - \phi_3 - \phi_4)} \rangle\rangle \equiv \frac{\sum_{events} \left(W_{\langle 4 \rangle}\right)_i \langle 4 \rangle_i}{\sum_{events} \left(W_{\langle 4 \rangle}\right)_i}, \tag{4.42}$$

here the weights are the number of two- and four-particle combinations

$$W_{\langle 2 \rangle} \equiv M(M-1), \tag{4.43}$$

$$W_{\langle 4 \rangle} \equiv M(M-1)(M-2)(M-3). \tag{4.44}$$

Including these multiplicity as weights can make the final multi-particle azimuthal correlations free of multiplicity fluctuations [Bil12]. However, one can also use unit weight and treat events with different multiplicity equally. The $v_n$ estimations can then be obtained according to Eq. (4.33, 4.35) and Eq. (4.36, 4.37).

The process described above can be performed over a large number of low transverse momentum particles, namely reference particles (REP), in order to obtain the reference flow. Reference flow, as suggested by its name, serves as a reference in the calculation. To have a good reference, the multiplicity $M$ of the reference particle pool should be as large as possible.

In order to measure differential flow of particle of interest (POI), two more vectors $p$ and $q$ need to be constructed. For particles labeled as POI

$$p_n \equiv \sum_{i=1}^{m_p} e^{in\psi_i}. \tag{4.45}$$

For particles labeled as both POI and REP

$$q_n \equiv \sum_{i=1}^{q_p} e^{in\psi_i}. \tag{4.46}$$

Then the reduced single-event average two- and four-particle correlations are

$$\langle 2' \rangle = \frac{p_n Q_n^* - m_q}{m_p M - m_q} \tag{4.47}$$

$$\begin{aligned} \langle 4' \rangle = & [p_n Q_n Q_n^* Q_n^* - q_{2n} Q_n^* Q_n^* - p_n Q_n Q_{2n}^* \\ & - 2 \cdot M p_n Q_n^* - 2 \cdot m_q |Q_n|^2 + 7 \cdot q_n Q_n^* \\ & - Q_n q_n^* + q_{2n} Q_{2n}^* + 2 \cdot p_n Q_n^* + 2 \cdot m_q M \\ & - 6 \cdot m_q] / [(m_p M - 3 m_q)(M-1)(M-2)] \end{aligned} \tag{4.48}$$

and the event average can be obtained as

$$\langle\langle 2' \rangle\rangle = \frac{\sum_{i=1}^{N} (w_{\langle 2' \rangle})_i \langle 2' \rangle_i}{\sum_{i=1}^{N} (w_{\langle 2' \rangle})_i} \tag{4.49}$$

$$\langle\langle 4' \rangle\rangle = \frac{\sum_{i=1}^{N} (w_{\langle 4' \rangle})_i \langle 4' \rangle_i}{\sum_{i=1}^{N} (w_{\langle 4' \rangle})_i} \tag{4.50}$$

Where multiplicity weights are

$$w_{\langle 2' \rangle} \equiv m_p M - m_q \tag{4.51}$$

$$w_{\langle 4' \rangle} \equiv (m_p M - m_q)(M-1)(M-2) \tag{4.52}$$

The two- and four-particle differential cumulant without detector bias are given by

$$d_n\{2\} = \langle\langle 2' \rangle\rangle \tag{4.53}$$

$$d_n\{4\} = \langle\langle 4' \rangle\rangle - 2 \cdot \langle\langle 2' \rangle\rangle \langle\langle 2 \rangle\rangle \tag{4.54}$$

Estimations of differential flow are expressed as

$$v_n'\{2\} = \frac{d_n\{2\}}{\sqrt{c_n\{2\}}} \tag{4.55}$$

$$v_n'\{4\} = \frac{d_n\{4\}}{-c_n\{2\}^{3/4}} \tag{4.56}$$

The statistical errors of $v_n$ estimations given by Q-Cumulant method can be obtained by error permeation formulas. Note that the different cumulant and the detector

correlations terms discussed below are not independent variables. When calculating statistical errors, at lease the most significant off-diagonal elements of the covariance matrix must be taken into account. Otherwise, the statistical errors will be overestimated.

The formulas of Q-Cumulant method discussed above are derived for the case of an idea detector. In practice one has to take into account the uneven efficiency loss in the azimuth. Such detector inefficiency can also be estimated via a comprehensive correction procedure, taking various multi-particle correlations as inputs. Details of the statistical error estimation and detector inefficiency correction can be found in Ref. [BSV11, Bil12].

The Q-Cumulant has been independently implemented to measure $v_2$ via two- and four-particle correction, and the flow measured with it has been demonstrated to be correct and reliable. Besides this analysis, it was also used to measure charged particle $v_2\{2\}$ and $v_2\{4\}$ from $\sqrt{s_{NN}}$ = 39 - 7.7 GeV. As an example, in Fig. 4.14, $v_2\{2\}$ and $v_2\{4\}$, measured by generating function method and Q-Cumulant, is shown as a function of $p_T$ for Au + Au collisions at $\sqrt{s_{NN}}$ = 39 GeV. The two methods give consistent results in all centralities while both of them failed to measure $v_2\{4\}$ in the most central (0-5%) collisions.

In the study of the charge asymmetry dependency of pion event azimuthal anisotropy, Q-Cumulant method is used to measure $v_2$ of $\pi^+$ and $\pi^-$ via two-particle correction in Au + Au collisions at $\sqrt{s_{NN}}$ = 200 and 62.4 GeV. Four-particle cumulant is not chosen because it is way more statistics hungry than the two-particle cumulant. In order to suppress the non-flow from short range correlations, an event is divided into two sub-events according to the pseudo-rapidity of particles, and a $\eta$-gap of 0.3 is applied, to the REF side, between reference and particle of interest. Here the particle of interest are $\pi^+$ or $\pi^-$. This is the same technique used in the event plane method. In addition to basic cuts for selecting particles as listed in Table. 4.2, additional cuts for selecting charged pions are listed in Table.4.4 and cuts for selecting REP and POI, as the two sub-events, are listed in Table.4.5.

In order to take into account the particular selection criteria for this analysis, the two-particle correlation Eq. (4.39) and reduced two-particle correlation Eq. (4.47) need

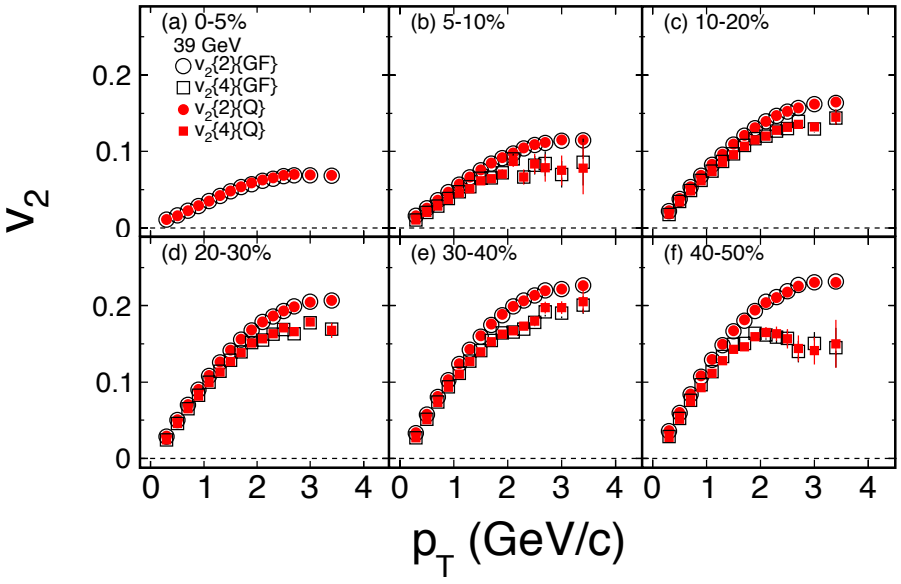


**Figure 4.14**: Charged particle $v_2\{2\}$ and $v_2\{4\}$ as a function of $p_T$ in Au + Au collisions at $\sqrt{s_{NN}}$ = 39 GeV measured by generated function method and Q-Cumulant method. Both of these two method are failed to measure $v_2\{4\}$ in the most central (0-5%) collisions.

| Cut Parameter | Values |
|---|---|
| $\lvert n\sigma_\pi \rvert$ | $< 2.0$ |
| ndEdx | $\geq 10$ |
| $p_T$ | $< 0.5$ GeV |

**Table 4.4**: Particle identification cuts for charge pions ($\pi^\pm$) in addition to the basic track quality cuts listed in Table. 4.2. $n\sigma_\pi$ is normalized ionization energy loss in TPC defined in Sec.2.2.1. ndEdx is the number of hit used when fitting the ionization energy loss $\mathrm{d}E/\mathrm{d}x$. Require the transverse momentum, $0.15 < p_T < 0.5$ GeV, can assure the purity of selected poins.

| sub-event | REP | POI |
|---|---|---|
| A | $p_T < 2.0$ GeV | $\pi^\pm$ |
| | $-1 < \eta < -0.3$ | $0 < \eta < 1$ |
| B | $p_T < 2.0$ GeV | $\pi^\pm$ |
| | $0.3 < \eta < 1$ | $-1 < \eta < 0$ |

**Table 4.5**: Particle selection cuts of reference particle and particle of interest in two sub-events in addition to the basic track quality cuts listed in Table. 4.2.

to be modified accordingly.

The two-particle correlation from two sub-events is

$$\langle 2 \rangle = \frac{Q_n^A \cdot Q_n^{B*}}{M_A M_B}, \tag{4.57}$$

here $Q_n^A$ and $Q_n^B$ are flow vectors calculated from reference particles for sub-event A and B. $M_A$ and $M_B$ are multiplicities of these two sub-events.

The reduced two-particle correlation are

$$\langle 2' \rangle^A = \frac{p_n^A \cdot Q_n^{B*}}{m_p^A M_B} \tag{4.58}$$

$$\langle 2' \rangle^B = \frac{p_n^B \cdot Q_n^{A*}}{m_p^B M_A} \tag{4.59}$$

The final $v_2$ measurements can still be obtained as Eq. (4.55). The two sub-events, Eq. (4.58) and (4.58), cover the effective pseudo-rapidity range of STAR TPC, $|\eta| < 1$. This method is used to analyze data at $\sqrt{s_{NN}} = 200$ and 62.4 GeV.

## 4.5 Results

In this section, the $v_2$ measurements of $\pi^+$ and $\pi^-$ integrated over $0.15 < p_T < 0.5$ GeV will be presented for different charge asymmetry bins, centralities and energies. The difference in $v_2$ between $\pi^+$ and $\pi^-$, i.e. $\Delta v_2 = v_2(\pi^-) - v_2(\pi^+)$, will be presented as a function of corrected charge asymmetry. The slope parameter Eq. (4.13) of $\Delta v_2(A_{ch})$will be extracted for all centralities and energies as discussed in Sec. 4.1.2. The centrality and energy dependency of the slope parameter will be compared to theoretical and model calculations.

### 4.5.1 Charge Asymmetry dependency of $v_2(\pi^-)$ and $v_2(\pi^+)$

The charge asymmetry dependency of $v_2(\pi^-)$ and $v_2(\pi^+)$, integrated from $p_T$ range 0.15 – 0.5 GeV, is presented in Fig. 4.15 and 4.16, for Au + Au collisions at at $\sqrt{s_{NN}} =$ 200 and 62.4 GeV, respectively. The abscissa in the two figures are the mean value of $A_{ch}$ in each charge asymmetry bin determined by the distribution shown in Fig. 4.9 and 4.10.

$v_2(\pi^-)$ and $v_2(\pi^+)$ are measured by Q-Cumulant method via two-particle correction with a $\eta$-gap, as is described in Sec. 4.4.2.

In middle centralities, 20-50% for $\sqrt{s_{NN}}$ = 200 GeV and 20-40% for $\sqrt{s_{NN}}$ = 62.4 GeV, $v_2(\pi^-)$ is larger than $v_2(\pi^+)$ in general, and $v_2(\pi^-)$ and $v_2(\pi^+)$ have opposite trend as a function of charge asymmetry $A_{ch}$. $v_2(\pi^-)$ linearly increases with increasing $A_{ch}$ while $v_2(\pi^+)$, linearly decreases. The absolute value of the slope parameter of $v_2(\pi^-)$ and $v_2(\pi^+)$ as a function of $A_{ch}$ is roughly the same. All of the features are consistent with the expectations described by Eq. (4.15) based on chiral magnetic wave.

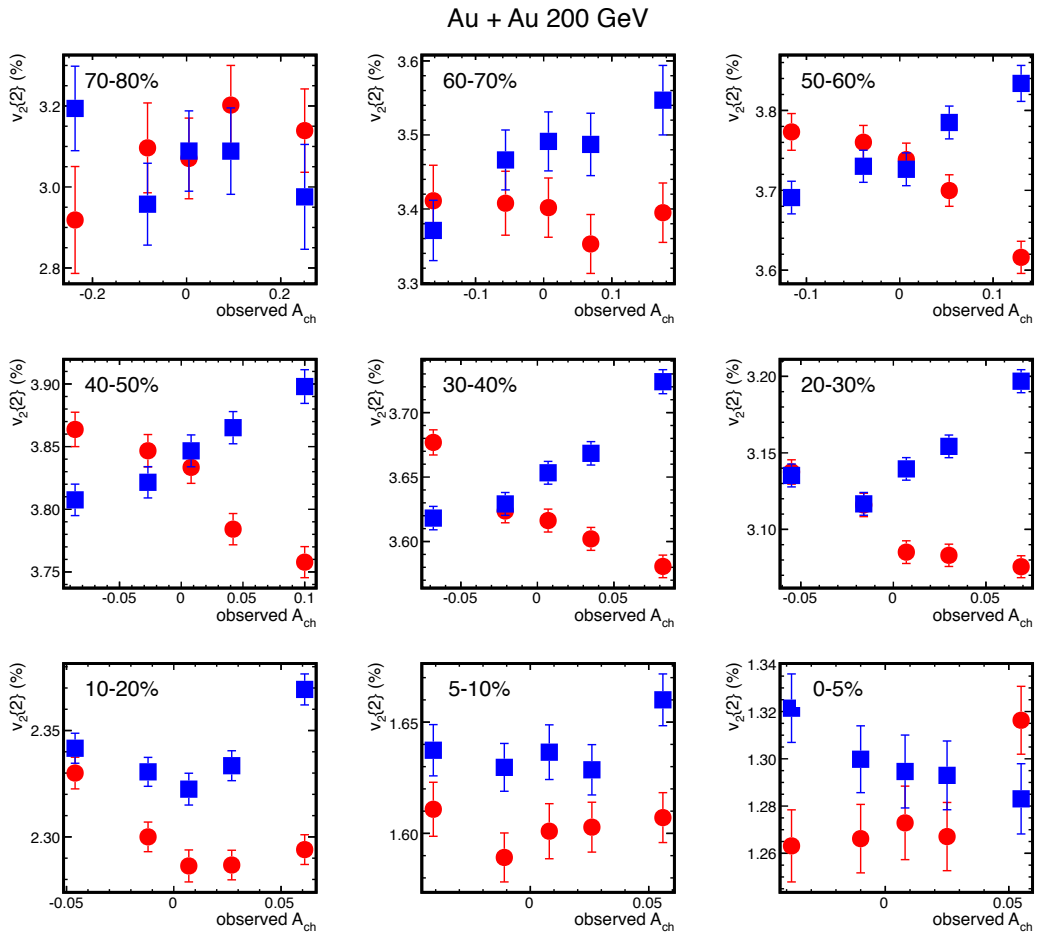


**Figure 4.15**: Integrated $v_2$ of $\pi^+$ and $\pi^-$ measured by Q-Cumulant method, $0.15 < p_T < 0.5$ GeV, as a function of observed charge asymmetry in Au + Au collisions at $\sqrt{s_{NN}}$ = 200 GeV.

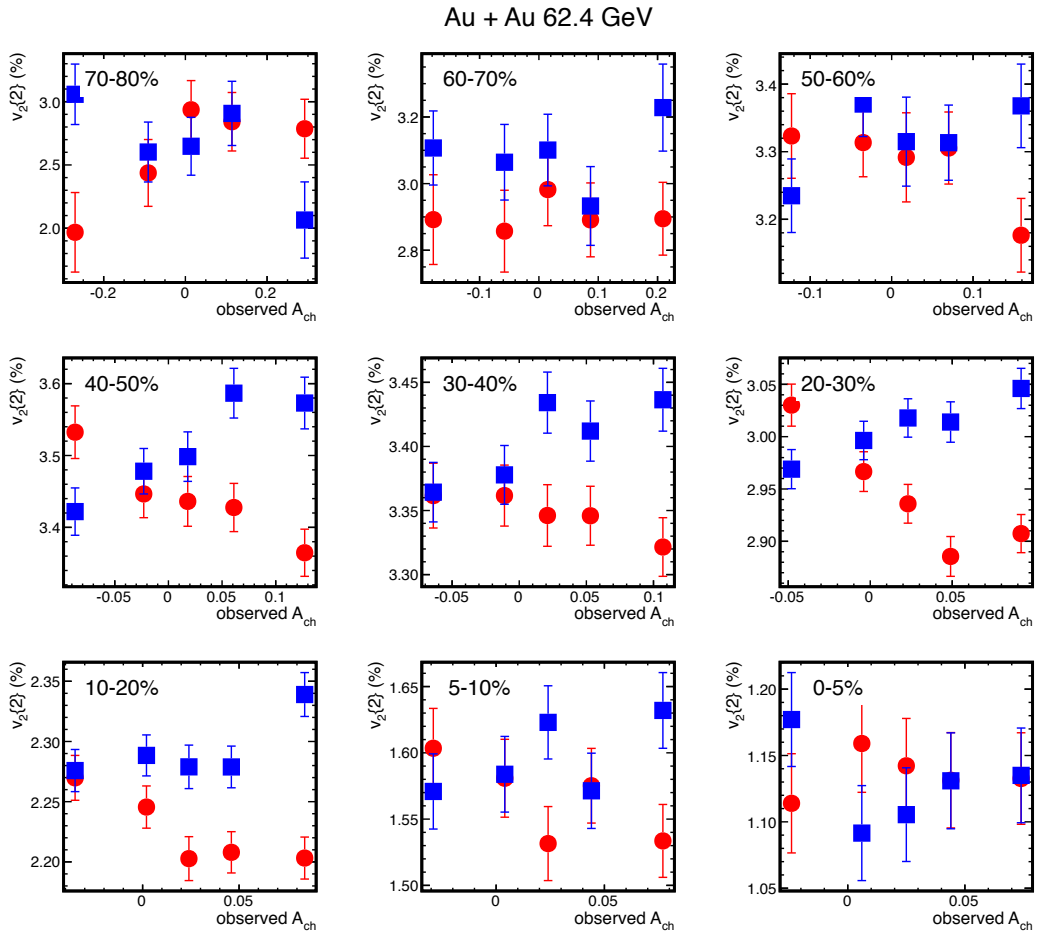


**Figure 4.16**: Integrated $v_2$ of $\pi^+$ and $\pi^-$ measured by Q-Cumulant method, $0.15 < p_T < 0.5$ GeV, as a function of observed charge asymmetry in Au + Au collisions at $\sqrt{s_{NN}}$ = 62.4 GeV.

### 4.5.2 Centrality and Energy Dependency of Slope Parameter

The difference between $v_2(\pi^-)$ and $v_2(\pi^+)$, $\Delta v_2$, increases linearly with increasing $A_{ch}$. The slope $r$ of such linear relationship, defined by Eq. (4.13), reflects the electric quadrupole momentum induced by the chiral magnetic wave. In Fig. 4.17 and 4.18, $\Delta v_2 = v_2(\pi^-) - v_2(\pi^+)$ is presented as a function of corrected charge asymmetry. The procedure of making correction to charge asymmetry is described in Fig. 4.13. Fitting the $\Delta v_2(A_{ch})$ with straight lines, the slope parameters can be extracted in each centrality and energies. The same analysis is performed at $\sqrt{s_{NN}}$ = 39, 27 and 19.6 GeV by Gang Wang using event plane method with a $\eta$-gap.

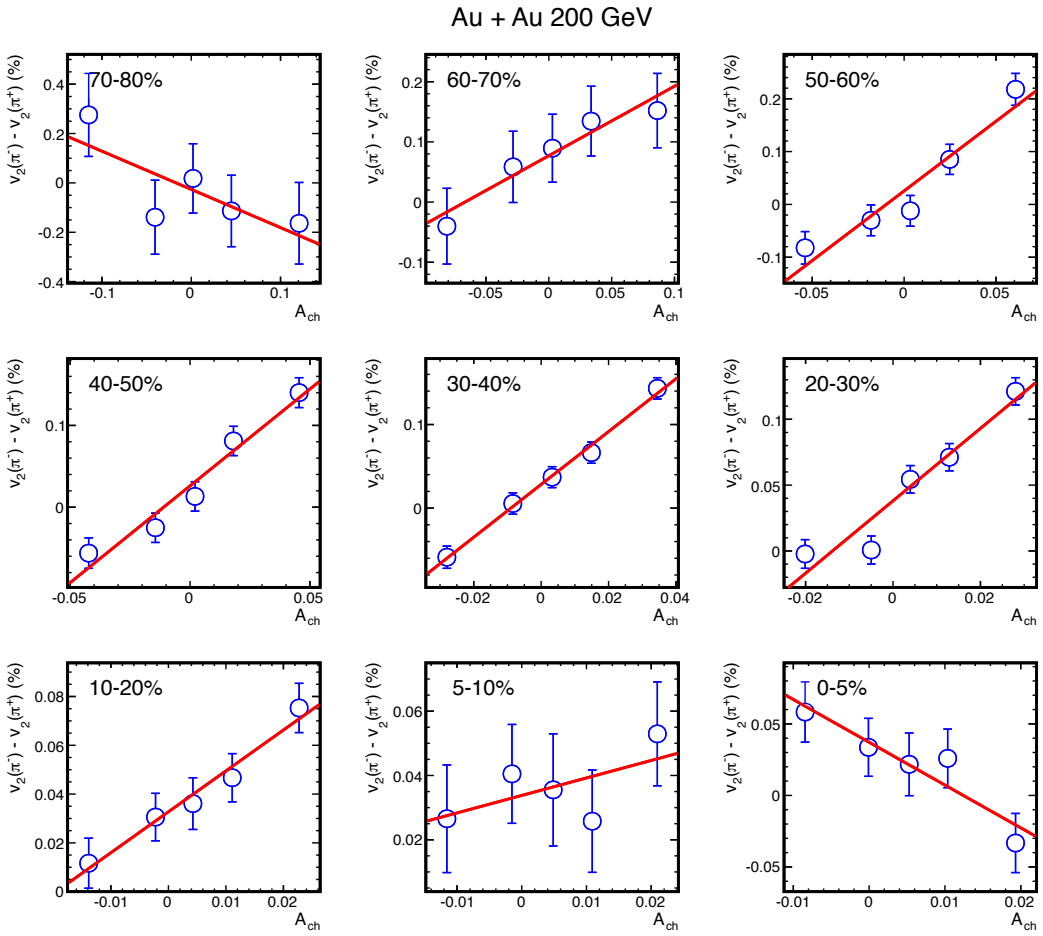


**Figure 4.17**: Integrated $v_2$ difference between $v_2(\pi^-)$ and $v_2(\pi^+)$ as function of charge asymmetry in Au + Au collisions at $\sqrt{s_{NN}}$ = 200 GeV. The solid red lines represent the straight line fit, the slope parameter of which is the observable $r = 2q_e/\bar{\rho}_e$.

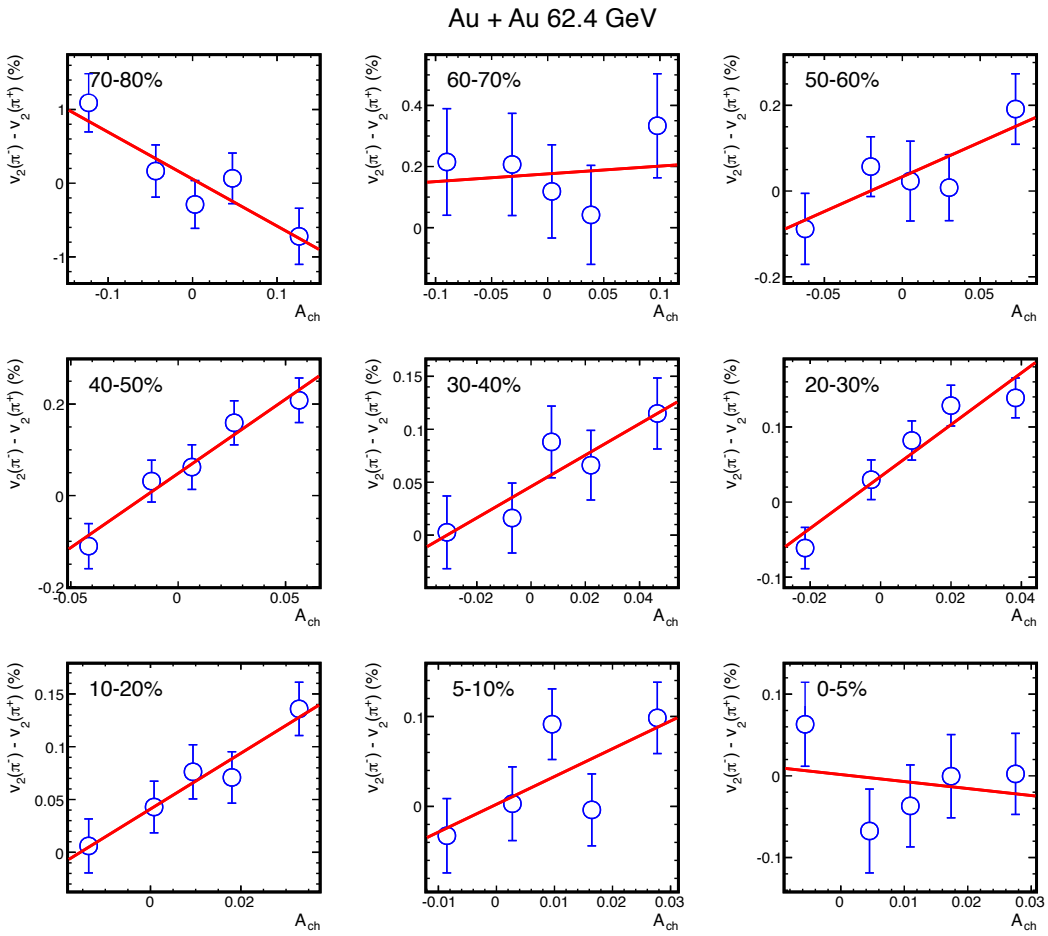


**Figure 4.18**: Integrated $v_2$ difference between $v_2(\pi^-)$ and $v_2(\pi^+)$ as function of charge asymmetry in Au + Au collisions at $\sqrt{s_{NN}}$ = 62.4 GeV. The solid red lines represent the straight line fit, the slope parameter of which is the observable $r = 2q_e/\bar{\rho}_e$.

The extracted slope parameters as a function of centrality in Au + Au collisions at $\sqrt{s_{NN}}$ = 200, 62.4, 39, 27 and 19.6 GeV are shown in Fig. 4.20. From peripheral to central collisions, the slope parameter shows a rise-and-fall feature. This feature can be seen for all energies under study. The magnitude of the slope has no obvious dependence on energy. The theoretical calculation based on chiral magnetic wave are presented as colored lines, to which STAR data has the similar trend and magnitude. The solid black lines are the statistical uncertainty and gray bars are the systematic uncertainties coming from varying DCA cuts for pions and varying tracking efficiency for charged particles. Details of obtaining the systematic uncertainties will be discussed in the next section.

The UrQMD model [BBB98, BZS99] is also used to study the charge asymmetry dependency of pion azimuthal anisotropy in Au + Au collisions at $\sqrt{s_{NN}}$ = 200 GeV. In middle centralities, the slope parameter given by UrQMD is consistent with zero. This study serves as a reference base line for our measurement, and it is also a consistency check as UrQMD does not have charge magnetic wave mechanism built-in.

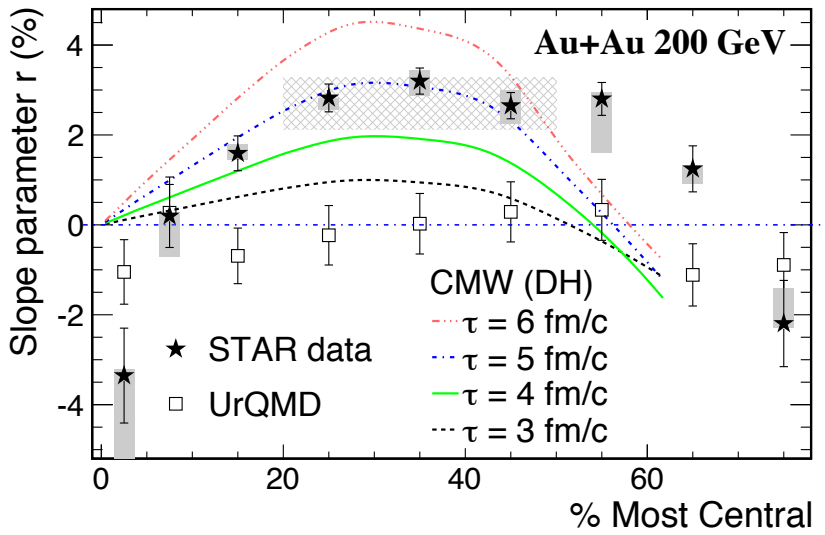


**Figure 4.19**: Slope parameter as a function of centrality in Au + Au collisions at $\sqrt{s_{NN}}$ = 200 GeV. The solid lines are statistical uncertainty, the gray bars include the systematic errors due to the DCA cut and the tracking efficiency. The shaded area represents the STAR measurement with the event plane reconstructed with ZDC-SMDs. The CMW calculation for different duration time as well as the UrQMD model simulation are shown for comparison.

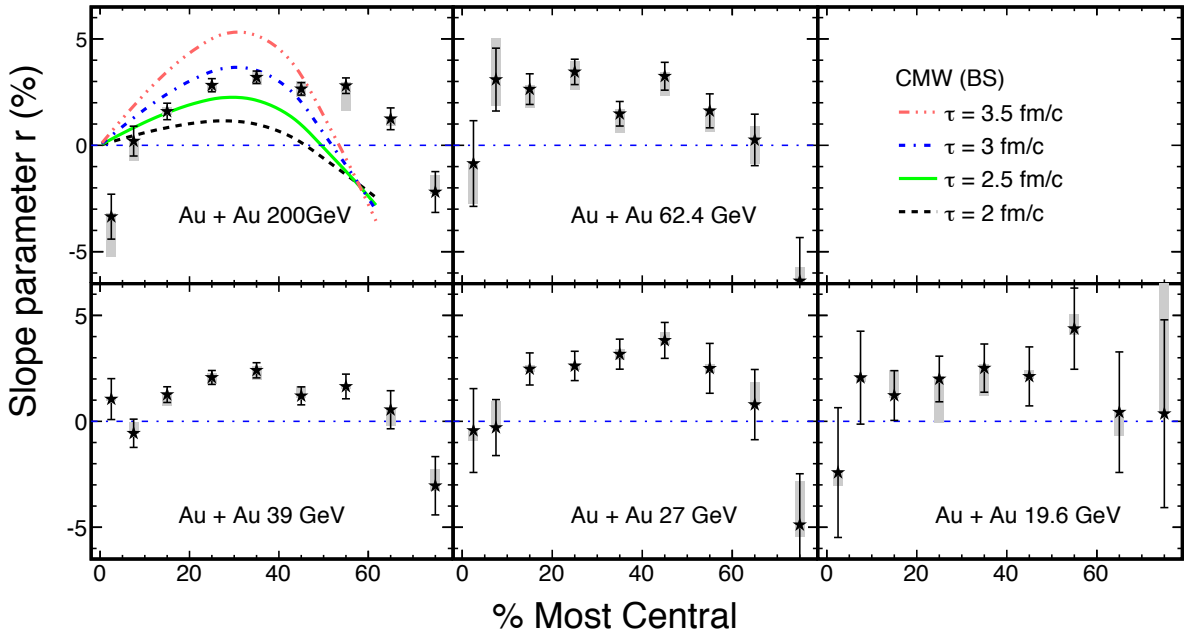


**Figure 4.20**: Slope parameter as a function of centrality in Au + Au collisions at $\sqrt{s_{NN}}$ = 200, 62.4, 39, 27 and 19.6 GeV. Another CMW calculation with different magnetic field calculation is shown for comparison at $\sqrt{s_{NN}}$ = 200 GeV.

## 4.6 Systematic Uncertainties

The gray bars in Fig. 4.20 represent the systematic uncertainty from two sources. The first one is from the non-primarily produced particles. This is studied by varying DCA cut for pions. The default DCA cut for pions selection is 1 cm as listed in Table. 4.2. If the chiral magnetic wave exists, it will affect only primarily produced pions. Decayed pions usually have large DCA. The difference between result from the default DCA cut to that from a tighter cut (DCA < 0.5 cm) is considered as the systematic uncertainty due to the contamination from decayed pions.

The second major systematic uncertainty arises from tracking efficiency of charged particles. As discussed in Sec. 4.3, the tracking efficiency for charged pions are used as that of all charged particles. Even pions dominate the finial state hadrons, this treatment still involves some uncertainty, not to mention that the pion tracking efficiency from embedding samples has it own uncertainty. The uncertainty in tracking efficiency can propagate into the slope measurement by changing the relation between observable $A_{ch}$

and true $A_{ch}$. To investigate this effect, the tracking efficiency is varied by relative 5% and the resulted difference in $r$ is taken as the systematic uncertainty. The total systematic uncertainty showing in Fig. 4.20 are the square root of the sum of these two individual squared systematic uncertainties.

In addition to the effects discussed above, there are still other sources that may influence the slope measurement. First one is the event plane estimation. The TPC tracks are used to estimated the event plane, which approximated the participant plane, and for reasonable event plane resolutions the measured $v_2$ are not the mean values, but closer to the root-mean-square value [OPV09]. The STAR ZDC-SMDs can be used to give a better proxy for the reaction plane. Measurements using ZDC-SMD estimated event plane for 20-50% Au + Au collisions at $\sqrt{s_{NN}}$ = 200 GeV is show in Fig. 4.19

Weak decays, like $\Lambda/\bar{\Lambda}$ may also contribute the $v_2$ and $A_{cj}$ measurement. $\Lambda$ decayed $\pi^+$ and $\pi^-$ have different integrated $v_2$. However, the neutral particle decay will not contribute the net charge of a event, but the total multiplicity. Therefore, the weak decays may create a non-zero interception of $v_2(A_{ch})$, but is it will not create a non-zero slope out of nothing. The observed slope need to be corrected by a scale factor correlated the $\Lambda/\pi$ ratio, which should be smaller than 10% [AAA04b]. The weak effect can also be study via UrQMD model.

# CHAPTER 5

# Discussion

In this chapter, we discuss a few other mechanisms which give alternative interpretations to the difference in $v_2$ between particles and anti-particles, or even the slope parameters of $\Delta v_2(A_{ch})$ observed. Experimental testing of the effect by reducing/turning off the magnetic field, while keep $v_2$ finite, will also be discussed.

## 5.1 Multi-Component Coalescence Model

The Multi-Component Coalescence (MCC) Model [**?**] is among one of the models which expected the splitting of $v_2$ between particles and anti-particles. In this model, it is assumed that hadrons are formed via quark coalescence, i.e. two (three) valence quarks (or "constituent quarks" ) coalesce together to make a meson (baryon). The momentum and $v_2$ of the hadron is the sum of that of the constituent quarks,

$$\overrightarrow{p}_h = \sum_{i=1}^{n} \overrightarrow{p}_{q,i}, \tag{5.1}$$

$$v_2^M(p_T) = v_2^a(x_a p_T) + v_2^b(x_b p_T). \tag{5.2}$$

Eq. (5.1) shows that the hadron momentum is the vector summation of its constituent quarks, and Eq. (5.2) shows that the meson $v_2$ is the summation of its two consistent quarks, $a$ and $b$, weighted by their momentum fractions $x_a$ and $x_b$. A similar equation can be written for hadrons with three constituent quarks each. Eq. (5.2) indicates that $v_2(p_T)/n$ for mesons and hadrons follow the same scaling, while $n = 2(3)$ for mesons (hadrons). This is so-called the number-of-constituent-quark (NCQ) scaling. The STAR experiment at RHIC has already observed such scaling in low $p_T$ range, $p_T \lesssim 1.5$ GeV [AAA05a, Shi09]. The NCQ scaling and quark coalesce mechanisms suggest that all

constituent quarks have the same $v_2^q$.

The MCC model argues that a common $v_2^q$ for all constituents may not be true for the transported quarks and produced quarks. Transported quarks refer to those quarks from the incident nuclei, i.e. $u$ and $d$ quarks transported from $y = y_{\rm beam}$ to $y = 0$. Produced quarks refer to those quarks produced from vacuum in the collision. Transported quarks are believed to suffer more binary collisions than produced quarks. Therefore, $v_2$ of the transported quarks $v_2^{q^T}$ is expected to be larger than $v_2$ of the produced quarks $v_2^{q^P}$. According to this argument, the $v_2$ of final state hadrons can be expressed as

$$v_2^h(p_T) = \sum_{i=1}^{n} \left[ X_{q_i^T} v_2^{q_i^T}(p_T/n) + (1 - X_{q_i^T}) v_2^{q_i^P}(p_T/n) \right], \tag{5.3}$$

where $X_{q_i^T}$ is the transported quark fraction of quark species $q_i$, and $n = 2(3)$ for mesons (baryons). For the $u$ and $d$ quarks, $X_{u^T}$ and $X_{d^T}$ can be estimated from the experimentally measured yield of different particle species. For other quarks, there is no transported fraction. Based on the above assumptions and the quark components, MCC model gives the $v_2$ order of the different hadrons,

$$\begin{aligned} v_2[\pi^- = d\bar{u}] &> v_2[\pi^+ = u\bar{d}], \\ v_2[\mathrm{K}^+ = u\bar{s}] &> v_2[\mathrm{K}^- = \bar{u}s], \\ v_2[p = uud] &> v_2[\bar{p} = \bar{u}\bar{u}\bar{d}], \\ v_2[\Lambda = uds] &> v_2[\bar{\Lambda} = \bar{u}\bar{d}\bar{s}] \end{aligned} \tag{5.4}$$

Since the stopping power is getting stronger with the decreasing collision energy, the fraction of transported quarks should be larger at a lower energy. Therefore, the MCC model expects that the differences expressed in Eq. (5.4) should increase with the decreasing colliding energy.

In STAR, such splitting of $v_2$ between particles and anti-particles have been observed [Shi12], as shown in Fig. 5.1. The order of $v_2$ for different particles and their anti-particles is consistent with the expectation of MCC model and larger $v_2$ differences is observed at lower colliding energies than that at high energies.

A recent study based on MCC model further investigated the $v_2$ difference between $\pi^+$ and $\pi^-$ as a function of event-by-event charge asymmetry [CDL12]. It is found that

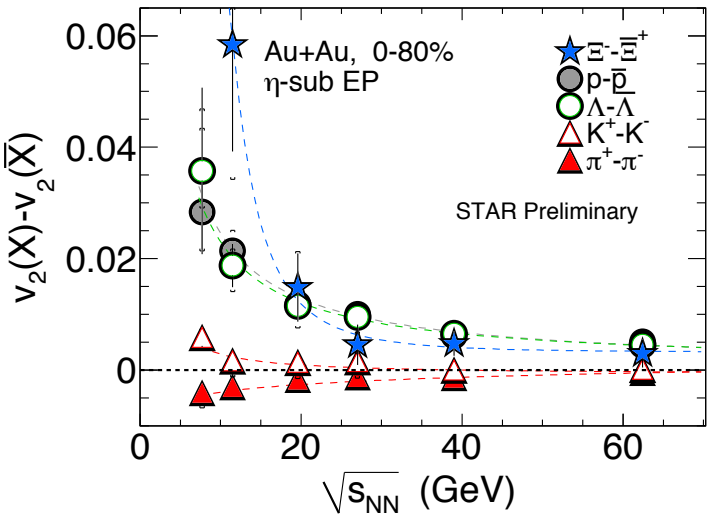


**Figure 5.1**: Integrated $v_2$ difference between particles and their corresponding anti-particles from 7.7 GeV to 62.4 GeV in Au + Au collisions (0-80%). The solid vertical lines represent the statistical uncertainties and the caps represent the systematic uncertainties. Dashed lines are fits to data. Figure taken from [Shi12].

MCC model expects a negative correlation between $v_2(\pi^-) - v_2(\pi^+)$ and charge asymmetry, which is opposite to what have been observed in data. Nevertheless, quark stopping described in MCC model may still have contribution to the non-zero interception of the function $\Delta v_2(A_{ch})$.

## 5.2 AMPT Model with Hardonic and Partonic Potential

The AMPT model [LKL05] is widely used to describe a variety of phenomenon observed in experiments. The string melting version of AMPT model uses HIJING [GW94] as the initial input, and converts hadrons generated by HIJING to constituent quarks and anti-quarks. The parton phase is managed by the Zhang's parton cascade (ZPC) model [Zha98]. The hadronization in AMPT is done by a spatial coalesce model, and the hadronic phase evolution is described by a relativistic transport (ART) model [LK95]. However, the string melting version of AMPT model does not give a difference

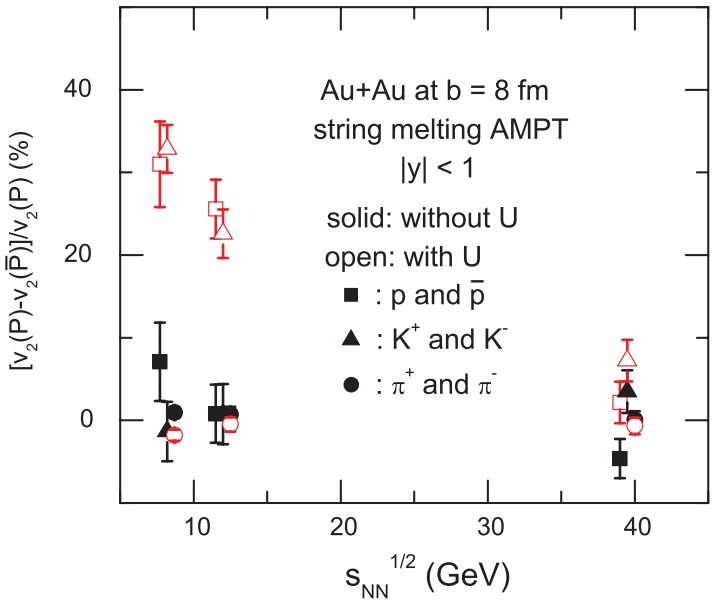


**Figure 5.2**: Integrated $v_2$ difference between $p$ and $\bar{p}$, $K^+$ and $K^-$, $\pi^+$ and $\pi^-$ given by the AMPT model with or without hardonic potential in Au + Au collisions at $\sqrt{s_{NN}}$ = 7.7, 11.5 and 39 GeV. Figure taken from [XCK12].

in $v_2$ between particles and anti-particles, as shown by black symbols in Fig. 5.2.

In a recent study [XCK12] the parton scattering cross section and the ending time of the partonic stage have been adjusted for lower collision energies in ZPC. More importantly, the ART model is also extended to include mean field potentials of baryons, kaons, and pions. With those included, the AMPT model can qualitatively reproduce the $v_2$ splitting between particles and anti-particles in Au + Au collisions at $\sqrt{s_{NN}}$ = 7.7, 11.5 and 39 GeV. The adjusted AMPT results are shown by the open red symbols in Fig. 5.2. In addition, the mean field potential is also expected to increase with the charge asymmetry $A_{ch}$. Thus it may offer an alternative interpretation of the increase of $v_2(\pi^-) - v_2(\pi^+)$ with increasing $A_{ch}$. However, detailed calculation is not available at this point.

In a similar study, the elliptic flow of particles and antiparticles are studied with the consideration of mean field potential from partonic phase instead of hadronic phase, it also gives a $v_2$ difference between particles and antiparticles. However, it did not provide the calculation for pions, thus prevents us from making a comparison [SPG12].

## 5.3 Test Chiral Magnetic Effects in U + U Collisions

The chiral charge related effects under discussion, including the chiral magnetic effect, the chiral separation effect and the chiral magnetic wave, require a strong magnetic field generated in heavy ion collisions. Besides the chiral magnetic effect and local parity violation, there are arguments that the observed three-particle correlation Eq. 4.18 may originated from other sources, for example, cluster particle correlations [Wan10] as well as charge and momentum conservation overlaid with elliptic flow [Pra10]. Because of the two particles, $\alpha$ and $\beta$ in Eq. 4.18, may come from the same cluster, e.g. resonance, jets and di-jets, and those clusters may have $v_2$ themselves or have different emission pattern between in-plane and out-of-plane direction [Vol10], they can contribute to the three-particle correlation. Form the point of view of a global momentum and charge conservation [Pra10, SP11], the whole collision system can be treated as a cluster. In addition, in Au + Au collisions the strongest magnetic field can only be found in middle collisions in which $v_2$ is also large. When the magnetic field and $v_2$ are entangled, it is difficult to rule out if the LPV or CMW observables have a non-trivial correlation with $v_2$ instead of the magnetic field.

Because of the unique geometry of uranium nucleus, U + U collision is an excellent test bed for the magnetic field and $v_2$ related physics [Vol10]. Fully-overlapped U + U collision was originally suggested to be used to study hydrodynamic behavior of elliptic flow, because it can provide much larger and denser collision system than the middle central Au + Au collisions [HK05]. In contrast to the Au nucleus which has a round shape, uranium nucleus is a prolate spheroid with much larger difference between the long and short axes. There are two special configurations of fully-overlapped U + U collisions, namely, body-body collision and tip-top collision. Body-body (tip-tip) collision refers to the long (short) axes of the two nuclei are in parallel to each other, as shown by the cartoons in Fig. 5.4. The body-body configuration is of special interest, because with it the two uranium nuclei are fully-overlapped and it yields minimum spectators, i.e. weakest magnetic field. However, because of its geometry, $v_2$ is still sizable, as shown in Fig. 5.3. This configuration makes the disentangling of magnetic field and $v_2$ possible.

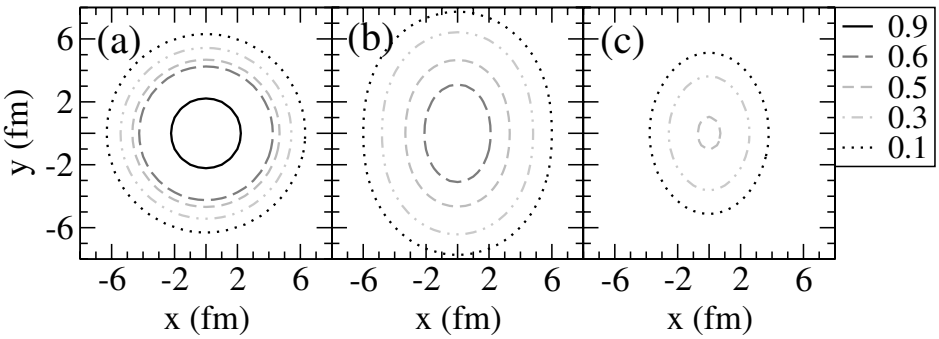


**Figure 5.3**: Entropy density contours for a) tip-tip U + U collisions, b) body-body U + U collisions and c) most central Au + Au collisions.

Experimentally, body-body events can be selected by cutting on ZDC coincidence rate and multiplicity. By cutting on the lowest ZDC coincidence rate, fully-overlapped events can be selected. Within this sample, there are body-body events, tip-tip events and other configurations in between. Because that body-body events have the long axes lining up in parallel, the number of binary collisions between quarks should be the minimum. On the contrary, the number of binary collisions between quarks in tip-tip collisions should reach the maximum. Therefore, within the fully-overlapped event sample, body-body events tend to yield the minimum multiplicity and tip-tip events tend to yield the maximum multiplicity. In Fig. 5.4, the multiplicity distribution of the 1% events with the lowest ZDC coincidence measured by STAR high level trigger. It is expected that the low multiplicity end is body-body events rich and the high multiplicity end is tip-tip events rich.

The three-particle correlation, Eq. 4.18, as a signal of the chiral magnetic effect has been measured in U + U collisions and compared with that in Au + Au collisions. The left panel of Fig. 5.5 shows the direct comparison of three-particle correlation in U + U and Au + Au collisions in all centralities. Denoting the opposite sign correlation by $\gamma_{OS}$ and the same sign correlation by $\gamma_{SS}$, $\gamma_{OS} - \gamma_{SS}$ is believed to be a better observable because some background is canceled. In the right panel of Fig. 5.5 $(\gamma_{OS} - \gamma_{SS}) \cdot N_{\rm part}$ is shown as a function of $v_2$. The blue point with the smallest $v_2$ corresponding to the 0-1% central collisions of U + U collisions. It can be seen that the signal seems disappears, where $v_2$ is still sizable. The LPV analysis in U + U collisions is still ongoing and this

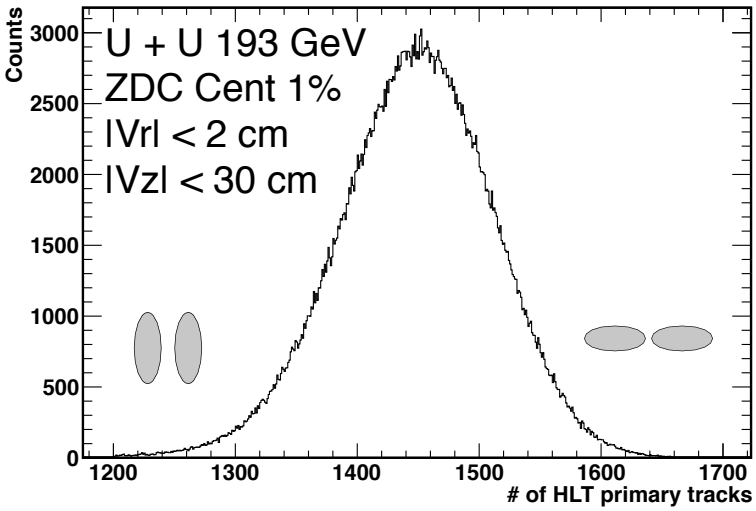


**Figure 5.4**: STAR HLT measured multiplicity distribution of most central, top 1% ZDC coincidence rate, U + U collisions at $\sqrt{s_{NN}}$ = 193 GeV. The low and high multiplicity ends are believed to be body-body and tip-tip collisions rich.

subject is not conclusive yet.

The pion event anisotropy as a function of event-by-event charge asymmetry can also be performed in body-body U + U collisions. Based on same arguments made above, with finite $v_2$ but almost zero magnetic field, the slope parameters ( Eq. 4.13) observed in Au + Au collisions should vanish if it is caused by the chiral magnetic wave.

In additional, a recent study [BB13] proposed two mechanisms which can also generate non-zero slope parameters. The first one is based on the pseudo-rapidity dependency of $v_2$ and a finite detector acceptance. The second is based on the local charge conservation. The quantitative estimation from the experimental side on both of these two mechanisms are under study.

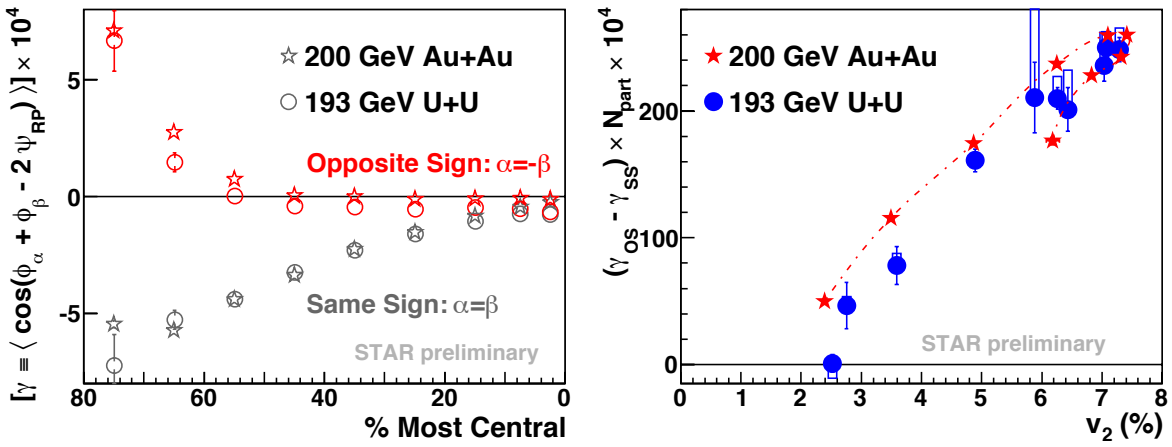


**Figure 5.5**: Chiral Magnetic Effect measurement in U + U collisions at 193 GeV comparing to that in Au + Au collisions at 200 GeV.

# CHAPTER 6

# Summary and Outlook

## 6.1 Summary

In this dissertation, we discussed the development of the STAR High-Level Trigger as well as the measurement of the charged pion azimuthal anisotropy as a function event-by-event charge asymmetry in Au + Au collisions for all centralities at $\sqrt{s_{NN}}$ = 200, 62.4, 39, 27 and 19.6 GeV.

The STAR High-Level Trigger is playing an important role in the current data taking in STAR. With its capability of real time track reconstruction and event assembling, STAR HLT selects event with special physics interests, including high $p_T$ , di-electron, light nuclei, while rejects most of the background events. With the help of HLT, STAR timely made the observation of anti-helium-4 nuclei and the measurement of $J/\psi$ elliptic flow. Other triggers, such as single electron, ultra-peripheral collision, can be easily implemented per request. Currently the main detectors used by STAR HLT are TPC, BEMC and TOF. However, the ability of incorporating new detectors is an existing feature of STAR HLT. Next year, the MTD and HFT will be fully installed and their information can also be integrated into HLT. During the RHIC beam energy scan program, HLT is used to monitor the good collision out of beam background collisions, because of its irreplaceable ability of real time vertex position reconstruction. This year the STAR HLT is undergoing a major upgrade. As the first step, a cellular automaton (CA) based track finder is used to replace the original conformal mapping based tracker. The second step is to decouple HLT tracking from DAQ computers, and operate on an independent online computer farm. The testing of the new HLT with CA tracker is on going.

The physics analysis discussed in this dissertation is about the Beam Energy, Collision Centrality and charge asymmetry dependency of pion event azimuthal anisotropy in Au + Au collisions. Theoretical studies argue that because of the possible chiral symmetry restoration and extremely strong magnetic field created, chiral magnetic effect (CME) and chiral separation effect (CSE) should exist in heavy ion collisions. Recent calculations pointed out that CME and CSE can couple with each other and induce density waves of electric and chiral charge – the chiral magnetic wave (CMW). The CMW can induce an electric quadrupole momentum in the fireball, and the electric quadrupole momentum acquires more positive charge near the two poles of the fireball and more negative charge near the equator. Such a configuration can be reflected by the azimuthal anisotropy $v_2$ of charge pions, because of the similar absorption cross section of $\pi^+$ and $\pi^-$. If the electric quadrupole induced by the CMW exists, $v_2$ of $\pi^+(\pi^-)$ is expected to decrease (increase) linearly with the increasing charge asymmetry $A_{ch}$. The $v_2$ difference between $\pi^+$ and $\pi^-$ should be proportional to the charge asymmetry and slope of this relation reflects the electric quadrupole momentum. We measured the integrated $v_2$ of $\pi^+$ and $\pi^-$ in $0.15 < p_T < 0.5$ GeV/c and $|\eta| < 1$ with two particle cumulant method and $\eta$-sub event method in Au + Au collisions at $\sqrt{s_{NN}} = 200, 62.4, 39, 27$ and 19.6 GeV. In middle centralities, it is found that integrated $v_2$ of $\pi^+(\pi^-)$ decreases (increases) linearly with the increasing charge asymmetry. The slope values of $\pi^+$ and $\pi^-$ are similar. The slope parameters of $\Delta v_2(A_{ch})$ have been extracted for all centralities and all energies under study. The slope parameters shows a rise and fall feature from most central to most peripheral collisions, which is similar to the theoretical calculations based on CMW. From 200 GeV to 27 GeV, the slope parameter as a function only shows a weak energy dependence.

## 6.2 Future Development of the STAR High-Level Trigger

There is an ongoing effort to adopt the CA tracker in STAR HLT. Based on previous tests performed by STAR offline computing team, CA tracker provides better tracking efficiency with comparable speed. In the future, a Kalman filter based particle reconstruction package will be in place, after the CA tracker, to reconstruct primary and secondary vertices. Using Kalman filter technology, KFParticle treat the tracks given by CA tracker as measurements and try to fit the position and momentum of a vertex. Because the mathematics in Kalman filter is only small matrix manipulations, KFParticle is demonstrated to be much faster than the conventional topological reconstruction method.

The technical reason for which we are interested in the CA tracker and KFParticle is the trend of migrating to parallel computing. The increasing trend of CPU frequency saturated recently. To fulfill the increasing requirements of the computing power, multi-core and even many-core architecture are believed to be the direction of future. The last version of the STAR HLT is a transitional single thread application, which is not aware of the new hardware architecture. However, the CA tracker is designed as a multi-thread application, which can run on the latest multi-core CPUs in order to gain higher performance. On the other hand, the intrinsic parallelism of the algorithm of CA tracker is suitable to be executed in the SIMD or vector mode. The new development on the SIMD instruction set in recent years provide even more performance margin for the vectorized application. Fortunately, the vectorized CA track finder and Kalman filter have already been developed and ready to use. Therefore, adopting the CA tracker and KFParticle gives STAR HLT the ability to leverage the cutting edge computing technologies.

An more ambitious attempt on the high performance computing is to offload the most computing intensive part to general purpose GPU (GPGPU) or many integrated core (MIC) accelerator to reach extremely high performance. This idea is based on the

fact that the most computing intensive part is usually repetitive and independent tasks taking over a large data sample. If those tasks can be distributed over tens of cores (MIC) or even thousands of cores (GPGPU), an extremely high overall throughput maybe achieved. We have demonstrated that GPGPU can easily increase the performance of a V0 finder by a factor of ten. Study on the accelerating of CA tracker and KFParticle by Intel's MIC architecture is on going. We have contacted Intel for cooperation and support. STAR HLT will study the possibility of deploying MIC accelerator in a large scale.

## 6.3 Outlook for the Charge Asymmetry Dependency of Pion Event Azimuthal Anisotropy

As discussed before, $\pi^+$ and $\pi^-$ from $\Lambda(\bar{\Lambda})$ decay may contribute different integrated $v_2$, because of the different yield of $\Lambda$ and $\bar{\Lambda}$. Although we have concluded that this weak decay effect can not create a slope out of nothing, it may alter an existing slope. Therefore, it is necessary to check the magnitude of this effect via Monte-Carlo model. We plan to use UrQMD model to trace the $\Lambda(\bar{\Lambda})$ decayed daughters to study this effect.

It is pointed out[KY11] that the CMW effect may be less visible in other particles species other than pions, because of their larger hardonic cross section between particles and antiparticles. Thus a surprisingly large slope parameters of $\Delta v_2(A_{ch})$ obtained from other particle species may change the picture significantly. For a comprehensive understanding it is also useful to check the charge asymmetry dependency of $v_2$ of particles other than pions.

In body-body U + U collisions, magnetic field is turned off while $v_2$ remains finite. Thus one should not observe a finite slope of $v_2(A_{ch})$ or $\Delta v_2(A_{ch})$ for charged pions. The measurement from U+U collisions with special configuration selection will serve as an important consistency check.

When all of the above checks are done, hopefully we will have a better understanding of the phenomena and the dynamics that lead to it.

# References

[AAA03] STAR Collaboration, K. H. Ackermann *et al.*, STAR detector overview, *Nuclear Instruments and Methods in Physics Research Section A: Accelerators, Spectrometers, Detectors and Associated Equipment*, **499**, 624 – 632, 2003.

[AAA04a] STAR Collaboration, J. Adams *et al.*, Particle-Type Dependence of Azimuthal Anisotropy and Nuclear Modification of Particle Production in Au + Au Collisions at $\sqrt{s_{NN}}$ = 200 GeV, *Phys. Rev. Lett.*, **92**, 052302, 2004.

[AAA04b] STAR Collaboration, J. Adams *et al.*, Multistrange Baryon Production in Au-Au Collisions at $\sqrt{s_{NN}}$ = 130 GeV, *Phys. Rev. Lett.*, **92**, 182301, 2004.

[AAA05a] STAR Collaboration, J. Adams *et al.*, Azimuthal anisotropy in Au+Au collisions at $\sqrt{s_{NN}} = 200GeV$, *Phys. Rev. C*, **72**, 014904, 2005.

[AAA05b] The STAR Collaboration, J. Adams *et al.*, Experimental and theoretical challenges in the search for the quark-gluon plasma: The STAR Collaboration's critical assessment of the evidence from RHIC collisions, *Nuclear Physics A*, **757**, 102 – 183, 2005.

[AAA05c] The PHENIX Collaboration, K. Adcox *et al.*, Formation of dense partonic matter in relativistic nucleus-nucleus collisions at RHIC: Experimental evaluation by the PHENIX Collaboration, *Nuclear Physics A*, **757**, 184 – 283, 2005.

[AAA07] STAR Collaboration, B. I. Abelev *et al.*, Mass, quark-number, and $\sqrt{s_{NN}}$ dependence of the second and fourth flow harmonics in ultrarelativistic nucleus-nucleus collisions, *Phys. Rev. C*, **75**, 054906, 2007.

[AAA09] STAR Collaboration, B. I. Abelev *et al.*, Azimuthal Charged-Particle Correlations and Possible Local Strong Parity Violation, *Phys. Rev. Lett.*, **103**, 251601, 2009.

[AAA10a] STAR Collaboration, B. I. Abelev *et al.*, Observation of charge-dependent azimuthal correlations and possible local strong parity violation in heavy-ion collisions, *Phys. Rev. C*, **81**, 054908, 2010.

[AAA10b] STAR Collaboration, M. M. Aggarwal *et al.*, Higher Moments of Net Proton Multiplicity Distributions at RHIC, *Phys. Rev. Lett.*, **105**, 022302, 2010.

[AAA10c] STAR Collaboration, M. M. Aggarwal *et al.*, An Experimental Exploration of the QCD Phase Diagram: The Search for the Critical Point and the Onset of De-confinement, 2010, arXiv:1007.2613v1 [nucl-ex].

[AAA11] STAR Collaboration, H. Agakishiev *et al.*, Observation of the antimatter helium-4 nucleus, *Nature*, **473**, 353–356, 2011.

[AAA13] STAR Collaboration, L. Adamczyk *et al.*, Observation of an Energy-Dependent Difference in Elliptic Flow between Particles and Antiparticles in Relativistic Heavy Ion Collisions, *Phys. Rev. Lett.*, **110**, 142301, 2013.

[ABB94] S. Ahlen *et al.*, An antimatter spectrometer in space, *Nuclear Instruments and Methods in Physics Research Section A: Accelerators, Spectrometers, Detectors and Associated Equipment*, **350**, 351 – 367, 1994.

[ABB03a] STAR Collaboration, M. Anderson *et al.*, The STAR time projection chamber: a unique tool for studying high multiplicity events at RHIC, *Nuclear Instruments and Methods in Physics Research Section A: Accelerators, Spectrometers, Detectors and Associated Equipment*, **499**, 659 – 678, 2003.

[ABB03b] M. Anderson *et al.*, A readout system for the STAR time projection chamber, *Nuclear Instruments and Methods in Physics Research Section A: Accelerators, Spectrometers, Detectors and Associated Equipment*, **499**, 679 – 691, 2003.

[ABB05] BRAHMS, I. Arsene *et al.*, Quark-gluon plasma and color glass condensate at RHIC? The perspective from the BRAHMS experiment, *Nuclear Physics A*, **757**, 1 – 27, 2005.

[ABD03] C. Adler *et al.*, The STAR Level-3 trigger system, *Nuclear Instruments and Methods in Physics Research Section A: Accelerators, Spectrometers, Detectors and Associated Equipment*, **499**, 778 – 791, 2003.

[ADG03] C. Adler *et al.*, The RHIC zero-degree calorimeters, *Nuclear Instruments and Methods in Physics Research Section A: Accelerators, Spectrometers, Detectors and Associated Equipment*, **499**, 433 – 436, 2003.

[BAB12] Particle Data Group, J. Beringer *et al.*, Review of Particle Physics, *Phys. Rev. D*, **86**, 010001, 2012.

[BB13] A. Bzdak and P. Bozek, Contributions to the event-by-event charge asymmetry dependence for the elliptic flow of $\pi^+$ and $\pi^-$ in heavy-ion collisions, 2013, 1303.1138.

[BBB97] J. Barrette *et al.*, Proton and pion production relative to the reaction plane in Au + Au collisions at 11$A$ GeV/$c$, *Phys. Rev. C*, **56**, 3254–3264, 1997.

[BBB98] S. Bass *et al.*, Microscopic models for ultrarelativistic heavy ion collisions, *Progress in Particle and Nuclear Physics*, **41**, 255 – 369, 1998.

[BBB05] PHOBOS, B. Back *et al.*, The PHOBOS perspective on discoveries at RHIC, *Nuclear Physics A*, **757**, 28 – 101, 2005.

[BCE03] F. Bieser *et al.*, The STAR trigger, *Nuclear Instruments and Methods in Physics Research Section A: Accelerators, Spectrometers, Detectors and Associated Equipment*, **499**, 766 – 777, 2003.

[BCW98] A. J. Baltz, C. Chasman, and S. N. White, Correlated forward-backward dissociation and neutron spectra as a luminosity monitor in heavy-ion colliders, *Nuclear Instruments and Methods in Physics Research Section A: Accelerators, Spectrometers, Detectors and Associated Equipment*, **417**, 1 – 8, 1998.

[BDO01a] N. Borghini, P. M. Dinh, and J.-Y. Ollitrault, Flow analysis from cumulants: a practical guide, 2001, arXiv:nucl-ex/0110016v1.

[BDO01b] N. Borghini, P. M. Dinh, and J.-Y. Ollitrault, Flow analysis from multiparticle azimuthal correlations, *Phys. Rev. C*, **64**, 054901, 2001.

[BDO01c] N. Borghini, P. M. Dinh, and J.-Y. Ollitrault, New method for measuring azimuthal distributions in nucleus-nucleus collisions, *Phys. Rev. C*, **63**, 054906, 2001.

[BFR85] P. Billoir, R. Frühwirth, and M. Regler, Track element merging strategy and vertex fitting in complex modular detectors, *Nuclear Instruments and Methods in Physics Research Section A: Accelerators, Spectrometers, Detectors and Associated Equipment*, **241**, 115 – 131, 1985.

[Bil84] P. Billoir, Track fitting with multiple scattering: A new method, *Nuclear Instruments and Methods in Physics Research*, **225**, 352 – 366, 1984.

[Bil12] A. Bilandzic. *Anisotropic Flow Measurements in ALICE at the Large Hadron Collider*. PhD thesis, Utrecht University,

[BKL10] A. Bzdak, V. Koch, and J. Liao, Remarks on possible local parity violation in heavy ion collisions, *Phys. Rev. C*, **81**, 031901, 2010.

[BKL11] Y. Burnier, D. E. Kharzeev, J. Liao, and H.-U. Yee, Chiral Magnetic Wave at Finite Baryon Density and the Electric Quadrupole Moment of the Quark-Gluon Plasma, *Phys. Rev. Lett.*, **107**, 052303, 2011, arXiv:1103.1307v1 [hep-ph].

[BS07] P. Braun-Munzinger and J. Stachel, The quest for the quark–gluon plasma, *Nature*, **448**, 302–309, 2007.

[BSV11] A. Bilandzic, R. Snellings, and S. Voloshin, Flow analysis with cumulants: Direct calculations, *Phys. Rev. C*, **83**, 044913, 2011, arXiv:1010.0233v1 [nucl-ex].

[BZS99] M. Bleicher *et al.*, Relativistic hadron-hadron collisions in the ultra-relativistic quantum molecular dynamics model, *Journal of Physics G: Nuclear and Particle Physics*, **25**, 1859, 1999.

[CDL12] J. Campbell, J. Dunlop, M. Lisa, and P. Sorensen. Can baryon stopping explain the breakdown of constituent quark scaling and proposed signals of chiral magnetic waves at RHIC? Quark Matter 2012, poster, 2012.

[CP75a] N. Cabibbo and G. Parisi, Exponential hadronic spectrum and quark liberation, *Physics Letters B*, **59**, 67 – 69, 1975.

[CP75b] J. C. Collins and M. J. Perry, Superdense Matter: Neutrons or Asymptotically Free Quarks?, *Phys. Rev. Lett.*, **34**, 1353–1356, 1975.

[CS74] S.-S. Chern and J. Simons, Characteristic Forms and Geometric Invariants, *Annals of Mathematics*, **99**, 48–69, 1974.

[Den88] B. Denby, Neural networks and cellular automata in experimental high energy physics, *Computer Physics Communications*, **49**, 429 – 448, 1988.

[Dia03] D. Diakonov, Instantons at work, *Progress in Particle and Nuclear Physics*, **51**, 173 – 222, 2003.

[Don05] X. Dong. *Single Electron Transverse Momentum and Azimuthal Anisotropy Distributions: Charm Hadron Production at RHIC*. PhD thesis, University of Science and Technology of China, Hefei, China,

[Don12] X. Dong, Highlights from STAR, 2012, arXiv:1210.6677 [nucl-ex].

[FBB12] W. Fischer *et al.* RHIC Collider Projections (FY 2013 – FY 2017). 2012.

[FG72] H. Fritzsch and M. Gell-Mann. Current algebra: Quarks and what else? volume 2, p. 135, 1972. Proceedings of the XVI International Conference on High Energy Physics.

[FH11] K. Fukushima and T. Hatsuda, The phase diagram of dense QCD, *Reports on Progress in Physics*, **74**, 014001, 2011.

[Fru87] R. Frühwirth, Application of Kalman filtering to track and vertex fitting, *Nuclear Instruments and Methods in Physics Research Section A: Accelerators, Spectrometers, Detectors and Associated Equipment*, **262**, 444 – 450, 1987.

[GHK12] B. Gaster, L. Howes, D. R. Kaeli, P. Mistry, and D. Schaa. *Heterogeneous Computing with OpenCL*. Elsevier Inc.,

[GK07] S. Gorbunov and I. Kisel. Reconstruction of decayed particles based on the Kalman filter. CBM-SOFT-note-2007-003, 2007.

[GKK93] A. Glazov, I. Kisel, E. Konotopskaya, and G. Ososkov, Filtering tracks in discrete detectors using a cellular automaton, *Nuclear Instruments and Methods in Physics Research Section A: Accelerators, Spectrometers, Detectors and Associated Equipment*, **329**, 262 – 268, 1993.

[GKK08] S. Gorbunov, U. Kebschull, I. Kisel, V. Lindenstruth, and W. Mller, Fast SIMDized Kalman filter based track fit, *Computer Physics Communications*, **178**, 374 – 383, 2008.

[GLM11] S. Gupta, X. Luo, B. Mohanty, H. G. Ritter, and N. Xu, Scale for the Phase Diagram of Quantum Chromodynamics, *Science*, **332**, 1525–1528, 2011.

[GMS11] E. V. Gorbar, V. A. Miransky, and I. A. Shovkovy, Normal ground state of dense relativistic matter in a magnetic field, *Phys. Rev. D*, **83**, 085003, 2011.

[GRA11] S. Gorbunov *et al.*, ALICE HLT High Speed Tracking on GPU, *Nuclear Science, IEEE Transactions on*, **58**, 1845 –1851, 2011.

[Gro87] H. Grote, Pattern recognition in high-energy physics, *Reports on Progress in Physics*, **50**, 473, 1987.

[GW73] D. J. Gross and F. Wilczek, Ultraviolet Behavior of Non-Abelian Gauge Theories, *Phys. Rev. Lett.*, **30**, 1343–1346, 1973.

[GW94] M. Gyulassy and X.-N. Wang, HIJING 1.0: A Monte Carlo program for parton and particle production in high energy hadronic and nuclear collisions, *Computer Physics Communications*, **83**, 307 – 331, 1994.

[HFF03] H. Hahn *et al.*, The RHIC design overview, *Nuclear Instruments and Methods in Physics Research Section A: Accelerators, Spectrometers, Detectors and Associated Equipment*, **499**, 245 – 263, 2003.

[HK05] U. Heinz and A. Kuhlman, Anisotropic Flow and Jet Quenching in Ultrarelativistic U + U Collisions, *Phys. Rev. Lett.*, **94**, 132301, 2005.

[HKH01] P. Huovinen, P. Kolb, U. Heinz, P. Ruuskanen, and S. Voloshin, Radial and elliptic flow at RHIC: further predictions, *Physics Letters B*, **503**, 58 – 64, 2001.

[Kal60] R. E. Kalman, A New Approach to Linear Filtering and Prediction Problems, *Transactions of the ASME–Journal of Basic Engineering*, **82**, 35–45, 1960.

[Kar02] F. Karsch, Lattice results on QCD thermodynamics, *Nuclear Physics A*, **698**, 199 – 208, 2002, arXiv:hep-ph/0103314.

[Kis06] I. Kisel, Event reconstruction in the CBM experiment, *Nuclear Instruments and Methods in Physics Research Section A: Accelerators, Spectrometers, Detectors and Associated Equipment*, **566**, 85 – 88, 2006.

[Kis08] I. Kisel. Reconstruction of tracks in high energy physics experiments. Habilitation Thesis, 2008.

[KKK97] I. Kisel, E. Konotopskaya, and V. Kovalenko, Elastic neural net for track and vertex search, *Nuclear Instruments and Methods in Physics Research Section A: Accelerators, Spectrometers, Detectors and Associated Equipment*, **389**, 167 – 168, 1997.

[KL12] M. Kretz and V. Lindenstruth, Vc: A C++ library for explicit vectorization, *Software: Practice and Experience*, **42**, 1409–1430, 2012.

[KLP00] F. Karsch, E. Laermann, and A. Peikert, The pressure in 2, 2+1 and 3 flavour QCD, *Physics Letters B*, **478**, 447 – 455, 2000, arXiv:hep-lat/0002003.

[KM84] F. R. Klinkhamer and N. S. Manton, A saddle-point solution in the Weinberg-Salam theory, *Phys. Rev. D*, **30**, 2212–2220, 1984.

[KMW08] D. E. Kharzeev, L. D. McLerran, and H. J. Warringa, The effects of topological charge change in heavy ion collisions: "Event by event and violation", *Nuclear Physics A*, **803**, 227 – 253, 2008.

[KPT98] D. Kharzeev, R. D. Pisarski, and M. H. G. Tytgat, Possibility of Spontaneous Parity Violation in Hot QCD, *Phys. Rev. Lett.*, **81**, 512–515, 1998.

[Kre09] M. Kretz. *Effcient Use of Multi- and Many-Core Systems with Vectorization and Multithreading*. PhD thesis, University of Heidelberg,

[KSY10] K.-Y. Kim, B. Sahoo, and H.-U. Yee, Holographic chiral magnetic spiral, *Journal of High Energy Physics*, **2010**, 1–20, 2010.

[KY11] D. Kharzeev and H.-U. Yee, Chiral magnetic wave, *Physical Review D*, **83**, 085007, 2011.

[LK95] B.-A. Li and C. M. Ko, Formation of superdense hadronic matter in high energy heavy-ion collisions, *Phys. Rev. C*, **52**, 2037–2063, 1995.

[LK04] V. Lindenstruth and I. Kisel, Overview of trigger systems, *Nuclear Instruments and Methods in Physics Research Section A: Accelerators, Spectrometers, Detectors and Associated Equipment*, **535**, 48–56, 2004.

[LKL05] Z.-W. Lin, C. M. Ko, B.-A. Li, B. Zhang, and S. Pal, Multiphase transport model for relativistic heavy ion collisions, *Phys. Rev. C*, **72**, 064901, 2005.

[LLL03] J. M. Landgraf *et al.*, An overview of the STAR DAQ system, *Nuclear Instruments and Methods in Physics Research Section A: Accelerators, Spectrometers, Detectors and Associated Equipment*, **499**, 762 – 765, 2003.

[LY56] T. D. Lee and C. N. Yang, Question of Parity Conservation in Weak Interactions, *Phys. Rev.*, **104**, 254–258, 1956.

[Man83] N. S. Manton, Topology in the Weinberg-Salam theory, *Phys. Rev. D*, **28**, 2019–2026, 1983.

[Man04] R. Mankel, Pattern recognition and event reconstruction in particle physics experiments, *Reports on Progress in Physics*, **67**, 553, 2004.

[Mat87] T. Matsui, Dynamical evolution of the quark-gluon plasma and phenomenology, *Nuclear Physics A*, **461**, 27 – 48, 1987.

[McL10] L. McLerran, The Color Glass Condensate and Small x Physics: 4 Lectures, 2010, hep-ph/0104285.

[Moo06] G. E. Moore, Cramming more components onto integrated circuits, Reprinted from Electronics, volume 38, number 8, April 19, 1965, pp.114 ff., *Solid-State Circuits Newsletter, IEEE*, **11**, 33 –35, 2006.

[MS99] R. Mankel and A. Spiridonov, The Concurrent Track Evolution algorithm: extension for track finding in the inhomogeneous magnetic field of the HERA-B spectrometer, *Nuclear Instruments and Methods in Physics Research Section A: Accelerators, Spectrometers, Detectors and Associated Equipment*, **426**, 268 – 282, 1999.

[MZ05] M. A. Metlitski and A. R. Zhitnitsky, Anomalous axion interactions and topological currents in dense matter, *Phys. Rev. D*, **72**, 045011, 2005.

[OPV09] J.-Y. Ollitrault, A. M. Poskanzer, and S. A. Voloshin, Effect of flow fluctuations and nonflow on elliptic flow methods, *Phys. Rev. C*, **80**, 014904, 2009.

[Pet89] C. Peterson, Track finding with neural networks, *Nuclear Instruments and Methods in Physics Research Section A: Accelerators, Spectrometers, Detectors and Associated Equipment*, **279**, 537 – 545, 1989.

[Pol73] H. D. Politzer, Reliable Perturbative Results for Strong Interactions?, *Phys. Rev. Lett.*, **30**, 1346–1349, 1973.

[Pra10] S. Pratt, Alternative Contributions to the Angular Correlations Observed at RHIC Associated with Parity Fluctuations, 2010, arXiv:1002.1758 [nucl-th].

[PV98] A. M. Poskanzer and S. A. Voloshin, Methods for analyzing anisotropic flow in relativistic nuclear collisions, *Phys. Rev. C*, **58**, 1671–1678, 1998.

[Qiu11] H. Qiu. *STAR High Level Trigger and $J/\psi$ Elliptic Flow.* PhD thesis, Institute of Modern Physics, Chinese Academy of Sciences, Lanzhou, China,

[SBD06] M. Shao *et al.*, Extensive particle identification with TPC and TOF at the STAR experiment, *Nuclear Instruments and Methods in Physics Research Section A: Accelerators, Spectrometers, Detectors and Associated Equipment*, **558**, 419 – 429, 2006.

[SF10] A. Strandlie and R. Frühwirth, Track and vertex reconstruction: From classical to adaptive methods, *Rev. Mod. Phys.*, **82**, 1419–1458, 2010.

[Shi09] S. Shi, Event anisotropy at STAR, *Nuclear Physics A*, **830**, 187c – 190c, 2009.

[Shi12] S. Shi, Event anisotropy $v_2$ in Au+Au collisions at $\sqrt{s_{NN}}$ = 7.7 - 62.4 GeV with STAR, 2012, arXiv:1210.4607 [nucl-ex].

[SP11] S. Schlichting and S. Pratt, Charge conservation at energies available at the BNL Relativistic Heavy Ion Collider and contributions to local parity violation observables, *Phys. Rev. C*, **83**, 014913, 2011.

[SPG12] T. Song, S. Plumari, V. Greco, C. M. Ko, and F. Li, Partonic mean-field effects on matter and antimatter elliptic flows, 2012, arXiv:1211.5511 [nucl-th].

[SY81] H. Sato and K. Yazaki, On the coalescence model for high energy nuclear reactions, *Physics Letters B*, **98**, 153 – 157, 1981.

[SZ04] D. T. Son and A. R. Zhitnitsky, Quantum anomalies in dense matter, *Phys. Rev. D*, **70**, 074018, 2004.

[Thi84] P. Thieberger, The Brookhaven double MP facility: Recent developments and plans for the future, *Nuclear Instruments and Methods in Physics Research*, **220**, 45 – 53, 1984.

[Vol04] S. A. Voloshin, Parity violation in hot QCD: How to detect it, *Phys. Rev. C*, **70**, 057901, 2004.

[Vol10] S. A. Voloshin, Testing the Chiral Magnetic Effect with Central $U+U$ Collisions, *Phys. Rev. Lett.*, **105**, 172301, 2010.

[VZ96] S. Voloshin and Y. Zhang, Flow study in relativistic nuclear collisions by Fourier expansion of azimuthal particle distributions, *Zeitschrift für Physik C Particles and Fields*, **70**, 665–671, 1996.

[WAH57] C. S. Wu, E. Ambler, R. W. Hayward, D. D. Hoppes, and R. P. Hudson, Experimental Test of Parity Conservation in Beta Decay, *Phys. Rev.*, **105**, 1413–1415, 1957.

[Wan97] X.-N. Wang, A pQCD-based approach to parton production and equilibration in high-energy nuclear collisions, *Physics Reports*, **280**, 287 – 371, 1997.

[Wan10] F. Wang, Effects of cluster particle correlations on local parity violation observables, *Phys. Rev. C*, **81**, 064902, 2010.

[Whi98] S. N. White, Forward measurements in RHIC and LHC heavy ion collisions, *Nuclear Instruments and Methods in Physics Research Section A: Accelerators, Spectrometers, Detectors and Associated Equipment*, **409**, 618 – 620, 1998.

[XCK12] J. Xu, L.-W. Chen, C. M. Ko, and Z.-W. Lin, Effects of hadronic potentials on elliptic flows in relativistic heavy ion collisions, *Phys. Rev. C*, **85**, 041901, 2012.

[Yep96] P. Yepes, A fast track pattern recognition, *Nuclear Instruments and Methods in Physics Research Section A: Accelerators, Spectrometers, Detectors and Associated Equipment*, **380**, 582 – 585, 1996.

[Zha98] B. Zhang, ZPC 1.0.1: a parton cascade for ultrarelativistic heavy ion collisions, *Computer Physics Communications*, **109**, 193 – 206, 1998.

# Presentations and publication List

## Presentations

1. Mar. 2013, Search for Chiral Magnetic Effects in Au + Au Collisions at STAR, oral presentation, Moriond QCD and High Energy Interactions, La Thuile, Italy

2. Aug. 2012, Charge Asymmetry Dependency of $\pi^+/\pi^-$ Azimuthal Anisotropy in Au + Au Collisions at STAR, poster, Quark Matter 2012 International Conference, Washington, DC, USA

3. Apr. 2012, Charge Asymmetry Dependency of $\pi^+/\pi^-$ elliptic flow in Au + Au Collisions at 200 GeV, oral presentation, The 28th Winter Workshop on Nuclear Dynamics, Dorado del Mar, Puerto Rico

4. Jun. 2011, A High Level Online Tracking Trigger for the STAR Experiment at RHIC, poster, RHIC & AGS Annual Users' Meeting, Upton, NY, USA

5. Apr. 2011, The Monte-Carlo Environment for the STAR High Level Trigger, oral presentation, American Physical Society (APS) April meeting, Anaheim, CA, USA

## Publication list

1. Charge asymmetry dependency of $\pi^+/\pi^-$ elliptic flow in Au + Au collisions at $\sqrt{s_{NN}} = 200$ GeV, **Hongwei Ke** for the STAR Collaboration, Journal of Physics: Conference Series **389**, 012035, 2012

2. Critical phenomena in a disc-percolation model and their application to relativistic heavy ion collisions, **KE Hong-Wei**, XU Ming-Mei and LIU Lian-Shou, Chinese Physics C **33**, 854-859, 2009

3. Characterizing variable for the critical point in momentum space, DU Jia-Xin, **KE Hong-Wei**, XU Ming-Mei and LIU Lian-Shou, Chinese Physics C **33**, 655-660,

2009

4. Imaging source with Gaussian proper time distribution, CHEN Li-Zhu, **KE Hong-Wei** and WU Yuan-Fang, Chinese Physics C **33**, 661-665, 2009

## STAR Publications as Principal Author

5. STAR Collaboration, L. Adamczyk et al., Inclusive charged hadron elliptic flow in Au + Au collisions at $\sqrt{s_{NN}} = 7.7 - 39$ GeV, Phys. Rev. C, **86**, 054908, 2012

6. STAR Collaboration, H. Agakishiev et al., Observation of the antimatter helium-4 nucleus, Nature, **473**, 353356, 2011

## STAR Publications:

7. STAR Collaboration, L. Adamczyk et al., Observation of an Energy- Dependent Difference in Elliptic Flow between Particles and Antiparticles in Relativistic Heavy Ion Collisions, Phys. Rev. Lett., **110**, 142301, 2013.

8. STAR Collaboration, L. Adamczyk et al., Single spin asymmetry in polarized proton - proton elastic scattering at $\sqrt{s}$ = 200 GeV, Physics Letters B, **719**, 62 69, 2013

9. STAR Collaboration, L. Adamczyk et al., Transverse single-spin asymmetry and cross section for $\pi^0$ and $\eta$ mesons at large Feynman $x$ in $p^{\uparrow} + p$ collisions at $\sqrt{s}$ = 200 GeV, Phys. Rev. D, **86**, 051101, 2012

10. STAR Collaboration, L. Adamczyk et al., Longitudinal and transverse spin asymmetries for inclusive jet production at mid-rapidity in polarized $p + p$ collisions at $\sqrt{s} = 200$ GeV, Phys. Rev. D, **86**, 032006, 2012

11. STAR Collaboration, L. Adamczyk et al., Measurements of $D^0$ and $D^*$ production in $p + p$ collisions at $\sqrt{s} = 200$ GeV, Phys. Rev. D, **86**, 072013, 2012

12. STAR Collaboration, L. Adamczyk et al., Di-electron spectrum at mid-rapidity in $p + p$ collisions at $\sqrt{s} = 200$ GeV, Phys. Rev. C, **86**, 024906, 2012

13. STAR Collaboration, L. Adamczyk et al., Measurement of the $W \to e\nu$ and $Z/\gamma^* \to e^+e^-$ production cross sections at mid-rapidity in proton-proton collisions at $\sqrt{s}$ = 500 GeV, Phys. Rev. D, **85**, 092010, 2012

14. STAR Collaboration, L. Adamczyk et al., Directed Flow of Identified Particles in Au + Au Collisions at $\sqrt{s_{NN}}$ = 200 GeV at RHIC, Phys. Rev. Lett., **108**, 202301, 2012

15. STAR Collaboration, G. Agakishiev et al., Energy and system-size dependence of two- and four-particle $v_2$ measurements in heavy-ion collisions at $\sqrt{s_{NN}}$ = 62.4 and 200 GeV and their implications on flow fluctuations and nonflow, Phys. Rev. C, **86**, 014904, 2012

16. STAR Collaboration, G. Agakishiev et al., System size and energy dependence of near-side dihadron correlations, Phys. Rev. C, **85**, 014903, 2012

17. STAR Collaboration, G. Agakishiev et al., Directed and elliptic flow of charged particles in Cu + Cu collisions at $\sqrt{s_{NN}}$ = 22.4 GeV, Phys. Rev. C, **85**, 014901, 2012

18. STAR Collaboration, G. Agakishiev et al., $\rho^0$ photoproduction in AuAu collisions at $\sqrt{s_{NN}}$ = 62.4 GeV measured with the STAR detector, Phys. Rev. C, **85**, 014910, 2012

19. STAR Collaboration, G. Agakishiev et al., Strangeness Enhancement in Cu-Cu and Au-Au Collisions at $\sqrt{s_{NN}}$ = 200 GeV, Phys. Rev. Lett., **108**, 072301, 2012

20. STAR Collaboration, G. Agakishiev et al., Identified Hadron Compositions in $p+p$ and Au + Au Collisions at High Transverse Momenta at $\sqrt{s_{NN}}$ = 200 GeV, Phys. Rev. Lett., **108**, 072302, 2012

21. STAR Collaboration, G. Agakishiev et al., Evolution of the differential transverse momentum correlation function with centrality in Au+Au collisions at, Physics Letters B, **704**, 467 473, 2011

22. STAR Collaboration, H. Agakishiev et al., Experimental studies of di-jet survival and surface emission bias in Au+Au collisions via angular correlations with respect to back-to-back leading hadrons, Phys. Rev. C, **83**, 061901, 2011

23. STAR Collaboration, H. Agakishiev et al., High $p_T$ nonphotonic electron production in $p+p$ collisions at $\sqrt{s_{NN}} = 200$ GeV, Phys. Rev. D, **83**, 052006, 2011